MASTER OF SCIENCE THESIS

Orthogonal Vortex-Propeller Interaction: Vortex Response and Impact on the Propeller Performance

For obtaining the degree Master of Science in Aerospace Engineering

at Delft University of Technology

REGISTRATION NUMBER: 054#15#MT#FPP

ZHOU TENG

Sep 2015, Delft

TU Delft Delft University of Technology

Delft University of Technology

Department of Aerodynamics, Wind Energy, Flight Performance and Propulsion

The undersigned hereby certify that they have read and recommend to the Faculty of Aerospace Engineering for acceptance a thesis entitled "**Orthogonal Vortex-Propeller Interaction: Vortex Response and Impact on the Propeller Performance**" by **Zhou Teng** in partial fulfillment of the requirements for the degree of Master of Science.

Chairman: _____
Prof. Dr. -Ing. G. Eitelberg (TU Delft)

Member: _____
Prof. dr. ir. Leo L.M. Veldhuis (TU Delft)

Member: _____
Yannian Yang, M.Sc (TU Delft)

Member: _____
Dr. Daniele Ragni (TU Delft)

Dated: _____.

Abstract

In some situations, concentrated vorticity which forms a vortical flow is involved in the inflow of a propeller. The impingement of the vortex on the propeller has several detrimental effects, e.g., foreign object damage during ground operation, impact on the propeller performance, unsteady loading on the blade, and tonal noise generation. The research presented in this report is conducted for the concern of the effects of the interaction between inflow vortex and propeller, in terms of vortex response to the propeller and vortex impact on the aerodynamic performance of the propeller.

The impact of impinging vortex on the propeller is studied by experimental and numerical methods. The variation of the propeller performance caused by the impingement of vortex is dependent on the relatively rotational direction of the vortex and the propeller. For the counter-rotating case, the thrust and torque coefficients are increased by the vortex impingement; and vice versa for the co-rotating case. The variations of the thrust and torque coefficients are proportional to the vortex strength. And it becomes more significant as the radial impingement position moves inwards and the advance ratio increases. However, the impingement of vortex does not evidently affects the efficiency of the propeller.

The response of vortex to the propeller is investigated by PIV measurement. The variation of vortex behaviors is dependent on the phase angle of the propeller blade. At the phase angles when the wake of the blade is away from the impinging vortex, the vortex core circulation is independent from the impact of propeller. Due to the contraction of the stream tube caused by the propeller suction, the vortex core radius observed in the measurement plane downstream the propeller is smaller than that in the flow field upstream, and the magnitude of vortex vorticity and the maximum tangential velocity becomes larger. At the phase angle when the vortex core coincides with the propeller blade wake vortices, characteristics of the impinging vortex are dependent on the sign of the vorticity of the impinging vortex and the blade wake. For the case that the impinging vortex and the blade wake have the opposite sign of vorticity, the impinging vortex and the blade wake break each other into fractions with smaller core radius and circulation; for the case with the same sign of vorticity, they merge together, forming a new pattern with higher magnitude of vorticity.

Acknowledgment

The thesis work presented in this report is conducted to obtain my degree of Master of Science in Aerospace Engineering in the Faculty of Aerospace Engineering of Delft University of Technology (TUD). All the experiments were performed in the low-speed wind-tunnel Open Jet Facility (OJF). Working on the facilities provided in OJF was a valuable and exciting experience for me.

I would like to thank my supervisor Prof. Georg Eitelberg. I have benefited a lot from his extensive knowledge and deep understanding in the academic field. Moreover, his emphasizing and strict requirements in details gradually alter the way I work and raise the standard I set for myself in many other fields.

And also, I would like to express special acknowledgment to my friend, Yannian Yang, who is a PhD candidate in the Faculty of Aerospace Engineering. He provided me tons of help on performing wind-tunnel tests. And I am deeply influenced by the rigorous spirit and good habit he showed during the academic research work. This is the last year of his PhD stage, may everything goes well for his graduation.

At last but certainly not the least, my greatest gratitude goes to my family. Without my parents' sponsoring and support, there is not any opportunity I can finish my Master degree in TUD. And thank my grandparents, who are always confident about me since I was a little child.

Delft, the Netherlands Zhou Teng
September, 2015

Content

Abstract ..... **V**

Acknowledgment ..... **VII**

Content ..... **IX**

List of Figures ..... **XI**

List of Tables ..... **XVII**

Notations ..... **XIX**

1 Introduction **1**
1.1 Motivation 1
1.2 Research background 2
1.2.1 Interaction between vortex and a single blade 2
1.2.2 Interaction between vortex and rotor 4
1.3 Objectives and scope 7
1.4 Outline of the the thesis 8

2 Theories of Propeller and Vortex **9**
2.1 Propeller aerodynamics 9
2.2 Flow in the propeller stream tube 11
2.3 Vortex aerodynamics 12
2.3.1 Circulation and vorticity 12
2.3.2 Vortex profile 14
2.3.3 Biot-Savart law 16

3 Tools for Investigations **19**
3.1 Numerical Approaches 19
3.1.1 Assumptions 19
3.1.2 Aerodynamic principle for BEM theory 19
3.1.3 Application of BEM theory to the case with vortex impingement 23
3.2 Experimental Apparatus and Setups 26
3.2.1 Wind tunnel 26
3.2.2 Propeller rigs 26
3.2.3 Vortex Generator 28
3.2.4 Rotor Shaft Balance 30

3.2.5 Set-up of particle image velocimetry measurement 31
3.3 Test matrix 32
3.4 Blade phase dependent research method 33

4 Results and Analysis 37
4.1 Definitions and Parameters 37
4.2 Impinging Vortex Profile 38
4.3 Propeller performance 39
4.3.1 Corrections on the free stream velocity 39
4.3.2 Impact of the wake of the vortex generator on the propeller performance 41
4.3.3 Validation of BEM model 42
4.3.4 Impact of vortex on the performance of propeller obtained from BEM theory 44
4.3.5 Propeller performance variation 49
4.4 Vortex development through the propeller 53
4.4.1 Variation of vortex behavior through propeller disk 53
4.4.2 Effects of the rotational direction of the impinging vortex 64
4.4.3 Effects of propeller advance ratio 71
4.4.4 Effects of radial impingement position 79

5 Conclusions, Discussion and Recommendation 87
5.1 Variations of propeller performance 87
5.2 Variations of vortex behavior 88
5.3 Discussion of modified BEM theory 89
5.4 Recommendation for future research 89

Reference 91

List of Figures

Figure 1.1: Vortices impingement on blade 2

Figure 1.2: Responses of vortex filament to blade intruding for different d/r_c 3

Figure 1.3: Definition for the relative position of vortex and blade 3

Figure 1.4: Vortex trace visualizati.....5

Figure 1.5: Dependence of the thrust developed by tail rotor on advance ratio in four different configurations (Low/high: tail rotor relative vertical positions compared with the main rotor height, TA: top-aft tail rotor, TF: top-forward tail rotor) 5

Figure 1.6: Interaction between tip vortices and wake produced by main rotor and tail rotor[14].....6

Figure 1.7: Variation of load distribution on tail rotor disk caused by the impingement of main rotor tip vortices (advance ratio = 0.12).....6

Figure 2.1: Definition of velocities and forces on a blade element 9

Figure 2.2: Pressure and velocity in the flow fields upstream and downstream the propeller 11

Figure 2.3: Distribution of pressure and axial velocity in the flow fields upstream and downstream the propeller 11

Figure 2.4: Vortex filament and surfaces definitions.....14

Figure 2.5: Vortex cross sectional profile and tangential velocity radial distribution15

Figure 2.6: Vortex tangential velocity profile (Lamb-Oseen).....16

Figure 2.7: Biot-Savart law.....17

Figure 3.1: Stream tube through an annular element of the propeller disk 21

Figure 3.2: Relative locations of propeller and vortex in the propeller disk plane....24

Figure 3.3: Variations of velocities and forces on the blade cross section located at point P. The dashed lines illustrate the velocities and forces generated in the isolated propeller case, and the continuous lines indicate the case with inflow vortex impingement. 25

Figure 3.4: Scheme of propeller disk division 25

Figure 3.5: TU Delft Open Jet Facility.....26
Figure 3.6: F29 propeller profile.....27
Figure 3.7: Chord length and incidence angle distribution along the blade span direction.....28
Figure 3.8: Profile of the DU 96-W-180 airfoil.....28
Figure 3.9: C_l-α curve of airfoil DU 96-W-180.....29
Figure 3.10: Propeller and vortex generator set-up.....30
Figure 3.11: Diagram of RSB.....30
Figure 3.12: Schemes of PIV measurement planes and camera set-up.....31
Figure 3.13: Position and dimension of PIV measurement windows.....32
Figure 3.14: Definition of 0 phase angle.....34
Figure 3.15: Corresponding relationship between the actual blade position and its light reflection in images captured by camera. Images in the right side are taken by the backward camera in the measurement plane downstream the propeller.....35
Figure 4.1: Definition of coordinate.....37
Figure 4.2: Vorticity fields for wingtip vortexes generated by vortex generator with different angles of attack.....38
Figure 4.3: Radial profiles of wingtip vortexes generated by vortex generator with different angles of attack.....38
Figure 4.4: Scheme of flow outside open tunnel outlet entraining to propeller stream tube.....40
Figure 4.5: Comparison of the measured C_T and corrected C_T.....41
Figure 4.6 Impacts of the wake produced by the vortex generator on propeller performance. (α_w=8°).....42
Figure 4.7: Comparison of propeller performance obtained from BEM theory and experiments. (J=0.58).....43
Figure 4.8: Load distribution on disk for the isolated propeller . (J=0.58).....44
Figure 4.9: Radial load distribution for the isolated propeller. (J=0.58).....44
Figure 4.10: Distribution of the coefficients of elemental normal force and out-of-plane component of moment in propeller disk with counter-rotating vortex impingement (J=0.58, r_{imp}=0.74).....45
Figure 4.11: Distribution of the coefficients of elemental normal force and out-of-plane component of moment in propeller disk with co-rotating vortex impingement. (J=0.58, r_{imp}=0.74).....46

Figure 4.12: Subtraction of coefficients of elemental normal force and out-of-plane component of moment for cases $\Gamma_{C,\,imp}$=-0.275 and isolated propeller. (J=0.58, r_{imp}=0.74) 46

Figure 4.13: Subtraction of coefficients of elemental normal force and out-of-plane component of moment for cases $\Gamma_{C,\,imp}$=0.275 and isolated propeller. (J=0.58, r_{imp}=0.74) 47

Figure 4.14: Variations of radial load distribution caused by impinging vortex with opposite rotational directions. (J=0.58, r_{imp}=0.74) 47

Figure 4.15: Propeller load radial distribution in the elemental sector region in which the vortex impinges in. (J=0.58, r_{imp}=0.74).....48

Figure 4.16: Variations of azimuthal load distribution caused by vortex impingement. (J=0.58, r_{imp}=0.74) 49

Figure 4.17: Dependence of propeller performance on advance ratio. ($\Gamma_{C,\,imp}$=-0.275, r_{imp}=0.74).....50

Figure 4.18: Magnitude of thrust and torque increase caused by vortex impingement. ($\Gamma_{C,\,imp}$=-0.275, r_{imp}=0.74).....51

Figure 4.19: Performance of propeller versus radial position of vortex impingement. (J=0.58, $\Gamma_{C,\,imp}$=-0.275) 52

Figure 4.20: Dependence of thrust and torque coefficient on impinging vortex strength. (J=0.58, r_{imp}=0.74) 52

Figure 4.21: Vorticity field and radial profile of tangential velocity. (upstream, J=0.58, r_{imp}=0.74, $\Gamma_{C,\,imp}$=-0.275).....54

Figure 4.22: Dependence of the vorticity field on the blade phase angle. (downstream, J=0.58, r_{imp}=0.74, $\Gamma_{C,\,imp}$=-0.275) 56

Figure 4.23: Scheme of blade wake vortices and the impinging vortex 57

Figure 4.24: Development of the vortex filament locus.....57

Figure 4.25: Comparison of mean and instantaneous positions of vortex center in the measurement planes upstream and downstream the propeller. (J=0.58, r_{imp}=0.74, Γ_C=-0.275) 58

Figure 4.26: Dependence of position of vortex center on blade phase angle. (downstream, J=0.58, r_{imp}=0.74, $\Gamma_{C,\,imp}$=-0.275) 59

Figure 4.27: Radial distribution of induced tangential velocity for the isolated propeller case. (acquired by BEM theory) 60

Figure 4.28: Scheme of the velocities induced by the blade wake vortices. 61

Figure 4.29: Dependence of the vortex core radius on blade phase angle. (downstream, J=0.58, r_{imp}=0.74, $\Gamma_{C,\,imp}$=-0.275) 62

Figure 4.30: Dependence of the maximum tangential velocity on blade phase angle. (downstream, J=0.58, r_{imp}=0.74, $\Gamma_{C,\,imp}$=-0.275) 63

Figure 4.31: Dependence of the vortex core circulation on blade phase angle. (downstream, J=0.58, r_{imp}=0.74, $\Gamma_{C,\,imp}$=-0.275) 64

Figure 4.32: Comparison of vorticity field for impinging vortex with different rotational directions. (upstream, J=0.58, r_{imp}=0.74) 65

Figure 4.33: Comparison of radial profile of the tangential velocity for impinging vortexes with different rotational directions. (upstream, J=0.58, r_{imp}=0.74) 65

Figure 4.34: Dependence of vorticity field on vortex rotational direction. For each case, three phase angles at which blade positions are closest to the impinging vortex column are selected. For each phase angle, the right figure gives the details of the region marked by the rectangular frame in the left figure. (upstream, J=0.58, r_{imp}=0.74) 67

Figure 4.35: Dependence of the mean positions of vortex center on blade phase angles. (downstream, J=0.58, r_{imp}=0.74) 68

Figure 4.36: Effect of vortex rotational direction on the vortex core radius. (downstream, J=0.58, r_{imp}=0.74) 70

Figure 4.37: Effect of vortex rotational direction on the maximum tangential velocity. (downstream, J=0.58, r_{imp}=0.74) 70

Figure 4.38: Effect of vortex rotational direction on the vortex core circulation. (downstream, J=0.58, r_{imp}=0.74) 71

Figure 4.39: Comparison of vorticity field for different advance ratios. (upstream, $\Gamma_{C,\,imp}$=-0.275, r_{imp}=0.74).....72

Figure 4.40: Comparison of radial profile of tangential velocity for different advance ratio conditions. (upstream, $\Gamma_{C,\,imp}$=-0.275, r_{imp}=0.74).....72

Figure 4.41: Dependence of the vorticity field on propeller advance ratio. (downstream, $\Gamma_{C,\,imp}$=-0.275, r_{imp}=0.74).....74

Figure 4.42: Displacement of mean vortex center position between the upstream and downstream measurement planes for different advance ratios. (J=0.58, $\Gamma_{C,\,imp}$=-0.275) 75

Figure 4.43: Statistical analysis of vortex center positions for different advance ratios. (downstream, J =0.58, $\Gamma_{C,\,imp}$=-0.275).....75

Figure 4.44: Dependence of impinging vortex characteristics on propeller advance ratio. (upstream, $\Gamma_{C,\,imp}$=-0.275, r_{imp}=0.74).....76

Figure 4.45: Effect of advance ratio on vortex core radius. (downstream, $\Gamma_{C,\,imp}$=-0.275, r_{imp}=0.74).....77

Figure 4.46: Effect of advance ratio on the maximum tangential velocity. (downstream, $\Gamma_{C,\,imp}$=-0.275, r_{imp}=0.74) 77

Figure 4.47: Variation of vortex core radius and maximum tangential velocity between the measurement planes upstream and downstream the propeller. 78

Figure 4.48: Effect of advance ratio on the vortex core circulation. (downstream, $\Gamma_{C,\,imp}$=-0.275, r_{imp}=0.74) 78

Figure 4.49: Vorticity distribution for different impinging radial positions. (upstream, J=1.10, $\Gamma_{C,\,imp}$=-0.275) 79

Figure 4.50: Vortex tangential velocity radial distribution variation for different impinging radial positions. (upstream, J=1.10, $\Gamma_{C,\,imp}$=-0.275) 80

Figure 4.51: Vorticity fields for different vortex impinging radial positions. For each case, phase angles at which blade wake vortices coincide with the impinging vortex column and the following one were selected. (downstream, J=1.10, $\Gamma_{C,\,imp}$=-0.275) 81

Figure 4.52: Statistical analysis of vortex center positions for different radial impingement positions (J=1.10, $\Gamma_{C,\,imp}$=-0.275). 82

Figure 4.53: Scheme of the velocities induced by vortices at different radial positions 82

Figure 4.54: Dependence of r_c, $V_{t,v,m}$ and Γ_C on radial impingement position. (upstream, J=0.58, $\Gamma_{C,\,imp}$=-0.275) 83

Figure 4.55: Effect of radial impingement position on vortex core radius. (downstream, J=0.58, $\Gamma_{C,\,imp}$=-0.275) 84

Figure 4.56: Effect of radial impingement position on vortex maximum tangential velocity. (downstream, J=0.58, $\Gamma_{C,\,imp}$=-0.275) 85

Figure 4.57: Effect of radial impingement position on vortex core circulation. (downstream, J=1.10, $\Gamma_{C,\,imp}$=-0.275) 85

List of Tables

Table 3.1: Features of propeller model used in experiments 26

Table 3.2: PIV & RSB measurements matrix 32

Table 4.1: Comparison of vortex characteristics for different angles of attack of the vortex generator 39

Table 4.2: Variation of propeller performance caused by impinging vortex with opposite rotational directions. (J=0.58, r_{imp}=0.74).....45

Table 4.3: Statistical comparison of instantaneous vortex center positions. (J=0.58, r_{imp}=0.74, $\Gamma_{C,\,imp}$=-0.275) 58

Table 4.4: Effect of vortex rotational direction on vortex core center positions (J=0.58, r_{imp}=0.74) 68

Table 4.5: Comparison of impinging vortex core radius, maximum tangential velocity and core circulation for different vortex rotational directions. (upstream, J=0.58, r_{imp}=0.74).....69

Notations

Latin symbols

A	Area of propeller disk	m^2
A_1, A_2	Vortex tube cross sections	m^2
b	Distance between vortex and propeller centers, non-dimensionalized by propeller radius	
C	Closed curve	
C_{Fx}	Coefficient of propeller normal force	
C_{Mx}	Coefficient of propeller out-of-plane component of moment	
C_T	Thrust coefficient	
C_Q	Torque coefficient	
c	Chord length of blade	m
c_d	Drag coefficient of airfoil	
c_l	Lift coefficient of airfoil	
$c_{3/4R}$	Blade chord length at three-quarter spanwise position	m
d	ratio of blade thickness	
dD	Elemental drag	N
dl	Line element	m
dQ	Elemental torque	N•m
dT	Elemental thrust	N
F	Tip-loss factor	
h_t	Vertical location of the tail rotor with respect to the main rotor, non-dimensionalized by the main rotor radius	
J	Advance ratio	
J_{cor}	Corrected advance ratio	
N	Blade number of propeller	
n	Propeller rotational speed	rps
$\vec{n}$	Normal vector	
P_{in}	Total power generated by propeller	W
P_{out}	Power used for producing thrust	W
p_∞	Free stream pressure	Pa
p'	Pressure in front of the propeller disk	Pa
Q	Propeller torque	N•m
q	Propeller sink strength	m^3/s

R	Propeller radius	m
R_{hub}	Propeller hub radius	m
Re_v	Vortex Reynolds number	
r_b	Radial position of propeller disk, non-dimensionalized by propeller radius	
r_c	Vortex core radius, non-dimensionalized by propeller radius	
r_{imp}	Vortex impinging radial position on propeller disk, non-dimensionalized by propeller radius	
r_v	Radial position of vortex, non-dimensionalized by vortex radius	
S_C	Area of vortex core	m^2
S_{inf}	Area of the cross-section of the stream tube at the position infinite upstream the propeller	m^2
S_p	Area of propeller disk	m^2
S_{tunnel}	Area of the cross section of the wind-tunnel exit	m^2
T	Propeller thrust	N
T_Ψ	Phase angle period	
t	Time	s
U	Equivalent inflow velocity through the propeller disk	m/s
U_{cor}	Corrected propeller inflow speed	m/s
U_{inf}	Free stream velocity	m/s
U_1	Flow speed far downstream the propeller disk	m/s
V	Velocity of one point in the vortex filament flow field	m/s
$V_{b\text{-}v}$	Blade-vortex relative approaching speed	m/s
V_p	Effective blade element flow velocity	m/s
V_t	Effective tangential velocity	m/s
$V_{t,b}$	Tangential velocity of a point on blade	m/s
$V_{t,v}$	Tangential velocity of a point in vortex cross-sectional plane	m/s
$V_{t,v,m}$	Maximum vortex tangential velocity along radial direction, non-dimentionalized by inflow speed	
v_a	Axial induced velocity	m/s
v_t	Tangential induced velocity	m/s
$v_{t,1}$	Rotational speed far behind propeller disk	m/s

Greek symbols

α, α_b	Angle of attack of cross section of blade	rad
α_w	Angle of attack of the vortex generator	deg
β	$\beta = \theta_b - \alpha_b$	
γ	Oseen parameter	
Γ, Γ_v	Vortex circulation	m^2/s

Γ_C	Vortex core circulation, non-dimensionalized by $(R \cdot U_{inf})$	
$\Gamma_{C,\,imp}$	Original core circulation of the impinging vortex, non-dimensionalized by $(R \cdot U_{inf})$	
δ	Eddy viscosity coefficient	
ζ	Wingtip vortex age	
η_{prop}	Propeller efficiency	
Θ	Vorticity flux	
θ_b	Pitch angle of blade station	rad
λ	Angle between vortex and blade local tangential velocity	rad
ν	Kinetic viscosity	m^2/s
ρ	Fluid density	$kg \cdot m/s^2$
ρ_a	Air density	$kg \cdot m/s^2$
σ	Solidity of the blade	
φ	Angle between the blade and the line connecting vortex and propeller centers	rad
Ψ	Blade phase angle	rad
ϕ	Azimuth in propeller disk	rad
ω	Vorticity	s^{-1}
ω_x	Vorticity in the axial direction	s^{-1}

Abbreviation

BEM	Blade element momentum
BVI	Blade vortex interaction
CCD	Charge-coupled device
CFD	Computational fluid dynamic
LIF	Laser-induced fluorescence
NLR	Nationaal lucht-en ruimtevaartlaboratorium
OJF	Open jet facility
PIV	Particle image velocimetry
RSB	Rotor shaft balance
TA	Top-aft tail rotor
TF	Top-forward tail rotor
TUD	Delft University of Technology
OFAT	One-factor-at-a-time method

1
Introduction

1.1 Motivation

Inflow involving concentrated vorticity is a widely observed non-uniform flow situation in the community of turbomachinery and windmill farm. Orthogonal blade vortex interaction (BVI) often occurs to the blade plane. For the open rotor (Figure 1.1(a)) and turbo-fan engine aircraft (Figure 1.1(b)), vortices might be shed from the ground and impinge into blade from the upstream side during the ground operation[1]. For a helicopter, blade tip vortices shed from the main rotor may have orthogonal interaction with the tail rotor[2], as shown in Figure 1.1(c). In addition, similar interactions may also occur in many other fan or turbine situations, like pump intakes[3].

(a) Ground vortices toward the propeller of C130 aircraft[1]

(b) Ground vortices toward the engine inlet on a YC-14 aircraft[1]

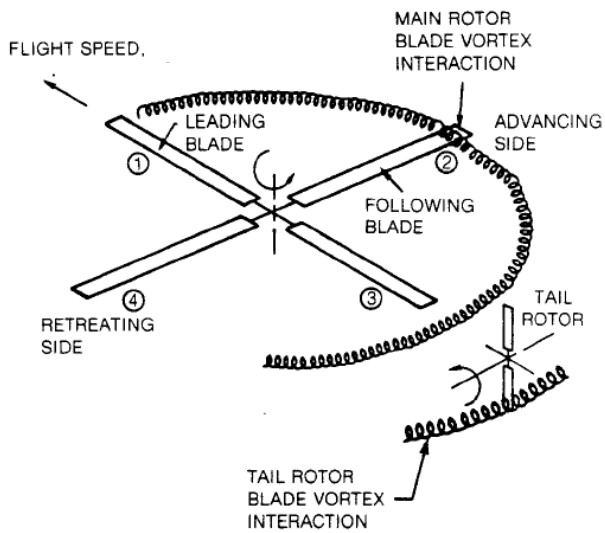

(c) Interaction between main rotor vortices and tail rotor[2]

Figure 1.1: Vortices impingement on the blade

Vortex impingement on the rotor or turbomachinery has several impacts. The ground vortices may bring debris or other external objects into the aircraft engine, or create flow distortion which has adverse effect on engine aerodynamic stability, rising potential for compressor surge and decreasing the stall margin[4]. It can also cause pressure distribution variation and net force generated on the propeller blades surfaces, resulting in propeller performance fluctuation. Besides, the vortex impingement can change the noise generation, leading to noise source positions displacement and amplitude increase in far field[2][5].

1.2 Research background

1.2.1 Interaction between vortex and a single blade

Interaction between vortex filament and a single intruding external object was widely investigated. In early 1990's, a numerical model was developed by Marshall, which is implemented by a vortex filament with variation of vortex core area and approached by the long-wave equation[6][7]. Based on that, it was found that the vortex filament will be bent as an external object (plate, cylinder, blade, *etc*.) approaches it. For the blade intruding case, the bending direction and curvature profile are decided by three dimensionless parameters: the ratio of blade thickness d to ambient core radius r_c, d/r_c; the ratio of blade-vortex relative forward speed $V_{b\text{-}v}$ to vortex swirl velocity $\Gamma/2\pi r_c$, $2V_{b\text{-}v}\pi r_c/\Gamma$, and the blade angle of attack α[7]. The vortex filament is bent significantly for a large d/r_c situation (Figure 1.2(a)). While for the cases d/r_c is in the order of unity

or smaller, only shock and expansion waves can be observed in the upper and lower side of the blade, as shown in Figure 1.2(b).

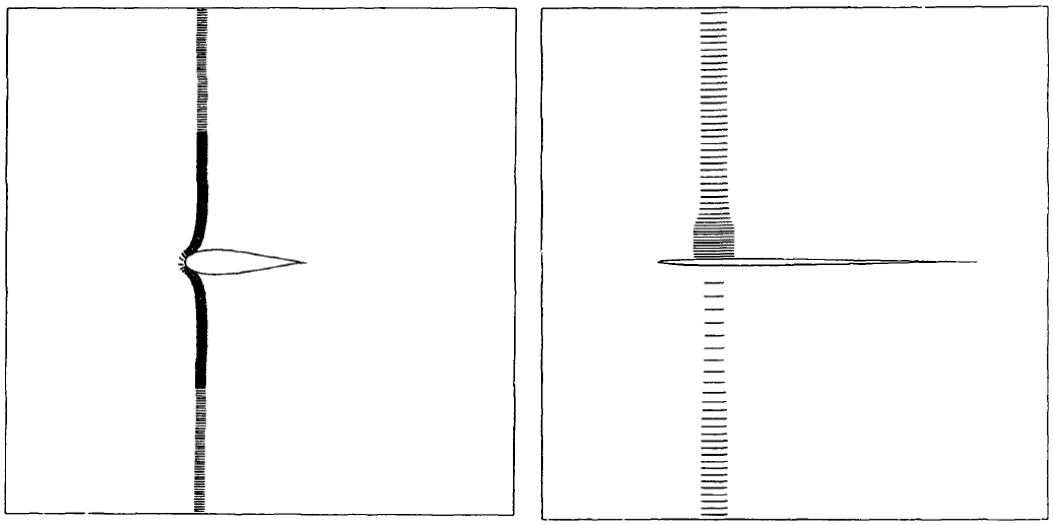

(a) Thick blade (d/r_c=5) intruding case (b) Thin blade (d/r_c=1) intruding case

Figure 1.2: Responses of vortex filament to blade intruding for different ratios of blade thickness over vortex radius d/r_c[7]

Based on a similar numerical model, computational study on orthogonal interaction between a steady blade and an approaching vortex column was conducted by Liu and Marshall[8]. It is reported that for the case that the axial velocity of the vortex column is not zero, while a blade with symmetric airfoil going through the vortex core region in zero angle of attack, pressure distribution on each side of the blade would be different. Magnitude of the pressure in the vortex filament impinging side is higher than that in the other side. As a result, a non-zero normal force is induced on the blade surface in the same direction as the vortex axial velocity.

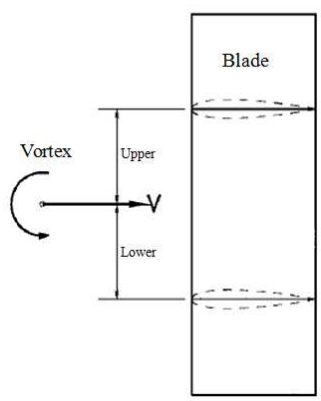

Figure 1.3: Definition of the relative position of vortex and blade[9]

A series of experimental studies on interaction between a steady blade and an approaching vortex filament (Figure 1.3) were conducted by a group of researchers in University of Glasgow. As a vortex filament passes, asymmetric pressure distribution is formed on each side of the blade (with symmetric airfoil), resulting in a normal force generated on its surface, which points to the same direction as the vortex angular velocity (right-hand coordinate)[9]. And such a blade surface normal force measured in these experiments is consistent with Marshall's computational result which suggests the existence of net lift on blade as the blade-vortex interaction occurs.

Furthermore, in the following studies with the same experimental apparatus, it is found that with the blade angle of attack increasing, variation of the pressure on the blade surface becomes more significant. When the vortex core region ages to the the blade leading-edge part, the normal force induced by the pressure difference on blade surface increases[10]. And also, it is reported that for high blade angle of attack situations, vortex has effects on flow separation on the surface of the blade. As the vortex filament passes, flow separation was exacerbated in the upper side (which is defined in Figure 1.3) of the blade and diminished in the lower side[11]. Essentially, the variation of flow separation on blade surface is dependent on the direction of the local tangential velocity of the vortex.

1.2.2 Interaction between vortex and rotor

Dependence of the noise generated by propeller on the radial position of vortex impingement was studied by Ahmadi & Beranek with experimental work. Cases for the impinging positions close to and away from the propeller tip region were compared. It is concluded that as the impinging position moves towards the blade tip, the direction of minimum noise shifts downstream[5]. In their research, smoke was utilized to visualize the vortex behavior, as presented in Figure 1.4. It can be observed that the vortex column bends and convergences in the upstream field because of the propeller contraction to the stream tube, and the radius of the vortex tube increases downstream the propeller disk due to the blade-vortex interaction.

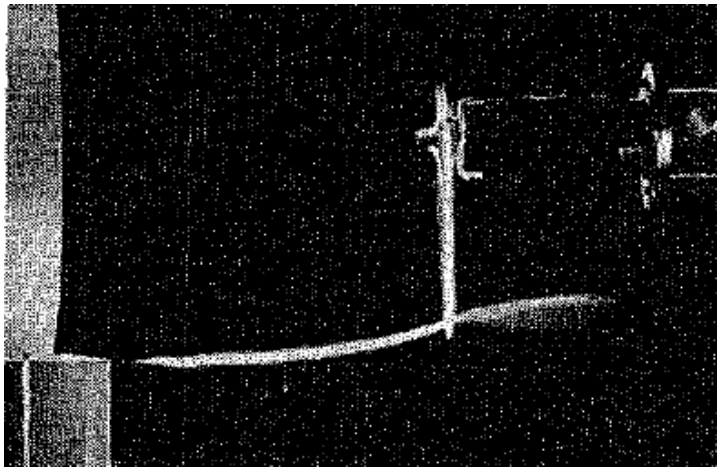

Figure 1.4: Visualization of the vortex trace [5]

To study the impacts of the main-rotor tip vortices on the tail rotor, wind-tunnel tests were performed with a helicopter model in HELIFLOW project. The experimental results suggest that the impingement of main rotor blade tip vortices can change the performance of tail rotor. Trend of the variation is dependent on both tail rotor's relative height to the main rotor and its rotational direction[12][13], as shown in Figure 1.5 (in the view given in Figure 1.5, main blade tip vortices in the tail rotor disk plane rotates in the counter-clockwise sense). At low advance ratio conditions (<0.05), thrust generated by tail rotor is independent of its rotational direction. As advance ratio increases, when the tail rotor counter-rotates (top-aft, denoted as TA) with the main rotor vortices, the thrust is larger than that generated in the other rotational sense case (top-forward, denoted as TF). In addition, by raising the tail rotor relative height to the main rotor, the occurrence of thrust divergence is delayed to higher advance ratio and the magnitude of divergence becomes smaller.

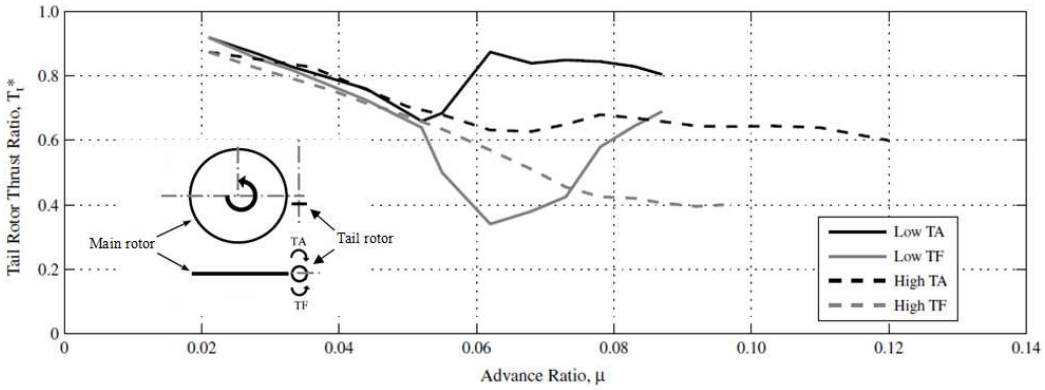

Figure 1.5: Dependence of the thrust developed by tail rotor on advance ratio in four different configurations (Low/high: tail rotor relative vertical positions

compared with the main rotor height, TA: top-aft tail rotor, TF: top-forward tail rotor)[12]

Based on the same helicopter model, impacts of the tip vortices and wake produced by the main rotor on the tail rotor was simulated by Fletcher & Brown by performing CFD tools (Figure 1.6). Their results reveal that with the impingement of main blade vortices, distribution of load and local inflow angle of attack in the tail rotor disk are no longer axisymmetrical. The variation of load distribution is shown in Figure 1.7. With the main rotor tip vortices rotating in the top-forward sense, comparing to the isolated tail rotor case (Figure 1.7(a)), for the top-forward case (Figure 1.7(b)), load increase only occurs on a small region in the bottom half of the tail rotor disk. While, for the top-aft case (Figure 1.7(c)), magnitude of the load coefficient on a much larger area of the tail rotor disk increases[14].

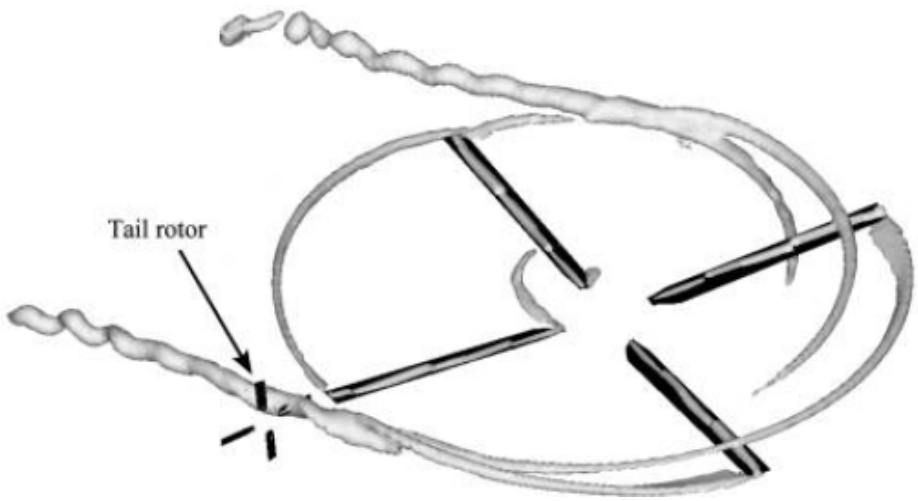

Figure 1.6: Interaction between tip vortices produced by main rotor and tail rotor[14]

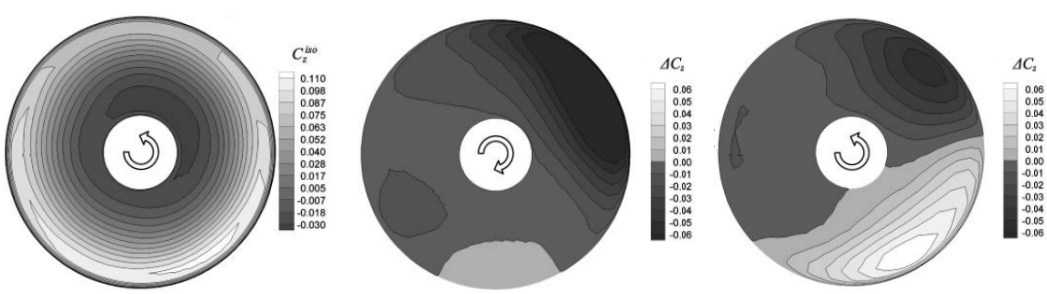

(a) Isolated (top-aft) tail rotor (b) Top-forward tail rotor (c) Top-aft tail rotor

Figure 1.7: Variations of the load distribution on the tail rotor disk caused by the impingement of main rotor tip vortices (advance ratio = 0.12)[14]

1.3 Objectives and scope

As illustrated in the Section 1.2 , most of the previous work focused on interaction between vortex and a single blade. However, in real applications, propeller can generate a series of effects to the flow field which one single blade does not have, involving contraction of the stream tube, induced velocities in both circumferential and axial directions, as well as vorticity in the blade wake and tip vortices. These facts may result in a number of more complicated impacts on the behavior of the impinging vortex.

As well, there is no concept of “performance” for a single blade. Studies on the variation of propeller performance caused by vortex impingement cannot be replaced by investigating the interaction between vortex and a single blade. Although the variations of tail rotor performance caused by the main rotor are reported by the HELIFLOW project, effects of both the tip vortices and wake generated by the main rotor are taken into account. It is not a good model to describe the effect of the impinging vortex itself.

Based on that mismatch between the previous work and the present research questions, objectives of this project are set in two aspects: a) variations of propeller performance caused by vortex impingement, and b) development of vortex filament from flow field upstream to downstream of the propeller disk.

Both numerical and experimental methods are utilized to investigate the variation of propeller performance caused by the impingement of vortex filament, in terms of thrust coefficient, torque coefficient and efficiency. Specifically, interests in the variations of propeller performance are:

1) Dependence of propeller thrust and torque on the impinging vortex strength, rotational direction and impingement radial position.

2) If the vortex has any influence on the efficiency of the propeller

Study on the impinging vortex properties is performed by experimental research tools. Both time averaged and time dependent results of vortex will be examined. Questions to be answered about the development of vortex are:

1) Variation of vortex properties (vorticity, core radius, core circulation, etc.) between the flow fields upstream and downstream of propeller disk.

2) Dependence of vortex properties on blade phase angle.

3) Dependence of vortex characteristics on the rotational direction of vortex, as well as radial impinging position and load of propeller.

1.4 Outline of the the thesis

This thesis report consists of five chapters. The present chapter gives an overview of the topic background and relevant previous work. Based on that, objectives of this project are introduced. Chapter 2 gives the knowledge background of the two research objects, propeller and vortex, and derives some basic physical theorems that will be applied in the discussion presented in the following chapters. Chapter 3 presents the derivation of the numerical research method and introduces facilities utilized in the experimental study. The most important part, Chapter 4, presents and discusses the results obtained from the computational and experimental work, and provides answers for the questions raised in Section 1.3 At last, Chapter 5 summarizes the conclusions achieved from all the investigation results and states a number of recommendations for the further research in this field.

2
Theories of Propeller and Vortex

2.1 Propeller aerodynamics

Propeller is a type of fan that transmits power by converting rotational motion to thrust. Normally, a propeller consists of two or more blades. Each blade is essentially a rotating wing, which produces lift acting as thrust that pulls or pushes aircraft moving forward.

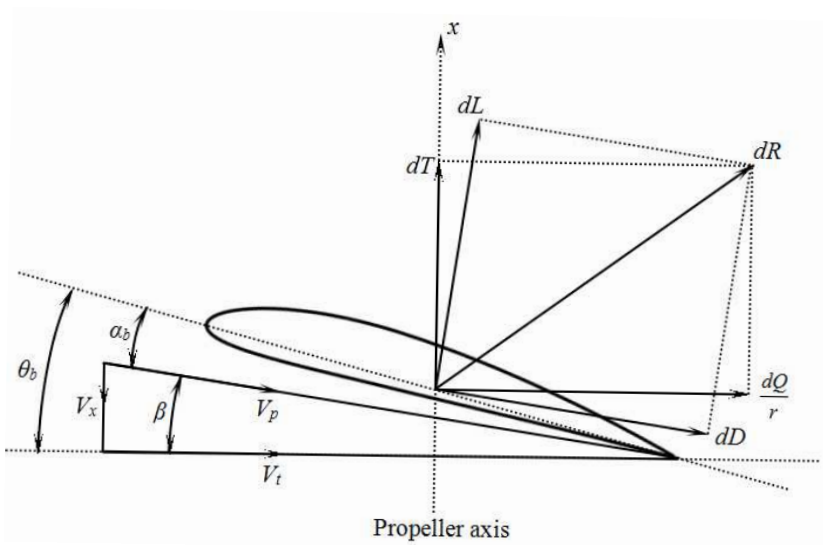

Figure 2.1: Definition of velocities and forces on a blade element

A sketch of forces and velocities on a cross section of the blade is shown in Figure 2.1. Magnitude and direction of the income flow velocity V_p is decided by the local axial velocity V_x and tangential velocity V_t. With geometric pitch angle θ_b constant, the

airfoil angle of attack α_b is only determined by V_x and V_t, which is expressed as

$$\alpha_b = \theta_b - \arctan\frac{V_x}{V_t} \tag{2.1}$$

The elemental force dR generated by the airfoil is equal to the vector addition of elemental lift dL and drag dD, as is shown in Figure 2.1. The axial component of dR (dT) accounts for the propeller thrust, and the tangential component (dQ/r) of that accounts for the propeller torque.

Tangential velocity of the blade cross section increases as the radial position moving outwards. According to Figure 2.1 and Eq. (2.1), it results in larger airfoil angle of attack at the blade tip region. In order to prevent the blade tip stalling at a relative low rotational speed, on each blade, airfoil used for different cross sections are varied along the blade spanwise, and the airfoil incidence angle θ_b decreases from blade root to tip. Then, the tip airfoil angle of attack could be kept relatively small at a certain rotational speed.

Advance ratio (denoted as J) is an important non-dimensional operational parameter for propulsion propeller, which is defined as the ratio between the distance a propeller moves forward during one evolution and its diameter, given by

$$J = \frac{U_{\inf}}{nD} \tag{2.2}$$

where U_{inf} is the true airspeed of the aircraft, n is the propeller rotational speed (in rps), and D is the diameter of the propeller.

To measure the thrust generated by a propeller, thrust coefficient (denoted as C_T) is a commonly used non-dimensional parameter, which is defined as

$$C_T = \frac{T}{\rho n^2 D^4} \tag{2.3}$$

where T is propeller total thrust, ρ is fluid density. And similarly, torque coefficient (C_Q) is given by

$$C_Q = \frac{Q}{\rho n^2 D^5} \tag{2.4}$$

where Q is propeller total torque. As well, with C_T and C_Q known, efficient of the propeller (η_{prop}), defined as the ratio of the power used for generating thrust and total input power, can be expressed as

$$\eta_{prop} = \frac{P_{out}}{P_{in}} = \frac{TU_{\inf}}{2\pi nQ} = \frac{J}{2\pi}\frac{C_T}{C_Q} \tag{2.5}$$

Thus, the efficient is proportional to the propeller advance ratio.

2.2 Flow in the propeller stream tube

Propeller thrust is essentially a result of the pressure difference generated between the upstream and downstream side of the propeller disk. According to the momentum theory (also known as Disk Actuator theory), the propeller has a compression effect to the coming flow, causing the stream tube in vicinity to the disk being contracted, as shown in Figure 2.2. Through the propeller disk plane, both flow axial velocity and static pressure increase. In order to simplify the problem, it is assumed that the flow velocity varies continuously, while the ambient pressure increases suddenly[15], as shown in Figure 2.3. Detailed mathematical derivation of propeller thrust with momentum theory will be presented in Chapter 3.

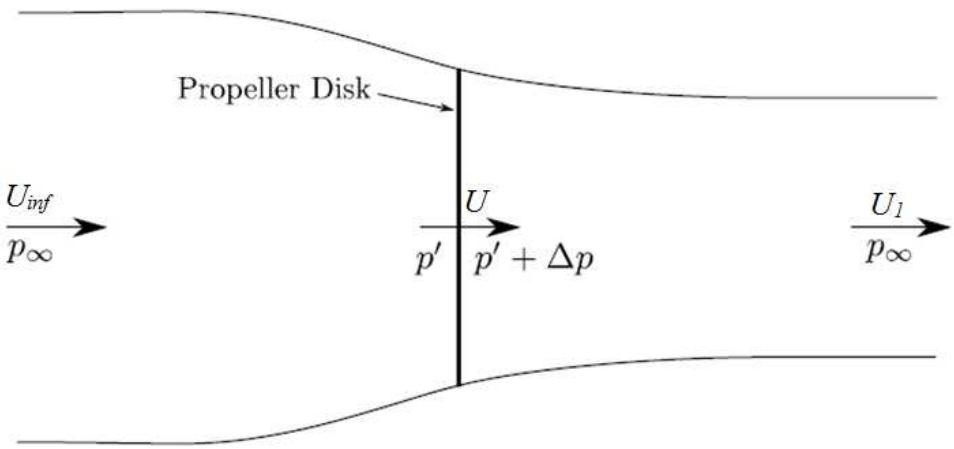

Figure 2.2: Schematic of the stream tube of the propeller[16]

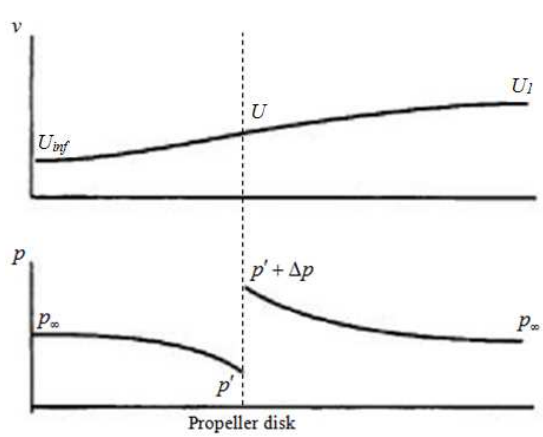

Figure 2.3: Distribution of pressure and axial velocity in the axial direction of the

propeller

2.3 Vortex aerodynamics

Vortical flow is a widely observed non-uniform flow situation in aerodynamic research. In a fluid medium, vortex is a region in which the flow mostly rotates on an axis, which could be either a straight or curved line[17]. Once formed, vortex can stretch and twist. And a moving vortex can carry angular or linear mass, momentum and energy with it.

2.3.1 Circulation and vorticity

To understand the physics and behavior of vortex, some mathematical concepts of circulation and vorticity are going to be introduced at the beginning of this section. Circulation is defined as the integration of velocity along a closed path

$$\Gamma = \oint_C \vec{u} \cdot d\vec{l} \tag{2.6}$$

where $\vec{u}$ is the flow velocity vector, and C is a closed path in the fluid, and $d\vec{l}$ is the length element along the integral path. Vorticity is a measure of the local spin of a fluid element, written as

$$\vec{\omega} = \nabla \times \vec{u} \tag{2.7}$$

To monitor vorticity in a certain surface, another physical quantity, vorticity flux, is introduced. It is defined as the integral of vorticity on the target surface, being expressed as

$$\Theta = \iint_A \vec{\omega} \cdot \vec{n} dA \tag{2.8}$$

where A represents a surface in the fluid, and $\vec{n}$ is the normal vector of the integral surface.

For a closed path in fluid, its circulation is equivalent to the vorticity flux of the surface enclosed by this path. This is known as Stokes' theorem, written as

$$\Gamma = \oint_C \vec{u} \cdot d\vec{l} = \iint_A \vec{\omega} \cdot \vec{n} dA = \Theta \tag{2.9}$$

Thus, Stokes' theorem builds a relationship between surface integral of the curl of a vector field over a surface A and the line integral of the vector field over its boundary C.

In an incompressible fluid with conservative body force, the momentum equation is termed as

$$\frac{Du}{Dt} = -\frac{\Delta p}{\rho} + \nabla \Phi \tag{2.10}$$

where Φ is the potential for body force, and ρ is a function only of the pressure. From Eq. (2.6), we have the convective derivative of circulation

$$\frac{D\Gamma}{Dt}=\frac{D}{Dt}\oint_C \vec{u}\cdot d\vec{l}=\oint_C \frac{D\vec{u}}{Dt}\cdot d\vec{l}+\oint_C \vec{u}\cdot\frac{Dd\vec{l}}{Dt} \tag{2.11}$$

Applying Stokes' theorem given in Eq. (2.9), the first term in the right side of Eq. (2.11) could be written as

$$\oint_C \frac{D\vec{u}}{Dt}\cdot d\vec{l}=\int_A \nabla\times\left(-\frac{\Delta p}{\rho}+\nabla\Phi\right)\cdot\vec{n}dS=\int_A \frac{1}{\rho^2}\left(\nabla\rho\times\nabla p\right)\cdot\vec{n}dS \tag{2.12}$$

Since it is incompressible fluid, density keeps constant, then we have

$$\nabla\rho\times\nabla p=0 \tag{2.13}$$

Then,

$$\oint_C \frac{D\vec{u}}{Dt}\cdot d\vec{l}=0 \tag{2.14}$$

For the second term in the right side of Eq. (2.11), applying the convective derivative for elemental line, we have

$$\oint_C \vec{u}\cdot\frac{Dd\vec{l}}{Dt}=\oint_C \vec{u}\cdot\left(d\vec{l}\cdot\nabla\vec{u}\right)=\oint_C d\vec{l}\cdot\nabla\left(\frac{1}{2}\left|\vec{u}\right|^2\right)=0 \tag{2.15}$$

Substituting Eqs. (2.14) and (2.15) into Eq. (2.11), we obtain the expression for Kelvin's circulation theorem

$$\frac{D\Gamma}{Dt}=0 \tag{2.16}$$

Thus, in a barotropic ideal fluid with conservative body force, around a closed curve, circulation remain constant with time.

To investigate flow vorticity and circulation spatial characteristics, considering a vortex filament (Figure 2.4) in fluid with two cross sections and wall denoted as A_1, A_2 and A_3, respectively. For the closed surface A consisting of A_1, A_2 and A_3, we have its vorticity flux expressed as

$$\Theta=\oiint_A \vec{\omega}\cdot\vec{n}dA=\iint_{A_1}\vec{\omega}_1\cdot\vec{n}_1dA_1+\iint_{A_2}\vec{\omega}_2\cdot\vec{n}_2dA_2+\iint_{A_3}\vec{\omega}_3\cdot\vec{n}_3dA_3 \tag{2.17}$$

where, since A is a closed surface, we have

$$\Theta=\oiint_A \vec{\omega}\cdot\vec{n}dA=0 \tag{2.18}$$

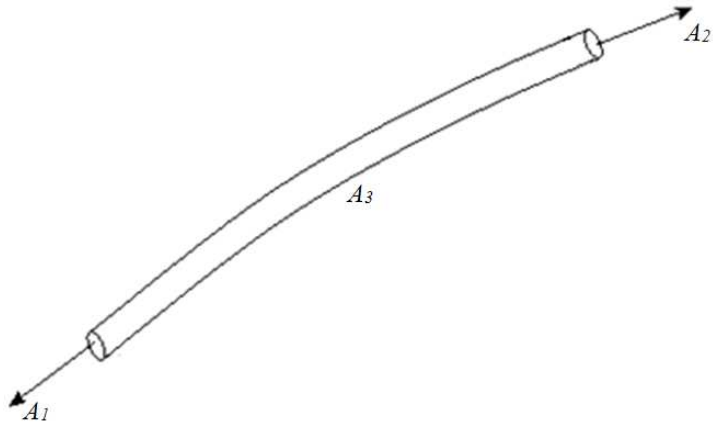

Figure 2.4: Vortex filament represented by a finite tube

On the right side of Eq. (2.17), according to the definition of vortex tube, the third term is 0. And because the surface normal vectors for cross sections A_1 and A_2, $\vec{n}_1$ and $\vec{n}_2$ have opposite directions, the first two terms in the right side of Eq. (2.17) have opposite symbols. Hence, we have Eq. (2.17) becomes

$$\iint_{A_1} \vec{\omega} \cdot \vec{n} dA_1 = \iint_{A_2} \vec{\omega} \cdot \vec{n} dA_2 \tag{2.19}$$

Eq. (2.19) indicates that vorticity flux at different cross sections of the same vortex tube stays constant. According to the Stokes' theorem, it also implies that in a vortex tube, circulation along the boundary path is the same for every cross section.

2.3.2 Vortex profile

In a cross-sectional plane perpendicular to the vortex axis, as shown in Figure 2.5, the vortex profile can be divided into the following four parts[18].

1) Viscous core, which is the most inner part, rotates in a solid-body type.

2) Turbulent mixing region, where flow is dominated by turbulent diffusion and obtains its maximum swirl velocity.

3) Transition region, which lies between the outer inviscid region and the inner regions.

4) Ir-rotational region, which is the outermost region. In this region, the circulation is constant.

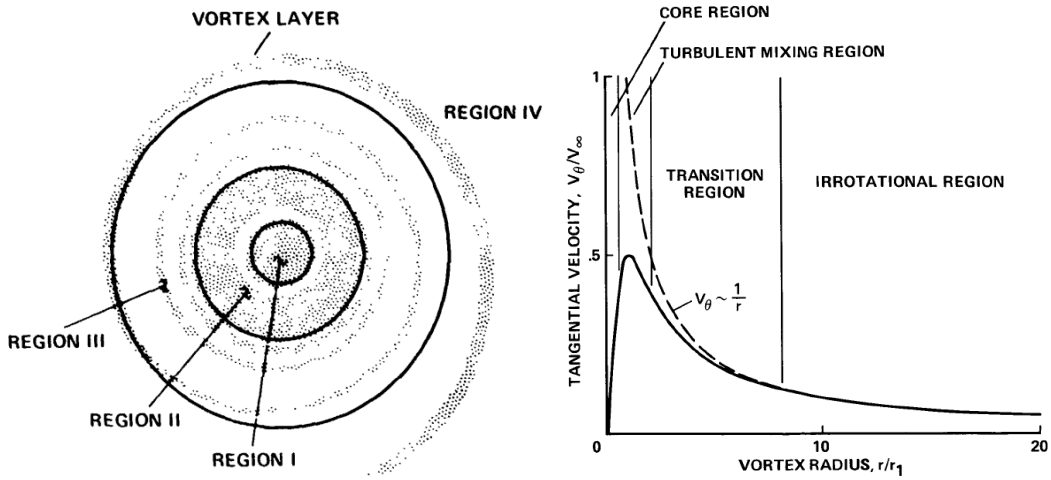

(a) Cross-sectional profile of the vortex[18] (b) Tangential velocity profile[19]

Figure 2.5: the profile of the vortex cross section and the distribution of tangential velocity in the radial direction

Generally, radius of the vortex core is defined as the radial distance from the vortex axis to the position in which the maximum swirl velocity occurs. It is in the same order of the airfoil thickness[20]. For the wingtip vortex case, as the distance downstream from the origin point increases, the vortex core radius increases. Relationship between the vortex core radius and aging time (or downstream distance) can be expressed as a function of the wake age $\zeta=\omega t$[21][22], given by

$$r_C(\zeta)=\sqrt{4\gamma\delta\nu\left(\frac{\zeta+\zeta_0}{U_{\inf}}\right)} \tag{2.20}$$

where γ is the Oseen parameter with a value of 1.25643, ν is the kinematic viscosity, δ is the eddy viscosity coefficient which is given in terms of an empirically determined parameter a_1 and the vortex Reynolds number Re_v

$$\delta=1+a_1\,\mathrm{Re}_v \tag{2.21}$$

Re_v is defined by the ratio of vortex core circulation Γ_C and kinematic viscosity ν, written as

$$\mathrm{Re}_v\equiv\Gamma_C/\nu \tag{2.22}$$

A commonly used model for describing vortex decay due to viscosity is Lamb-Oseen vortex, which is named after Horace Lamb and Carl Wilhelm Oseen[23]. As shown in Figure 2.6(a), Lamb-Oseen model describes the swirl velocity as a function of non-dimensional vortex radius, which is written as

$$V_{t,v}(\bar{r}_v)=\frac{\Gamma_C}{2\pi r_c\bar{r}_v}\left[1-e^{-\bar{r}_v^{\,2}}\right] \tag{2.23}$$

where, the non-dimensional radius is expressed as

$$\bar{r}_v = \frac{r_v}{r_C} \tag{2.24}$$

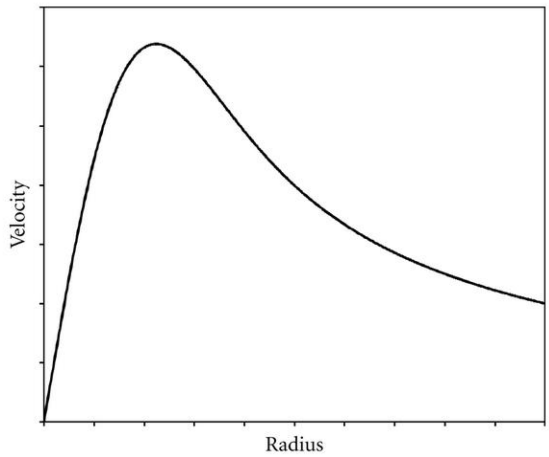

Figure 2.6: Profile of the tangential velocity of the Lamb-Oseen model

2.3.3 Biot-Savart law

Consider a 3-D vortex filament with a general shape. As shown in Figure 2.7, at a point K in flow field, velocity induced by an elemental segment on the vortex filament is given by Biot-Savart law, which is expressed as

$$d\vec{V} = \frac{\Gamma}{2\pi}\frac{\vec{r}\times d\vec{l}}{|\vec{r}|^3} \tag{2.25}$$

where Γ is the circulation of the vortex, $\vec{r}$ extends from the point of integration on the vortex axis to the point K. Integrate Eq. (2.25) along the entire length of the vortex filament, we have the velocity field of the vortex is

$$d\vec{V} = \frac{\Gamma}{2\pi}\int_{-\infty}^{+\infty}\frac{\vec{r}\times d\vec{l}}{|\vec{r}|^3} \tag{2.26}$$

From Eq. (2.26), it is easy to find that for an infinite or a semi-infinite straight vortex filament, the direction of the velocity at any point in the field is perpendicular to the vortex axis line.

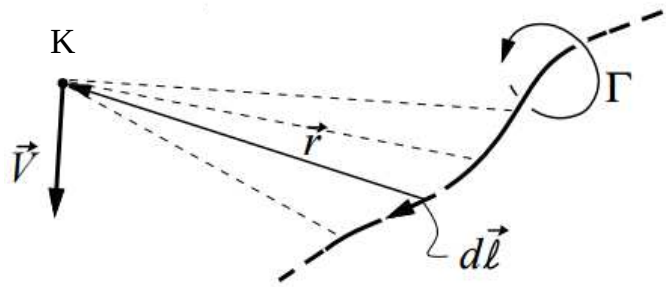

Figure 2.7: Schematic of the induced velocity of the vortex representing the Biot-Savart law

3
Tools for Investigations

3.1 Numerical Approaches

Blade Elemental Momentum (BEM) theory is a well-developed method used to calculate performance of propulsion propeller or wind-turbine. It combines the blade element theory (BET) and momentum theory. In the present project, BEM theory is applied to simulate the results of the propeller performance variation caused by the upstream vortex impingement and numerically analyze the mechanism of that performance variation. As well, it is used to produce some results that cannot be obtained by experiments due to the limitation of experimental condition, such as load distribution on the propeller disk.

3.1.1 Assumptions

To apply BEM theory for propeller performance analysis, it is assumed that the flow is a) inviscid, b) incompressible, c) uniform, and d) free from friction drag.

Besides, to solve the problem in this project, several more assumptions for the impinging vortex are:

1) Vortex core radius and circulation keep constant
2) Vortex model is axisymmetrical.
3) Vortex impinges into the propeller disk plane perpendicularly.
4) Vortex meandering is neglected.
5) Variations of radial and axial velocity caused by vortex are neglected

3.1.2 Aerodynamic principle for BEM theory

In Figure 2.1, the local axial and tangential velocities on a cross section of propeller

blade, V_x and V_t, can be expressed as functions of induced velocities in these two directions (v_a and v_t) as

$$V_x = U_{\inf} + v_a \tag{3.1}$$

$$V_t = \Omega r - v_t \tag{3.2}$$

where Ω is the angular velocity of propeller blade, and r is the radial position on blade. Then, for an elemental blade station at radial position r, according to the knowledge of airfoil aerodynamics, the elemental thrust and torque could be written as

$$dT = \frac{1}{2}\rho_a\left(V_x^2 + V_t^2\right)\left[c_l(\alpha_b)\cos\beta - c_d(\alpha_b)\sin\beta\right]cN \cdot dr\frac{d\phi}{2\pi} \tag{3.3}$$

$$dQ = \frac{1}{2}\rho_a\left(V_x^2 + V_t^2\right)\left[c_l(\alpha_b)\sin\beta + c_d(\alpha_b)\cos\beta\right]cN \cdot rdr\frac{d\phi}{2\pi} \tag{3.4}$$

where ρ_a is the density of air, c is the chord length of the blade element, c_l and c_d are local lift and drag coefficient for the corresponding blade element, which are expressed as functions of the airfoil angle of attack α_b.

To express the elemental thrust and torque by Eqs. (3.3) and (3.4), two unknown quantities, v_a and v_t, have to be solved. Hence, two equations in terms of v_a and v_t are needed. A general illustration for the momentum conservation theory is visualized in Figure 2.2. Since the flow is assumed inviscid and incompressible, according to the Bernoulli's equation, we have

$$p_\infty + \frac{1}{2}\rho_a U_{\inf}^2 = p' + \frac{1}{2}\rho_a U^2 \tag{3.5}$$

in the flow field upstream the propeller disk, and

$$p' + \Delta p + \frac{1}{2}\rho_a U^2 = p_\infty + \frac{1}{2}\rho_a U_1^2 \tag{3.6}$$

In the field downstream, where p_∞ is the flow pressure in the far field, p' is the pressure right upstream the propeller disk. Δp is the pressure raise generated by propeller (as shown in Figure 2.3), through Eqs. (3.5) and (3.6), which can be expressed as

$$\Delta p = \frac{1}{2}\rho_a\left(U_1^2 - U_{\inf}^2\right) \tag{3.7}$$

Considering the thrust produced by the propeller disk as a result of pressure difference between the sides upstream and downstream the propeller disk plane, we have

$$T = A\Delta p = A\frac{1}{2}\rho_a\left(U_1^2 - U_{\inf}^2\right) \tag{3.8}$$

where A is the propeller disk area. Then, expressing thrust as increase of slipstream momentum at the propeller disk plane, we have

$$T = A\rho_a U\left(U_1 - U_{\inf}\right) \tag{3.9}$$

Combining Eqs. (3.1), (3.8) and (3.9) , we have the equivalent axial flow velocity and induced velocity at the propeller disk can be expressed as

$$U = \frac{U_1 + U_{\inf}}{2} \tag{3.10}$$

and

$$v_a = U - U_{\inf} = \frac{1}{2}\left(U_1 - U_{\inf}\right) \tag{3.11}$$

Substituting Eq. (3.10) into Eq. (3.9), we have the thrust written as

$$T = 2A\rho_a\left(U_{\inf} + v_a\right)v_a \tag{3.12}$$

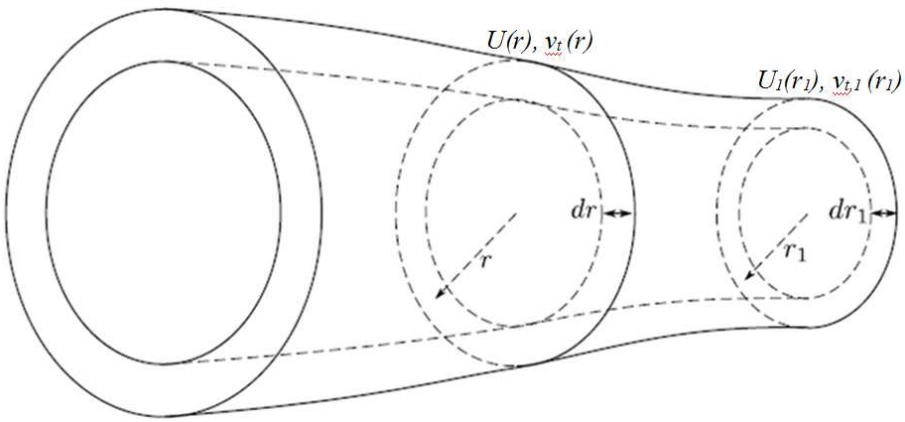

Figure 3.1: Stream tube through an annular element of the propeller disk[16]

To calculate the propeller torque, the the flow stream tube has to be divided into elemental ring tubes as shown in Figure 3.1. For each elemental ring, the elemental torque can be written as

$$dQ = \rho_a U dA v_{t,1} r \tag{3.13}$$

where $v_{t,1}$ is the tangential velocity for an elemental ring in the plane far downstream the propeller disk. Notice that in the following derivation, all the velocities in the propeller disk plane and the plane far downstream are functions of elemental tube radius r and r_1, respectively. For incompressible fluid, the induced tangential velocity at these two planes has a relationship[24] of

$$v_t = \frac{1}{2} v_{t,1} \tag{3.14}$$

Then, substituting Eqs. (3.14) into Eq. (3.13), we have the elemental torque at the disk could be expressed as

$$dQ = 4\pi r^2 dr \rho_a \left(U_{\inf} + v_a\right) v_t \tag{3.15}$$

Similarly, the elemental thrust could be written as

$$dT = 4\pi r dr \rho_a (U_{\inf} + v_a) v_a \tag{3.16}$$

The elemental thrust and torque derivations presented above are conducted under the assumption that the propeller is considered as a circular disk, thus, it has an infinite number of blades. To transform the solution to a real propeller with limited number of blades, apply a correction parameter to Eqs. (3.15) and (3.16), we have

$$dT = 2\rho_a r\,(U_{\inf} + v_a) v_a \cdot dr \cdot F \tag{3.17}$$

$$dQ = 2\rho_a r^2 (U_{\inf} + v_a) v_t \cdot dr \cdot F \tag{3.18}$$

where F is the tip-loss factor, which is proposed by Glauert[24]. It is applied to compensate for the influence of the vortices shed from the tip of each blade[25], expressed as

$$F = \frac{2}{\pi} \cos^{-1} e^{-f} \tag{3.19}$$

where

$$f = \frac{N}{2} \frac{R - r}{r \sin \varphi} \tag{3.20}$$

Note that Eqs. (3.17) and (3.18) can also be applied to a segment on the annular element. On the annular position ϕ, Eqs. (3.17) and (3.18) can be written as

$$dT(r,\phi) = 2\rho_a r\,(U_{\inf} + v_a) v_a \cdot dr d\phi \cdot F \tag{3.21}$$

$$dQ(r,\phi) = 2\rho_a r^2 (U_{\inf} + v_a) v_t \cdot dr d\phi \cdot F \tag{3.22}$$

Equating the thrust and torque expressions given by BET and momentum theory, Eqs. (3.3), (3.4) and Eqs. (3.21), (3.22), we have

$$\frac{1}{2}\sigma V_p^2 [c_l(\alpha_b)\cos\beta - c_d(\alpha_b)\sin\beta] - 2(U_{\inf} + v_a) v_a F = 0 \tag{3.23}$$

$$\frac{1}{2}\sigma V_p^2 [c_l(\alpha_b)\sin\beta + c_d(\alpha_b)\cos\beta] - 2(U_{\inf} + v_a) v_t F = 0 \tag{3.24}$$

where

$$\begin{aligned} V_p &= \sqrt{V_x^2 + V_t^2} \\ &= \sqrt{(U_{\inf} + v_a)^2 + (V_t - v_r)^2} \end{aligned} \tag{3.25}$$

and σ is local solidity of the blade, defined as $\sigma = \dfrac{cN}{2\pi r}$.

The induced velocities v_a and v_r can be obtained by solving Eqs. (3.23) and (3.24). Then the thrust and torque generated by each small segment on elemental ring can be obtained. And the propeller performance can be calculated by integrating the elemental thrust and torque over the whole propeller disk, which are written as

$$T = \int_0^{2\pi} \int_{R_{hub}}^{R} dT(r,\phi) \tag{3.26}$$

$$Q = \int_0^{2\pi} \int_{R_{hub}}^{R} dQ(r,\phi) \tag{3.27}$$

Note that in both Eqs. (3.26) and (3.27), the elemental radius should be integrated from the propeller hub (R_{hub}), instead of the propeller center, to the propeller tip.

3.1.3 Application of BEM theory to the case with vortex impingement

As shown in Figure 3.2, consider a case that the impinging vortex center does not coincide with the propeller axis. Denote the axial distance between the impinging vortex and the propeller in the propeller disk plane as b. For a position point P on one propeller blade, the resultant velocity is an vector addition of vortex tangential velocity $V_{t,v}$ and original blade tangential velocity $V_{t,b}$. Here the angle between the blade and the line connecting propeller and vortex centers is denoted as φ.

Consider the case that the vortex counter-rotates with the propeller (Figure 3.2). According to the law of cosines, we have the distance between P and vortex center is

$$r_v = \sqrt{b^2 + r_b^2 - 2br_b \cos\varphi} \tag{3.28}$$

Hence, the angle (λ) between two tangential velocities, $V_{t,\,b}$ and $V_{t,\,v}$, can be expressed as

$$\lambda = \arccos \frac{r_v^2 + b^2 - r_b^2}{2r_v b} \tag{3.29}$$

Then the resultant tangential velocity at point P is

$$V_t(r_b,\varphi) = \left|\vec{V}_{t,b} + \vec{V}_{t,v} \cos\lambda\right| \tag{3.30}$$

Given the Lamb-Oseen model described in Eq. (2.23), the vortex tangential velocity $V_{t,v}$ can be expressed as

$$V_{t,v} = \frac{\Gamma}{2\pi r_c \bar{r}_v}\left[1 - e^{-\bar{r}_v^2}\right] \tag{3.31}$$

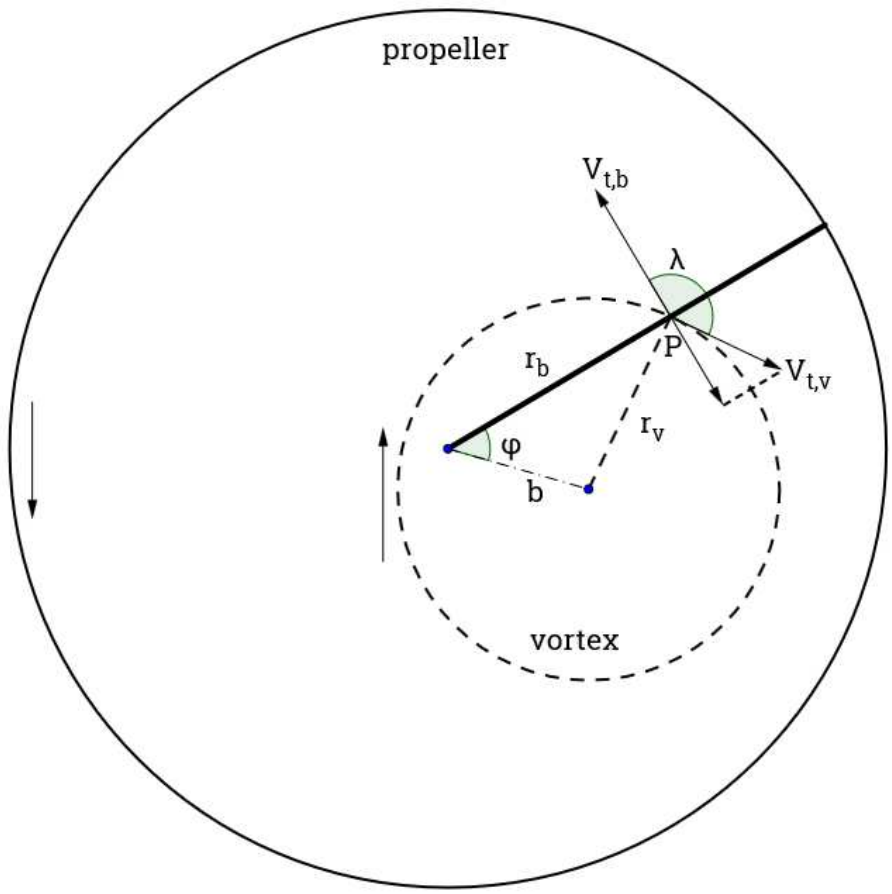

Figure 3.2: Relative locations of the propeller and the vortex in the propeller disk plane

The variations of velocities and forces on the blade cross section at point P are given in Figure 3.3: Variations of velocities and forces on the blade cross section . Because of the increase of tangential velocity (indicated by Eq. (3.30)), the cross section angle of attack becomes larger. As a result, both the elemental lift and drag generated by this cross section increase. That explains the reason why the inflow vortex impingement can vary the load distribution on the propeller disk.

However, notice that the counter-rotating case does not make sure that the resultant tangential velocity on blade cross sections always being larger than the isolated propeller case. For instance, for the case φ=0, on the blade cross sections where $r_b<b$, the resultant tangential velocity V_t is lower than $V_{t,b}$.

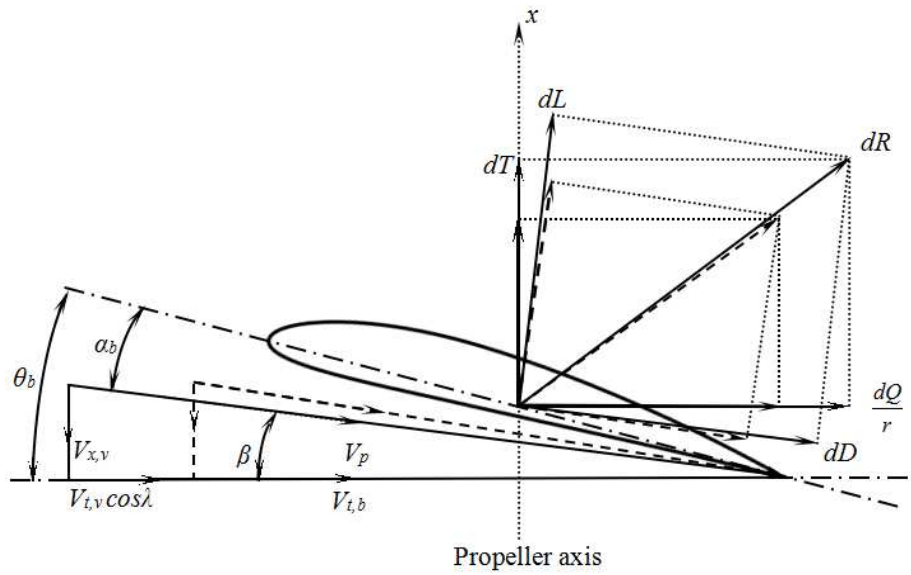

Figure 3.3: Variations of velocities and forces on the blade cross section located at point P (shown in Figure 3.2). The dashed lines illustrate the velocities and forces generated in the isolated propeller case, and the continuous lines indicate the case with inflow vortex impingement.

Substitute Eqs. (3.30) into Eqs. (3.23) and (3.24), the propeller load distribution with upstream vortex impingement can be solved by following the calculation procedure for an isolated propeller, which is illustrated in section 3.1.2 . In this project, to calculate $dT(r_b, \varphi)$ and $dQ(r_b, \varphi)$, the whole propeller disk is divided to 72×17 elements (72 elemental sectors, 17 elemental rings), as shown in Figure 3.4. And the integral of Eqs. (3.26) and (3.27) could be computed by summing the thrust and torque generated at all the elemental regions.

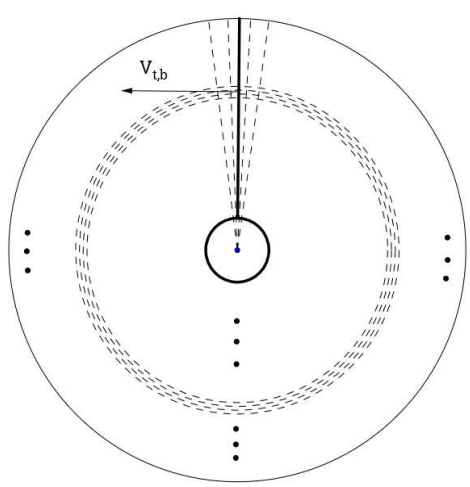

Figure 3.4: Scheme of element of the propeller disk

3.2 Experimental Apparatus and Setups

The experimental study for this project consists of two parts, propeller performance measurement, conducted by rotor shaft balance (RSB) and vortex measurement, performed by particle image velocimetry (PIV) technique. The propeller performance measurement provide validation and comparison for the numerical method illustrated in section 3.1 , and PIV is used to visualize the flow field and quantitatively analyze the behavior of the impinging vortex.

3.2.1 Wind tunnel

All the experiments for this project were conducted in a closed-loop, low-speed wind-tunnel (Figure 3.5), Open Jet Facility (OJF), in Delft University of Technology (TUD). It has an octagonal test section with a cross sectional area of 2.85m×2.85m[26] and maximum flow speed of 35.0m/s.

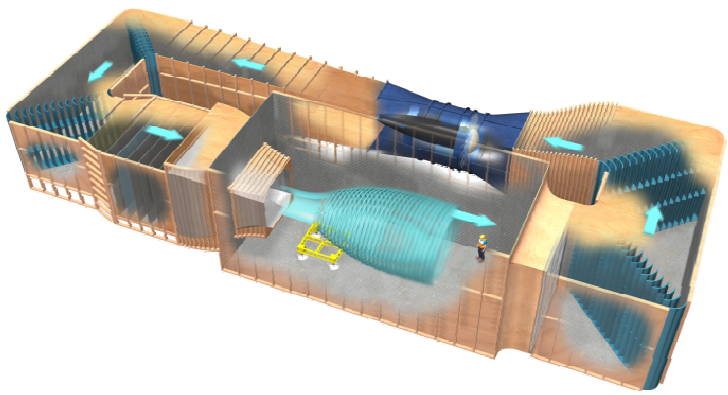

Figure 3.5: Open Jet Facility in TU Delft

3.2.2 Propeller rigs

The propeller applied in experiments was a 1:20 scaled Fokker F29 propeller. It is a well-developed propeller model that has already been used in aerodynamic research for a long time. Several of the structural parameters of this experimentally used propeller are shown in

Table 3.1. In the wind-tunnel tests, this propeller was driven by a TDI 1999 pneumatic motor, whose maximum rotating speed is 22,000 rpm[27].

Table 3.1: Geometric dimension of the F29 propeller

Blades number	8

Propeller diameter (m)	0.3046
Blade geometry pitch angle at r_b=0.75 (^{o})	41
Blade chord length at the root (m)	0.028
Hub diameter (m)	0.042

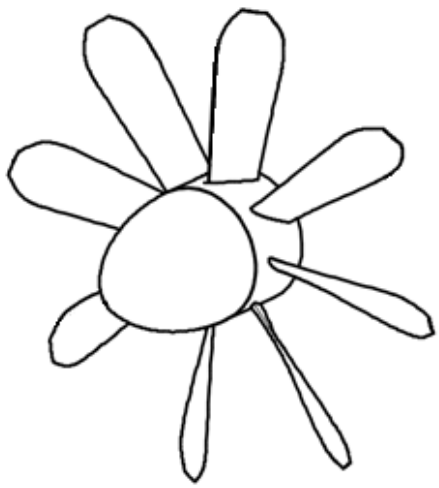

Figure 3.6: Three dimensional sketch of the F29 propeller

A 3-dimensional geometric profile of the F29 propeller model is presented in

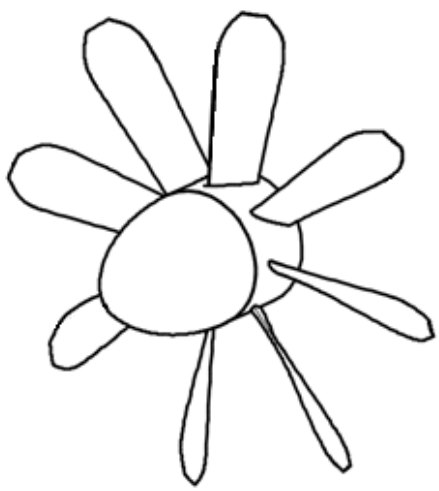

Figure 3.6. And the chord length and pitch angle distribution along blade span are presented in Figure 3.7. The chord length of each blade increases from the root until reaching the maximum value at radial position around 0.8R, then decreases at the tip part. And the pitch angle has the maximum magnitude at the blade root position, monotonically decrease with the radius increasing.

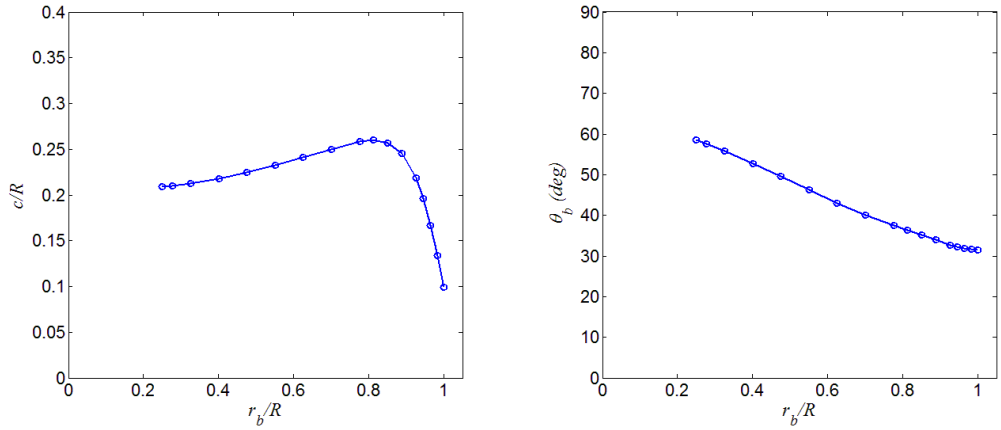

(a) chord length (b) Pitch angle

Figure 3.7: Distribution of the chord length and pitch angle along the span direction of the blade

3.2.3 Vortex Generator

In wind-tunnel tests, the impinging vortex was generated by a wing model with a cambered airfoil DU 96-W-180, which was designed for wind turbine applications[28]. The normalized airfoil profile is given in the website of Virginia Tech Aerospace and Ocean Engineering[29] and plotted in Figure 3.8. As well, the c_l-α curve for DU 96-W-180 is presented in Figure 3.9, which was obtained by Xfoil.

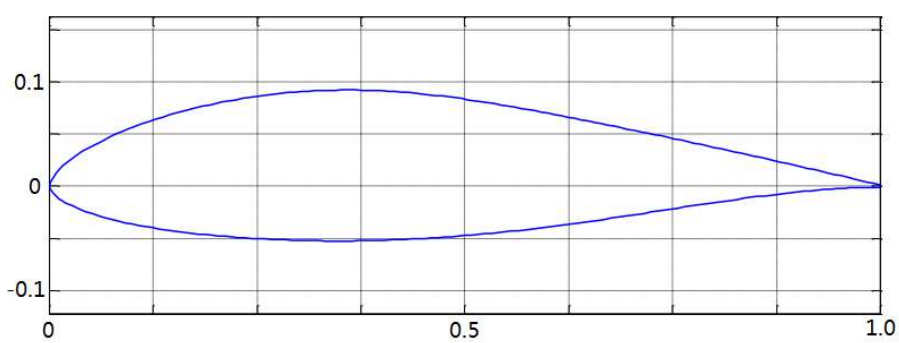

Figure 3.8: Profile of the DU 96-W-180 airfoil of the vortex generator

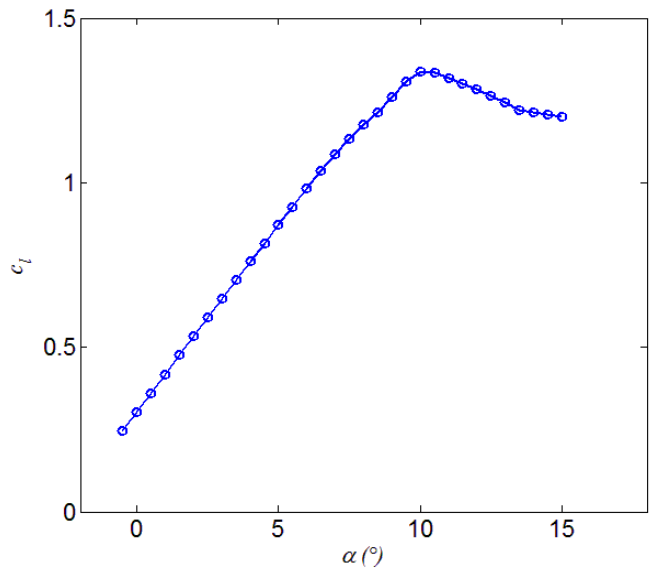

Figure 3.9: C_l-α curve of airfoil DU 96-W-180 (Re=3.3×10^5)

The wing utilized for vortex generation in the experimental research has a span-width of 1.0m, chord length of 0.25m. In order to diminish the effects of propeller to the vortex generator and reduce the influence of wake, the distance between wing model trailing-edge and the propeller blade leading-edge plane was kept as 800mm, which is around 3.5 times of the chord length of the wing. According to the PIV measurement result for an isolated vortex filament, it is already in a well-developed stage at this distance. A scheme illustrating the set up of vortex generator as well as the propeller is shown in Figure 3.10.

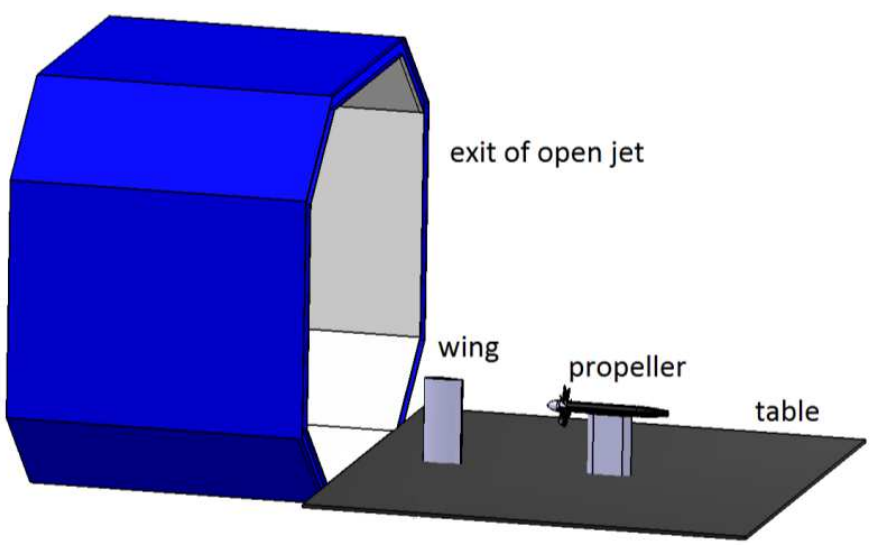

Figure 3.10: Set-up of the test in the wind tunnel

The wing angle of attack was adjusted by rotating through an axis mounted at the quarter point of its airfoil camber line. Since DU 96-W-180 is a cambered airfoil, the profile of wingtip vortex generated by the wing is not symmetrical about the zero angle of attack. In order to generated vortex with opposite rotational direction and maintain the same strength, the other end of the wing was also utilized to generate vortex. Thus, both two ends of this wing were used to produce vortex with opposite symbols.

3.2.4 Rotor Shaft Balance

The propeller was coupled with a six-component rotating shaft balance (RSB). A scheme of the structure of this balance is shown in Figure 3.11. Designed by National Aerospace Laboratory (NLR), this RSB measures time-average rotor thrust and torque produced by the propeller blades, hub and spinner.

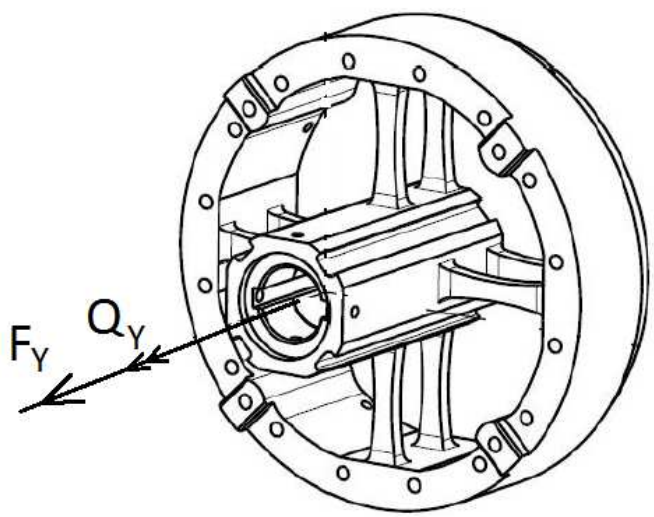

Figure 3.11: Rotor Shaft Balance

While the propeller is working, in the gap between its rotating and stationary parts, pressure is different from the ambient pressure. Such a pressure difference causes an extra axial force to the balance, leading to thrust measurement error. In order to correct that, a total number of 20 pressure ports were mounted to the back plate of the propeller hub to obtain an average pressure of the gap region. The corrected thrust is obtained by subtracting the force generated on the back plate from the RSB-measured thrust.

3.2.5 Set-up of particle image velocimetry measurement

Figure 3.12 shows the scheme of PIV measurement setup. According to the research objectives, there were two cross-sectional measurement planes selected: one was positioned $0.9c_{3/4R}$ (30mm) upstream of the propeller blade leading-edge plane, the other one was positioned $0.6c_{3/4R}$ (20mm) downstream of the blade trailing-edge plane. For measuring the upstream plane, the camera with forward scattering of the laser sheet was set at 42° with respect to the propeller axis, and the other camera was set at 44°. For measuring the downstream plane, the camera with forward and backward scattering of the laser sheet was set at 41° and 43°, respectively.

The selection of the axial positions of these two measurement planes were determined by trials and errors during the experiment preparation process. Although it is optimal to set the measurement planes as close as possible to the propeller disk plane, the distance cannot be smaller than the mentioned value due to a high signal to noise ratio in most of the measurement field.

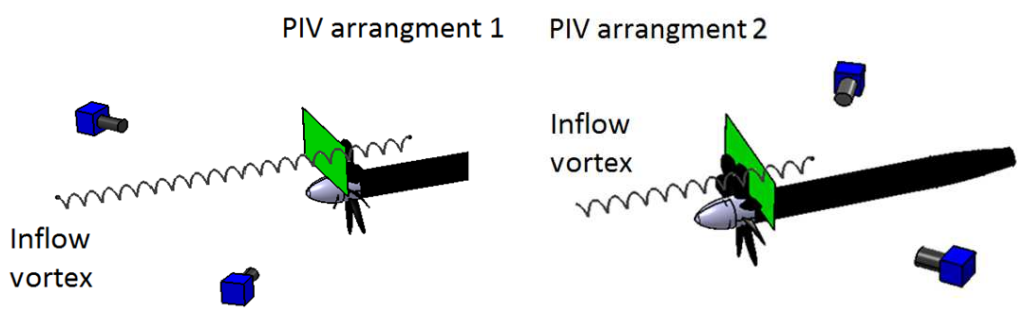

(a) Measurement plane upstream the propeller

(a) Measurement plane downstream the Downstream

Figure 3.12: Setup of PIV measurement

Two LaVision Imager Pro LX 16M high resolution CCD (CCD sensor of 4,870x3,246 pixels, 12 bit resolution, 7.4μm pixel pitch) were positioned in the level slightly higher than the height of the propeller hub. Spatially, the camera imaging windows were adjusted to the position allowing the horizontal middle line get aligned with the center of propeller. To measure flow in these two selected planes, cameras had to be mounted at different sides of the propeller disk plane, as shown in Figure 3.12. Due to the large dimension of the wind-tunnel, the distance between each camera and the target spot were more than 2.5m. In order to get higher image resolution, lenses with 200mm focal length were applied, creating measurement windows with resolution of 0.017R (2.557mm). Position and size of the windows are given in Figure 3.13.

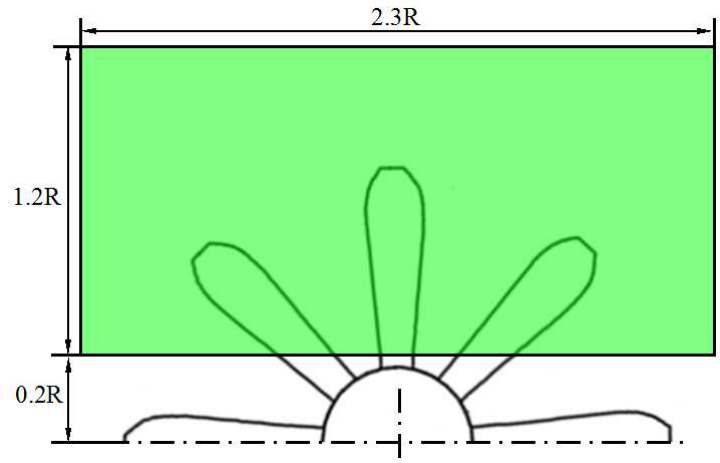

Figure 3.13: Field of view of the PIV measurement

The flow was seeded with micron-sized water-glycol particles produced by a SAFEX Twin Fog Double Power smoke generator, which was mounted in the wind-tunnel settling chamber. Particles illustration was provided by a double-pulsed Nd:YAG laser (Quantel Evergreen 200) emitting pulses with wavelength of 532nm, 200 mJ energy per pulse. The laser sheet had a thickness of 1.0mm, which was shaped by a group of lenses and mirrors. The laser and cameras were connected to a host computer via a Digital Delay Generator, which controlled the timing for triggering laser emitting and image acquisition.

3.3 Test matrix

In this project, the design of test matrix is based on the one-factor-at-a-time method (OFAT)[30]. Three parameters are thought to have effects on the interaction between propeller and the impinging vortex, which are the advance ratio of propeller J, vortex impinging radial position in propeller disk r_{imp}, and the vortex strength (represented by the vortex generator angle of attack) α_w. The experimental measurement matrix is shown in Table 3.2.

Table 3.2: Test matrix of PIV & RSB measurements

Case number	J	r_{imp}	α_w (°)
B	0.58-1.20	-	-
C1	0.58	0.74R	-8
C2	0.78	0.74R	-8
C3	1.10	0.74R	-8
C3	1.10	0.74R	-8
D1	1.10	0.83R	-8

D2	1.10	0.92R	-8
C1	0.58	0.74R	-8
E1	0.58	0.74R	8
E2	0.58	0.74R	-2
E3	0.58	0.74R	2

The inflow velocity in all the experiments is 19.0m/s. If the flow speed is too high, the density of particles used for PIV measurement would be too low to acquire results with high spatial resolution. Three advance ratios, 0.58, 0.78 and 1.10, were selected to investigate the effect of propeller loading. 0.58 is the condition in which propeller can generate the greatest thrust before blade stall. It can be considered as the maximum power condition in real aircraft situations, which usually occurs during taking-off. While 0.78 and 1.10 represent the median and low loading conditions of the propeller.

The radial positions of impingement are selected according to real situations. During ground operations, vortices shed from ground normally impinges into the propeller or engine inlet fan at outwards positions. The possibility of vortex impinging at a radial position smaller than 0.75R is very small[31]. Considering that, radial positions r_{imp}=0.74, 0.83 and 0.92 were selected to be investigated.

The strength of the impinging vortex was essentially decided by the vortex generation angle of attack α_w. The larger lift a wing can generated, the stronger the wingtip vortex would be. For the selected wing airfoil, DU 96-W-180, 8° is an angle of attack that is very close to the airfoil stall condition (as shown in Figure 3.9). And 2° is a smaller angle value selected for comparison. Note that the symbol of α_w is decided by the rotational direction of the wingtip vortex generated by the wing. Here define that when the vortex generated by the wing co-rotates with the propeller, the symbol of α_w is positive. For the other case, the symbol is negative.

3.4 Blade phase dependent research method

The dimension of the vortex core, comparing to the chord length of propeller blades, is much smaller. When the propeller blades rotate to different phase angles, it has different effects on the vortex column. Through propeller phase dependent analysis, the dependence of the vortex characteristics on propeller blade phase angles is investigated.

Denote the blade angle as Ψ. As shown in Figure 3.14, the phase angle of zero is defined when the symmetric line between two blades coincide with the O-Z axis. And define 45° as a phase angle period, which is denoted as T_Ψ. In the following chapters,

all phase angle will be given in dimensionless form, which is scaled by 45°.

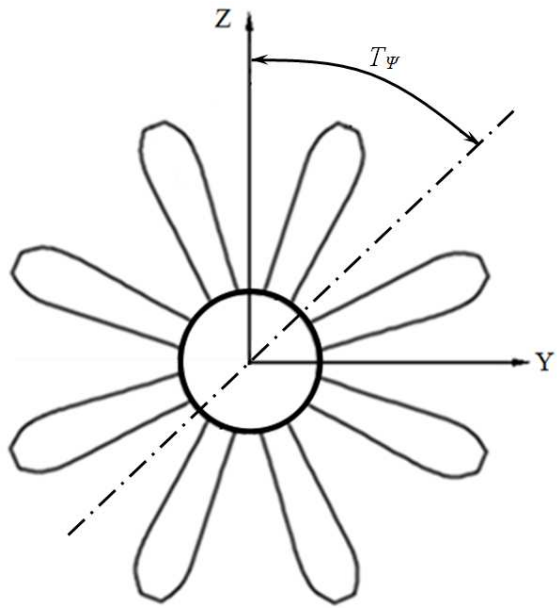

Figure 3.14: Definition of 0 phase angle

In PIV measurements, a commonly used phase dependent method is triggering laser and cameras together at the required blade phase angles by the signal from the propeller, which is called the synchronized PIV measurement. In this project, an alternative method, which takes use of the laser light reflected by the blade, was utilized. Procedures for conducting this alternative method is given following:

1) Divide the angle between two blades (45° for this applied propeller) into 8 phases. Fix one blade at every of these angles successively, take a PIV image for each of them. Due to the backward scattering of the laser sheet, light reflected by propeller blades on the images taken by the cameras has a corresponding relationship with each specific blade phase angle, as shown in Figure 3.15.

2) From all the PIV images acquired, search the images in which the blades is located at the position that indicates the required blade phase angles.

3) Work out required data and results from images that belong to each phase angle, respectively.

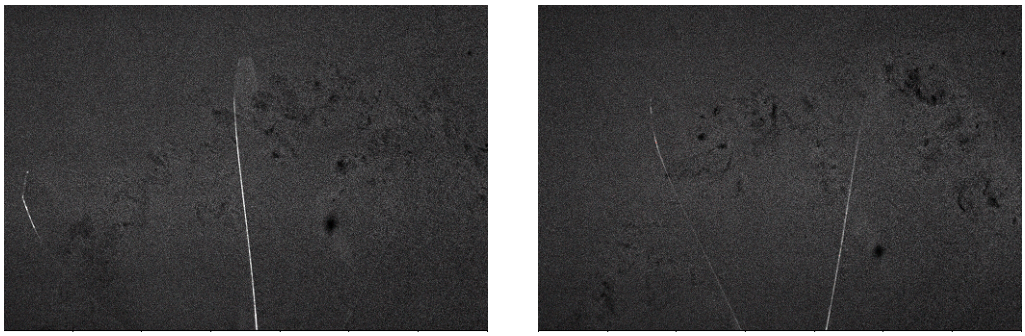

(a) $\Psi=0$ (a) $\Psi=0.5T_{\Psi}$

Figure 3.15: Light reflected by blades captured by camera.

Comparing with the synchronized PIV measurement, this phase angle dependent analysis method is not influenced by the fluctuation of the propeller rotational speed which affects the synchronization significantly. In addition, this method prevents repeated synchronized measurement at every phase angle for all measurement conditions given in the test matrix, which saves time.

4
Results and Analysis

4.1 Definitions and Parameters

Definition of the coordinate applied in this report is illustrated in Figure 4.1. This is a right handed coordinate system, in which the positive X-coordinate is set in the opposite direction to the flow stream. According to this, similar as the definition of the angle of attack of the vortex generator stated in section, symbols of vorticity and circulation of the impinging vortex are defined according to its relative rotational direction to the propeller. Thus, they are positive if the vortex co-rotates with the propeller; they have negative symbols for the counter-rotating case.

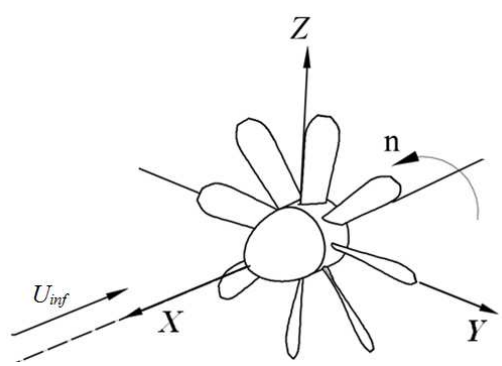

Figure 4.1: Definition of the coordinate system.

In this chapter, unless otherwise specified, all parameters used for presenting research results are given in dimensionless forms. Length volumes are non-dimensionalized by propeller radius R, velocities are non-dimensionalized by the infinite flow speed U_{inf}, vorticity and circulation are normalized by expressions (U_{inf}/R) and $(R \cdot U_{inf})$, respectively.

4.2 Impinging Vortex Profile

For the isolated vortex generated by the vortex generator with two angles of attack magnitudes, 2° and 8°, vorticity field together with streamlines are given in Figure 4.2. The contour is color-coded by the X-coordinate component of vorticity. And the radial profiles of these two vortexes are shown in Figure 4.3. For both these two angle of attack cases, the vorticity fields are symmetrical, and basically follow the Lamb-Oseen model introduced in section 2.3.2 .

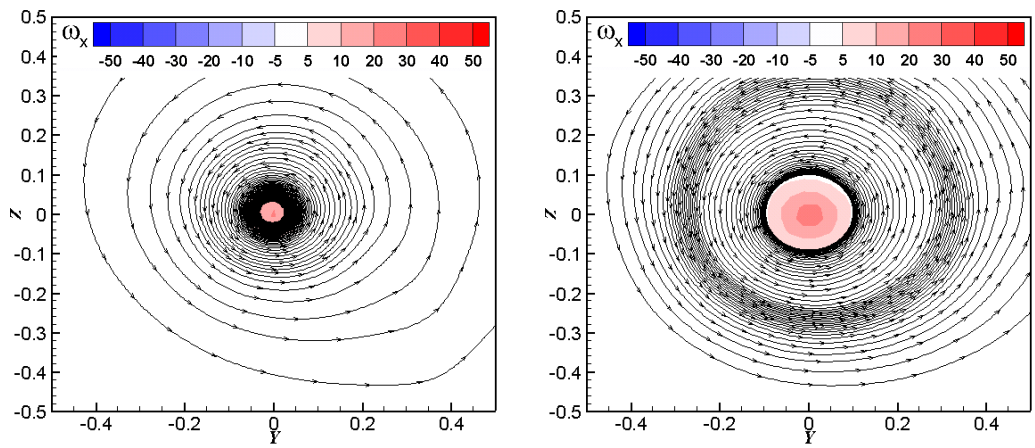

(a) α_w=2° (b) α_w=8°

Figure 4.2: Wingtip vortexes generated by vortex generator with different angles of attack, the flow field are contoured by the normalized vorticity in the axial direction.

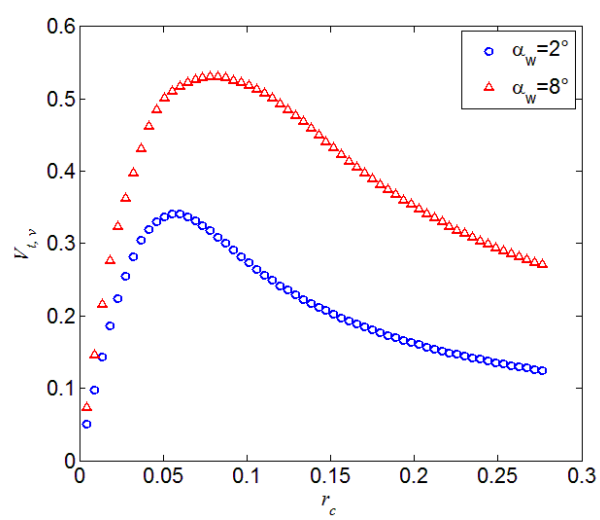

Figure 4.3: Distribution of the tangential velocity versus radial distance of the wingtip vortexes.

Characteristics of the vortices generated by the vortex generator with different angles of attack are given in Table 4.1, in which the vortex core circulation is calculated by the Stokes' theorem, written as

$$\Gamma_C = \int_{S_C} \omega_x dS \tag{4.1}$$

where Γ_C is the core circulation of vortex, S_C is the area of the vortex core in Y-Z plane, and ω_x represents the vorticity in X-coordinate. Note that here assumes that when the angles of attack of the vortex generator have the same magnitude but different symbols, the impinging vortex has opposite rotational directions but the same profile.

Table 4.1: Comparison of vortex characteristics for different angles of attack of the vortex generator .

	α_w=2°	α_w=8°
r_c	0.060	0.083
$V_{t,v,m}$	0.34	0.53
$\Gamma_{C,\,imp}$	0.128	0.275

4.3 Propeller performance

In this section, variations of the propeller performance obtained by both the experimental and numerical methods are presented. Base on the measurement matrix given in Table 3.2, the effect of propeller advance ratio, radial impinging position, vortex-propeller relative rotational direction and strength of the impinging vortex are discussed.

4.3.1 Corrections on the free stream velocity

For a propeller in an open jet wind-tunnel, due to the contraction of stream tube caused by the propeller, ambient air would be entrained from the region outside the wind-tunnel outlet area (as shown in Figure 4.4). It may cause the actual inflow velocity having a deviation from the wind-tunnel flow speed, resulting in an error added into the measured thrust.

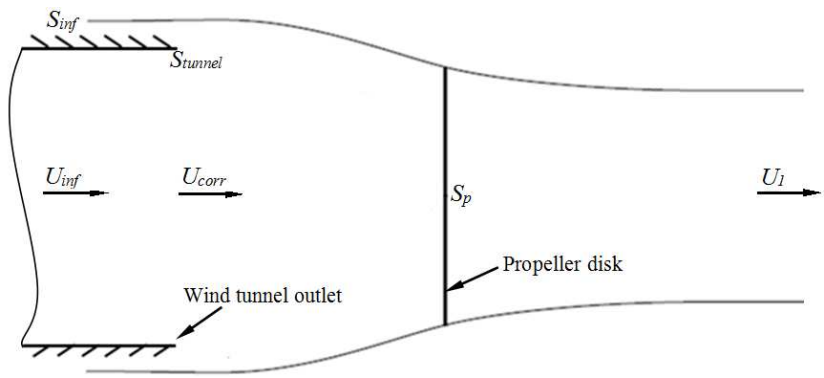

Figure 4.4: Scheme of the flow outside the exit of open tunnel entraining to propeller stream tube

A simplified correction is developed based on the correction for the case in a closed tunnel. Recognize the propeller as a sink, strength of the sink (mass flow) can be written as

$$\begin{aligned} q &= U_{\inf}\left(S_{\inf} - S_p\right) \\ &= U_{\inf} S_p \left(\sqrt{1+\frac{8}{\pi}\frac{C_T}{J^2}} - 1\right) \end{aligned} \tag{4.2}$$

where S_{inf} is the cross sectional area of the original inflow, S_p is the area of propeller. In an open tunnel, assume that the air outside the tunnel outlet maintains still, and the inflow velocity in the stream tube is a weighted average, then we have

$$U_{corr}\left[S_{tunnel} + \left(S_{\inf} - S_p\right)\right] = U_{\inf} S_{tunnel} \tag{4.3}$$

where S_{tunnel} is the cross-sectional area of the tunnel outlet, U_{corr} is the corrected inflow speed. Substituting Eq. (4.2) to Eq. (4.3), the corrected inflow speed can be expressed as

$$U_{corr} = U_{\inf} \frac{1}{1+\frac{S_p}{S_{tunnel}}\left(\sqrt{1+\frac{8}{\pi}\frac{C_T}{J^2}} - 1\right)} \tag{4.4}$$

Let

$$\frac{1}{1+\frac{S_p}{S_{tunnel}}\left(\sqrt{1+\frac{8}{\pi}\frac{C_T}{J^2}} - 1\right)} = 1+k \tag{4.5}$$

then the corrected thrust can be written as

$$T_{corr} = \dot{m}\left(U_1 - U_{corr}\right) = \dot{m}\left[U_1 - (1+k)U_{\inf}\right] = T_{mea} - \dot{m}kU_{\inf} \tag{4.6}$$

Note that with the corrected inflow velocity known, a corrected advance ratio can be

expressed as a function of the corrected inflow velocity, which is written as

$$J_{corr} = \frac{U_{corr}}{nD} \tag{4.7}$$

Apply the correction introduced above to the thrust measured in the wind-tunnel tests, a comparison of the originally measured and corrected thrust coefficient for an isolated propeller is shown in Figure 4.5. The error-bars are given with the experimental results representing the standard deviation of RSB measurement results. For C_T and C_Q, it is 0.07 and 0.003, respectively. Since the cross-sectional area of the exit of the wind-tunnel (7.56m^2) is much larger than the area of the propeller disk (0.07m^2), the corrected thrust are virtually equal to the measured thrust. Thus, the correction for thrust is not necessary in terms of the facilities utilized in this project.

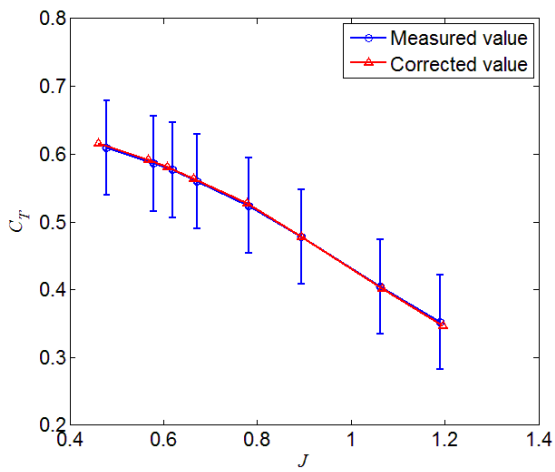

Figure 4.5: Comparison of the measured C_T and corrected C_T.

4.3.2 Impact of the wake of the vortex generator on the propeller performance

In the wind-tunnel tests, wing wake is always generated together with the wingtip vortex. In this project, since the vortex impinges upon the upper half of the propeller disk (as shown in Figure 3.12), the propeller performance is also influenced by the wake produced by the vortex generator. In order to estimate the impact of the wake on the propeller performance, a controlled test was conducted: raise the tip of the vortex generator to a level high enough that can make sure the wingtip vortex core going over the propeller disk from top and the whole disk being submerged in the wake flow. A comparison of C_T and C_Q for the isolated propeller and wake (produced by the vortex generator with α_w=8°) impinging cases are presented in Figure 4.6. Since for all the experimental conditions (given in Table 3.2), the region on propeller disk

influenced by the wake is smaller than that in the controlled test case, variations of the propeller performance caused by the wake would be smaller than that shown in Figure 4.6. Then it can be concluded that the impact of the wake on the propeller performance is so small that it can be neglected in the discussion of the effects of vortex impingement.

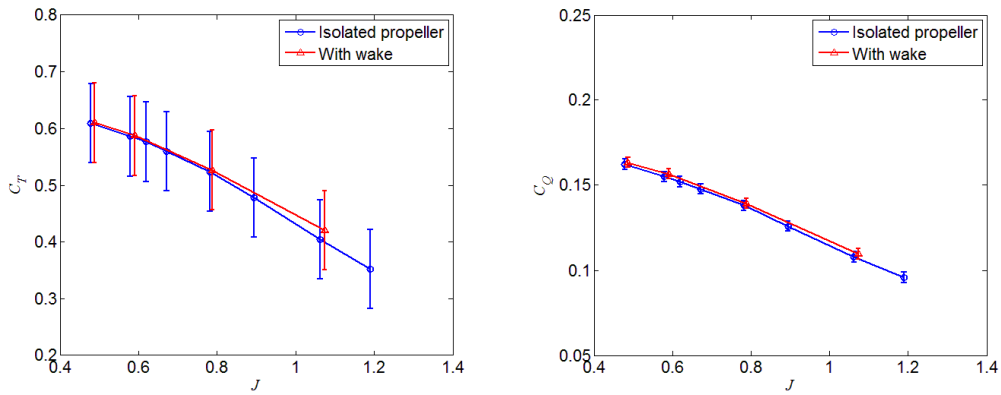

(a) C_T (a) C_Q

Figure 4.6: Impact of the wake produced by the vortex generator on the performance of the propelle. (α_w=8°)

4.3.3 Validation of BEM model

Before applying the BEM theory to simulate the impact of vortex impingement on the propeller performance, validation for the BEM model developed in Section 3.1 is necessary. Comparison of the experimental and numerical results for the thrust coefficient C_T, torque coefficient C_Q and efficiency η_{prop} of an isolated propeller are presented in Figure 4.7. The curves obtained by BEM theory show good agreement with those obtained from the experiments. Magnitude of C_T and C_Q obtained by the numerical method are larger than that obtained from wind-tunnel tests, with relative discrepancy of 2.5% and 5.5% in the low advance ratio region, respectively. However, the efficiency calculated by BEM theory is slightly lower than that of the experimental result. And for all these three parameters, between the numerical and experimental results, both the absolute and relative deviations increase with the propeller advance ratio increasing.

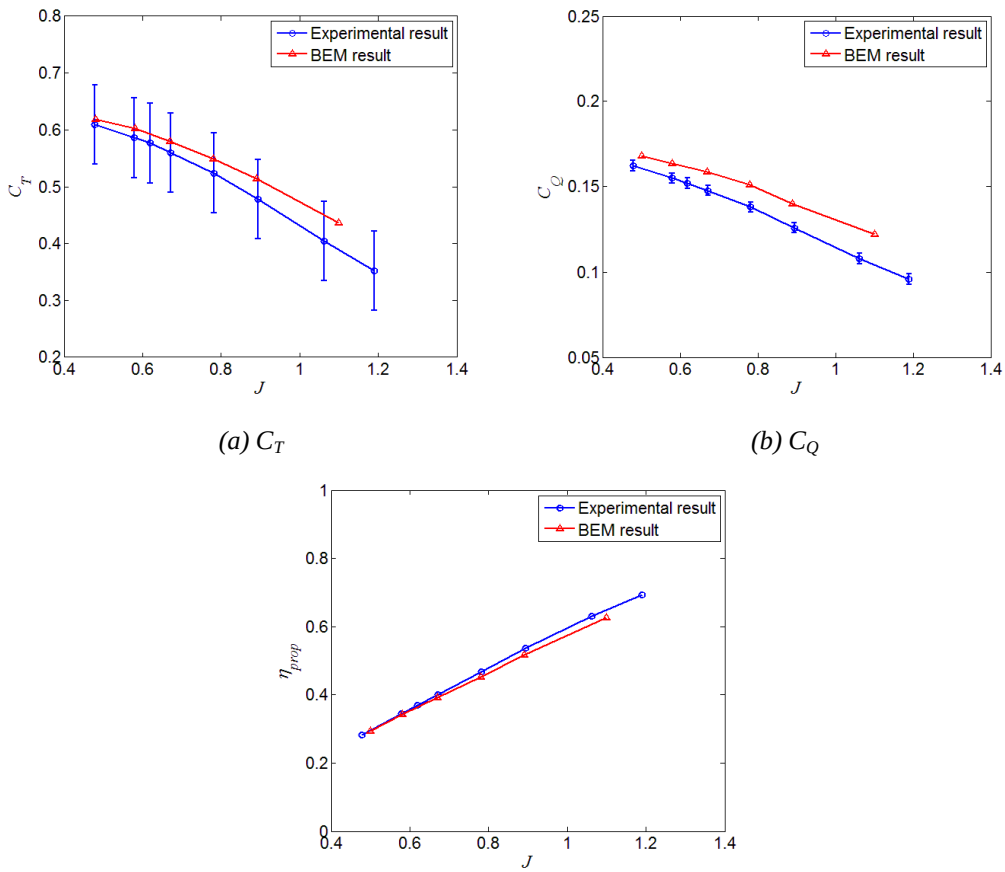

(a) C_T *(b)* C_Q

(c) η_{prop}

Figure 4.7: Comparison of propeller performance obtained from BEM theory and experiments. (J=0.58)

As stated in the section 3.1.2 , BEM theory can be applied to calculate the load distribution of propeller on the whole propeller disk. Figure 4.8 andFigure 4.9 show the load distribution along the radial direction for an isolated propeller with advance ratio of J=0.58. The contour figures are color-coded by the coefficients of normal force (dC_{Fx}) and out-of-plane component of moment (dC_{Mx}), respectively, which are defined as

$$dC_{Fx} = \frac{dT}{\rho n^2 \left(\frac{3}{4}D\right)^2 c_{3/4R}^2} \tag{4.8}$$

$$dC_{Mx} = \frac{dQ}{\rho n^2 \left(\frac{3}{4}D\right)^3 c_{3/4R}^2} \tag{4.9}$$

Note that in Figure 4.9, the values in y-coordinates are obtained by adding the load generated by all the elemental fractions in one annular ring. It presents the load distribution along the radial direction. For both dC_{Fx} and dC_{Fx}, the largest load occurs at the radial position r_b=0.87.

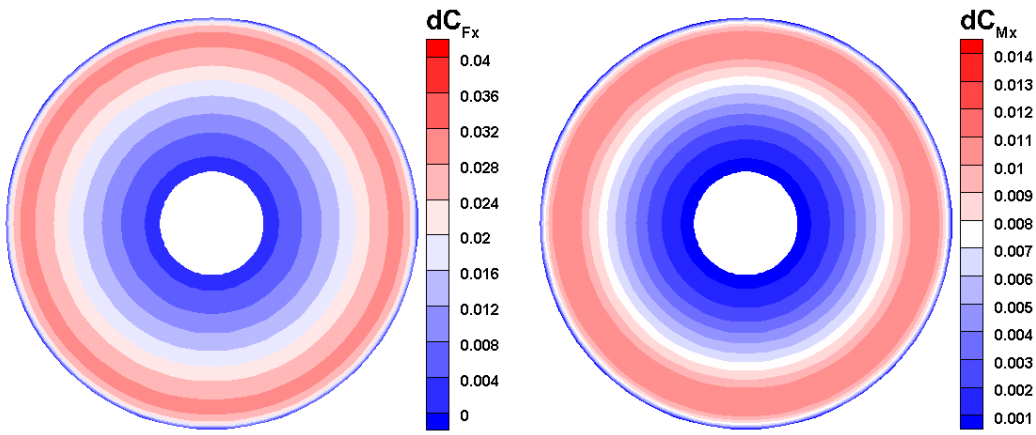

(a) dC_{Fx} (b) dC_{Mx}

Figure 4.8: Load distribution on disk for the isolated propeller . (J=0.58)

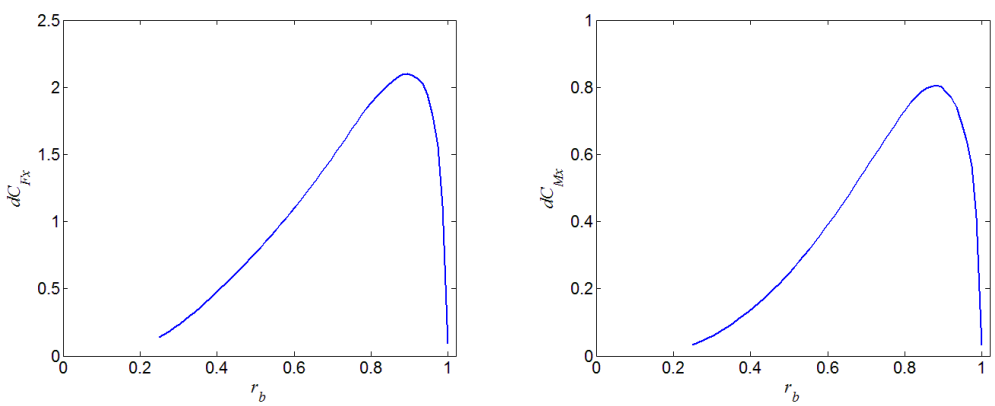

(a) dC_{Fx} (b) dC_{Mx}

Figure 4.9: Load distribution in the radial direction of the isolated propeller. (J=0.58)

4.3.4 Impact of vortex on the performance of propeller obtained from BEM theory

In this project, radial profiles of the tangential velocity of the impinging vortex used for numerical analysis are obtained from PIV measurement results. Table 4.2 shows the variation of propeller performance caused by vortex impingement, which are computed by BEM theory. Results for vortexes with opposite rotational directions are presented, with advance ratio J=0.58, and impinging radial position r_{imp}=0.74. Both

C_T and C_Q increase when a counter-rotating vortex column impinges into the propeller disk, and decrease for the co-rotating case.

Table 4.2: Variation of propeller performance caused by impinging vortex with opposite rotational directions. (J=0.58, r_{imp}=0.74)

$\Gamma_{C,\,imp}$	**-0.275**	**0**	**0.275**
C_T	0.620	0.602	0.578
C_Q	0.169	0.164	0.157

Contour of the elemental normal force and out-of-plane component of moment coefficient in the propeller disk plane for the cases $\Gamma_{C,\,imp}$=-0.275 and 0.275 are shown in Figure 4.10 andFigure 4.11, respectively. Significant load variation can be observed in the regions close to the vortex center. While in most parts of the propeller disk, the variation of performance is too weak to be evidently identified.

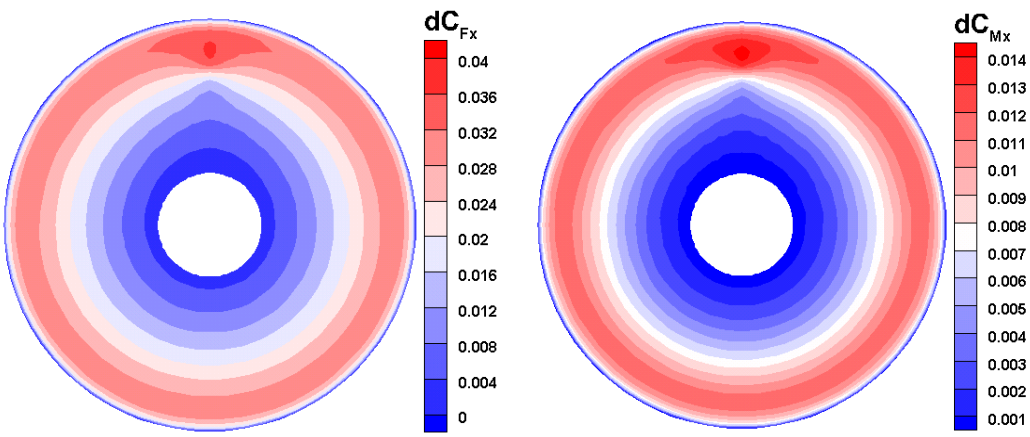

(a) dC_{Fx} (b) dC_{Mx}

Figure 4.10: Distribution of the coefficients of normal force and moment in the axial direction with counter-rotating vortex impingement ($\Gamma_{C,\ imp}$=-0.275, J=0.58, r_{imp}=0.74).

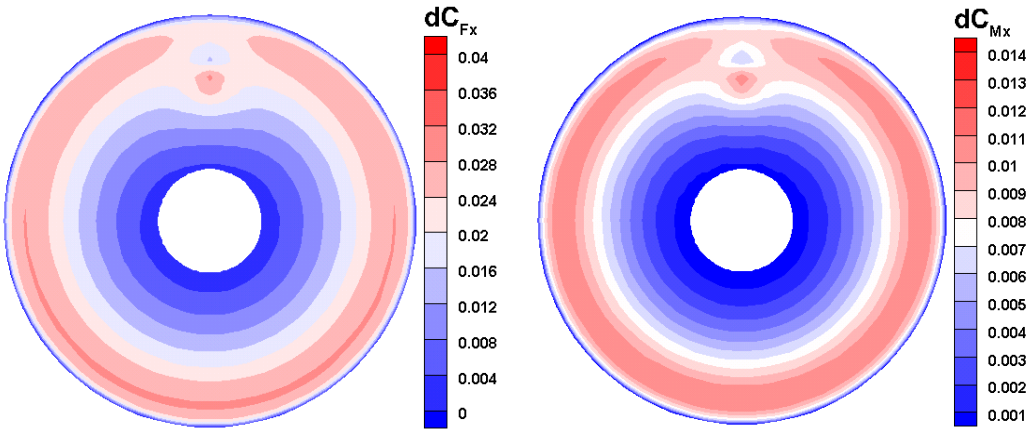

(a) dC_{Fx} (b) dC_{Mx}

Figure 4.11: Distribution of the coefficients of normal force and moment in the axial direction with counter-rotating vortex impingement ($\Gamma_{C,\,imp}$=0.275, J=0.58, r_{imp}=0.74)

To better illustrate the impact of the vortex impingement on the whole propeller disk, subtraction of the elemental load (ΔdC_{Fx} and ΔdC_{Mx}) on propeller disk for the cases with and without vortex impingement are shown in Figure 4.12 andFigure 4.13. The most significant load variation occurs at the regions that are close to the center of the impinging vortex, and opposite trends of variation are observed in the outward and inward sides of the vortex center. At the same position, impinging vortex with opposite rotational directions causes opposite trends of load variation.

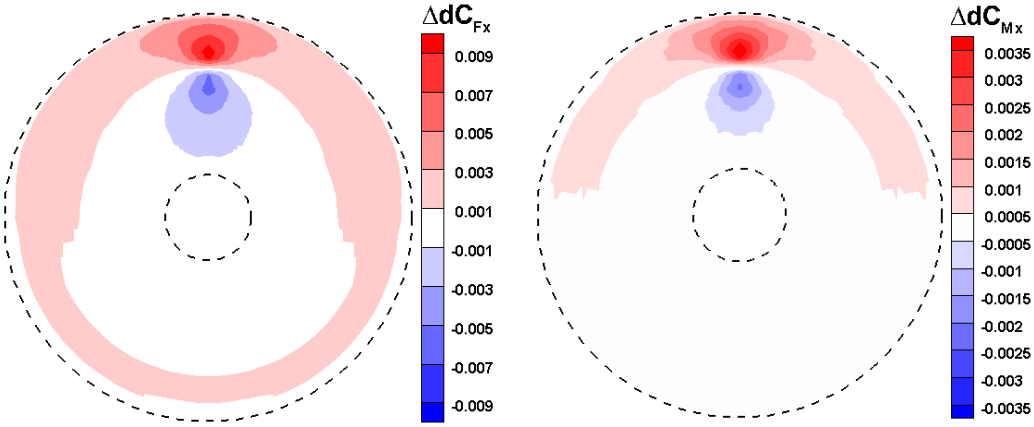

(a) ΔdC_{Fx} (b) ΔdC_{Mx}

Figure 4.12: Subtraction of the load on the propeller with vortex impingement by the case without vortex impingement. ($\Gamma_{C,\,imp}$=-0.275, J=0.58, r_{imp}=0.74)

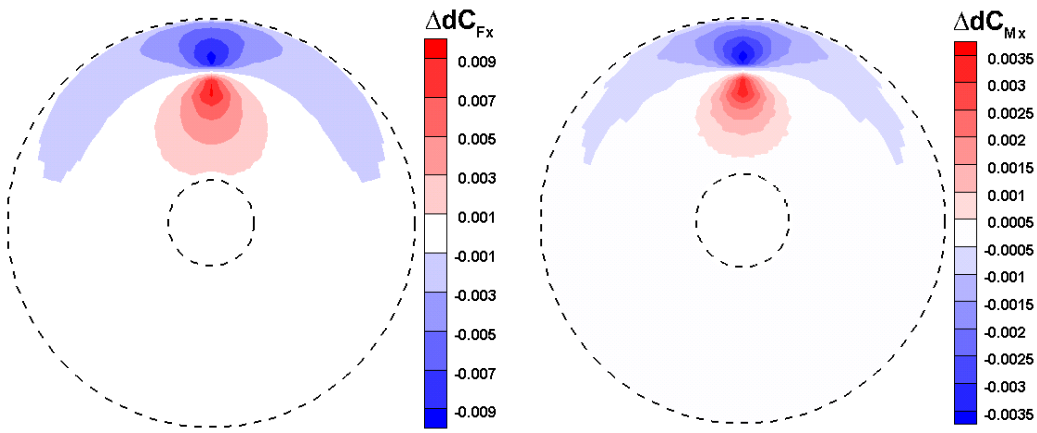

(a) ΔdC_{Fx} (b) ΔdC_{Mx}

Figure 4.13: Subtraction of the load on the propeller with vortex impingement by the case without vortex impingement. ($\Gamma_{C,\,imp}$=0.275, J=0.58, r_{imp}=0.74)

Comparison of the radial load distribution for the cases with and without vortex impingement is presented in Figure 4.14. Shapes of the curves for the radial load distribution are not changed significantly by the vortex impingement. Peak load still occurs near to the radial position r_b=0.87. However, load varies more evidently in the region whose radial position is larger than that of the vortex impinging position, which is consistent with the results shown in Figure 4.12 andFigure 4.13.

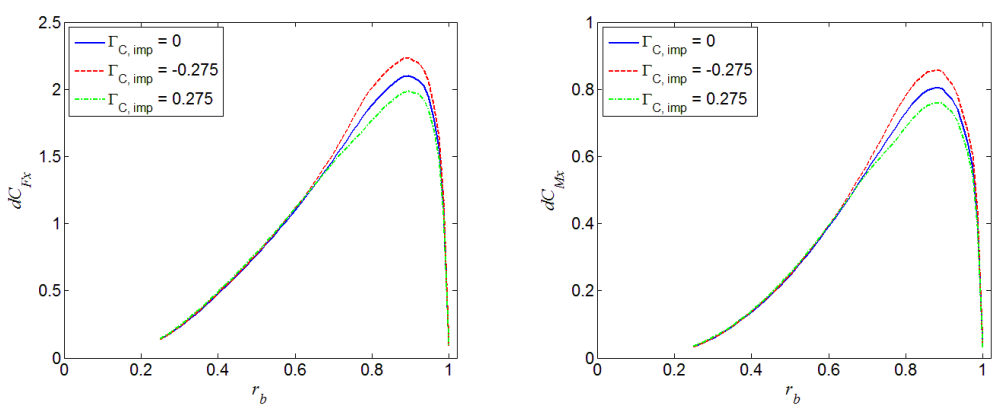

(a) dC_{Fx} (b) dC_{Mx}

Figure 4.14: Circumferentially averaged load distribution in the radial direction caused by impinging vortex with opposite rotational directions. (J=0.58, r_{imp}=0.74)

At the single elemental sector where the impinging vortex locates, load distribution along the radial direction is shown in Figure 4.15. For the coutern-rotating case)$\Gamma_{C,\,imp}$=-0.275), in the region outwards the radial position of vortex center (r_b>0.74), load

are much higher than that generated by an isolated propeller. In the rest part of this elemental sector (r_b<0.74), lighter load is observed. Oppositely, for the co-rotating case ($\Gamma_{C,\,imp}$=-0.275), variation of load distribution along the radial direction has the opposite trend.

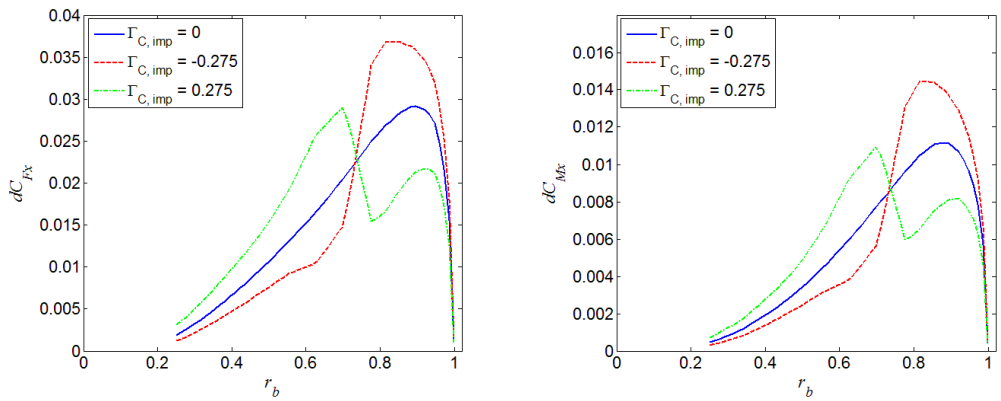

(a) dC_{Fx} (b) dC_{Mx}

Figure 4.15: Propeller load radial distribution in the elemental sector region in which the vortex impinges in. (J=0.58, r_{imp}=0.74)

Figure 4.15 illustrates the mechanism of the variation of elemental load caused by vortex impingement. For the counter-rotating case, in the region outwards the impinging position, vortex tangential velocity $V_{t,v}$ has the opposite direction with the tangential velocity of each cross section on blade, $V_{t,b}$. Vector addition of $V_{t,v}$ and $V_{t,b}$ results in a resultant tangential velocity V_t that is larger than $V_{t,b}$ and larger angle of attack for the corresponding cross section. Hence, increase of elemental load is observed in that region. However, in the region inwards from the impinging position, $V_{t,v}$ is in the same direction with $V_{t,b}$, which leads to lower V_t and angle of attack. And then decrease of elemental load is observed.

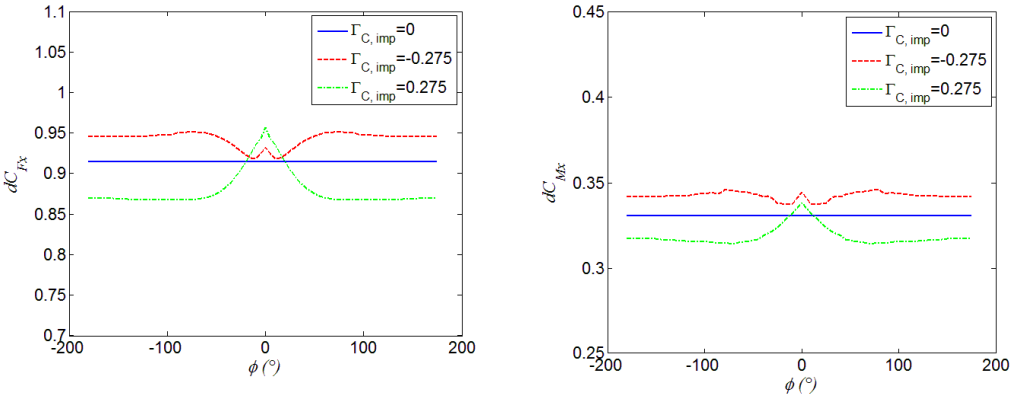

(a) dC_{Fx} (b) dC_{Mx}

Figure 4.16: Variations of azimuthal load distribution caused by vortex impingement. (J=0.58, r_{imp}=0.74)

Due to the impingement of vortex, the flow field upstream the propeller is no longer axisymmetric. Hence, the load distribution on the propeller disk is no longer axisymmetric, too (as shown in Figure 4.10Figure 4.11). Thus, at each elemental annular ring, the propeller load is not constant along the circumferential direction. Coefficients of the normal force and out-of-plane component of moment generated by each elemental sector in the propeller disk (as shown in Figure 3.4) are presented in Figure 4.16. Here define the circumferential position of the impinging vortex center is ϕ=0.

As shown in Figure 4.16, for the counter-rotating case, load generated by elemental sectors away from ϕ=0 is larger than that for the isolated propeller case; and vice versa for the vortex co-rotating case. Although the severest variation of load occurs at the elemental sector where the vortex center locates (as shown in Figure 4.13Figure 4.14), the load increase and decrease at different radial positions offset each other, resulting in relatively small variation of load on the corresponding elemental sector. Because of that, it is observed that the variation trend of the propeller performance is consistent with the variation trend of load observed at the elemental sectors that are away from the impinging position.

Notice that in Figure 4.16, the value of each data point is not equivalent to the coefficients of normal force or out-of-plane component of moment generated by a blade when it rotates to the corresponding azimuthal position. Instead, according to the derivation process illustrated in Section 3.1 , they represent the mean dC_{Fx} or dC_{Mx} generated at an elemental sector in one propeller rotational period. Thus, they are not instantaneous, but time averaged values.

4.3.5 Propeller performance variation

When the vortex impinges on the propeller, dependence of propeller performance on advance ratio is shown in Figure 4.17. Results acquired from BEM theory are presented in the same figures with the results acquired from RSB measurement to validate the numerical analysis method.

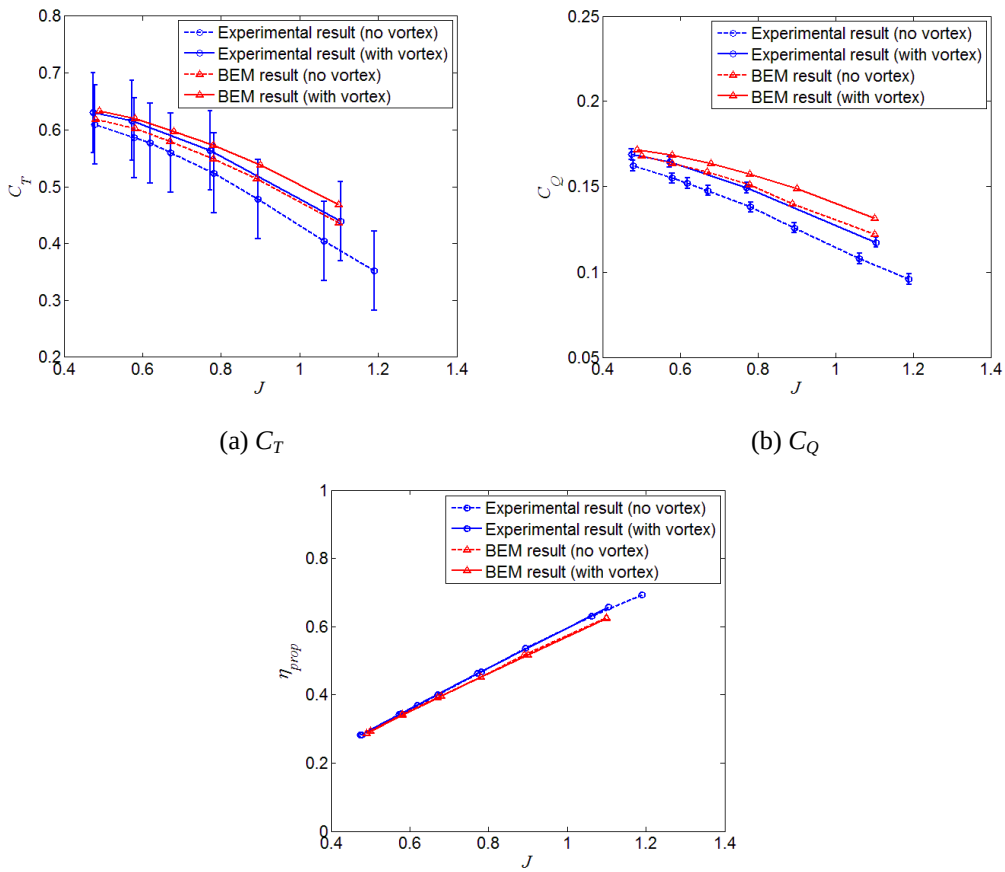

(a) C_T (b) C_Q

(c) η_{prop}

Figure 4.17: Impact of the impingement of counter-rotating vortex on the propeller performance. ($\Gamma_{C,\,imp}$=-0.275, r_{imp}=0.74)

As shown in Figure 4.17, comparing to the isolated propeller case, both the thrust and torque coefficient of the propeller increase, but the efficiency is independent from the impingement of vortex. The trends of the computational results, in terms of C_T and C_Q, are similar to that of the experimental result. At condition of low advance ratio, i.e. J=0.58, increases of C_T and C_Q due to vortex impingement from BEM theory are about 3%, while the results obtained from the experiments are about 4% and 6%, respectively.

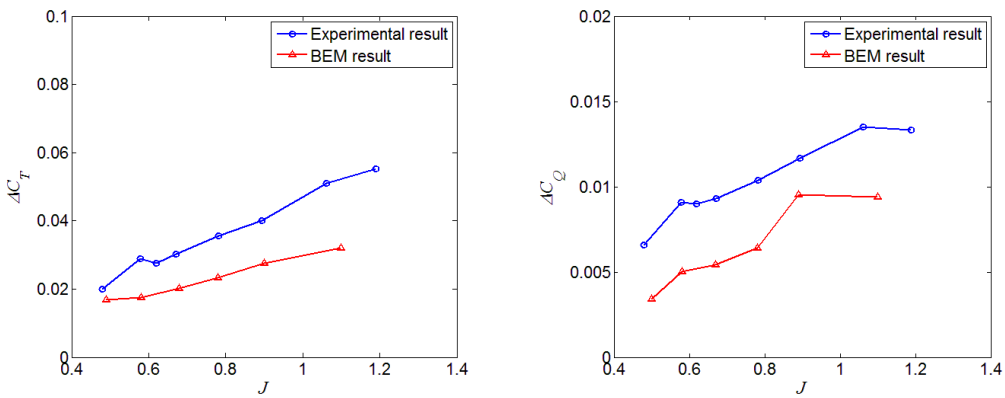

(a) ΔC_T *(b)* ΔC_Q

Figure 4.18: The increase of thrust and torque coefficient caused by vortex impingement. ($\Gamma_{C,\,imp}$=-0.275, r_{imp}=0.74)

The increase of thrust and torque coefficient caused by vortex impingement, ΔC_T and ΔC_Q, are presented in Figure 4.18. As the advance ratio increases, both ΔC_T and ΔC_Q increase. It is ascribed to the stall condition of the propeller blades. As stated before, vortex impingement changes the angle of attack at each cross section of the blade. At a high advance ratio condition, cross sections on the blade are below the stall condition. When a vortex filament impinges into the propeller, the increased local angle of attack is still below the range of stall. Consequently, the increase of thrust and torque is proportional to the increase of the angle of attack. However, at lower advance ratio condition, blade elements near to the maximum load area are closer to the range of stall. With their angles of attack increasing, on one hand, the thrust and torque coefficient of some of these cross sections increase proportionally; on the other hand, some of them reach the stall condition, which has a decrease of the thrust and torque. In total, the increase of the performance of propeller due to the impingement of a counter-rotating vortex at low advance ratio condition is not as much as that at high advance ratio condition.

Propeller performance versus the radial impinging position of vortex is presented in Figure 4.19. Experiments were performed for radial position of vortex at r_{imp}=0.74, 0.83 and 0.92; the numerical analysis has two more positions inwards. As shown in Figure 4.19, the curves obtained by experiments and BEM theory have a good agreement with each other.

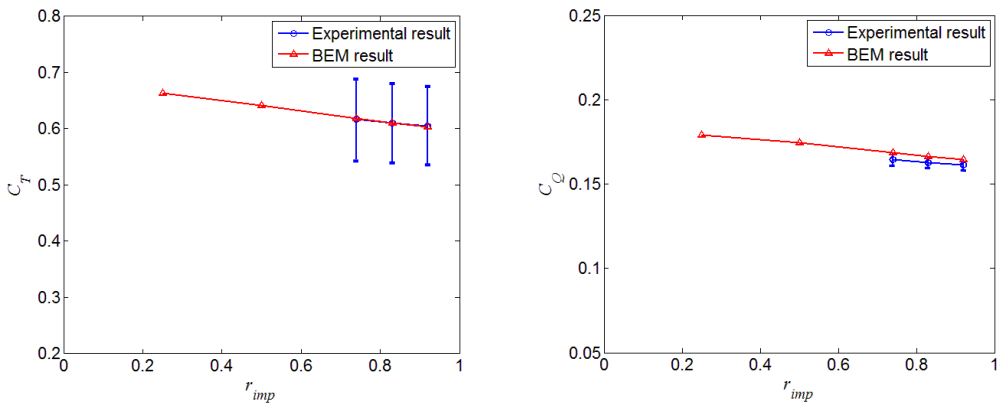

(a) C_T *(b)* C_Q

Figure 4.19: Performance of propeller versus radial position of vortex impingement. (J=0.58, $\Gamma_{C,\,imp}$=-0.275)

With a counter-rotating vortex impingement, both C_T and C_Q increase as the impinging position moves inwards. When the impinging position of vortex moves inwards, the inflection point shown in Figure 4.15 moves inwards. Consequently, the decreased region of load reduces and the increased region of load increases. In the sectors that are far from the position where the vortex impinges, the inward moving of impingement position decreases their distances to the vortex core center, leading to larger resultant vortex tangential velocity. Hence, the load increase in these sectors becomes more significant. Combining all these effects, with a counter-rotating vortex impinging, the propeller performance increases as the vortex impingement position moves inwards.

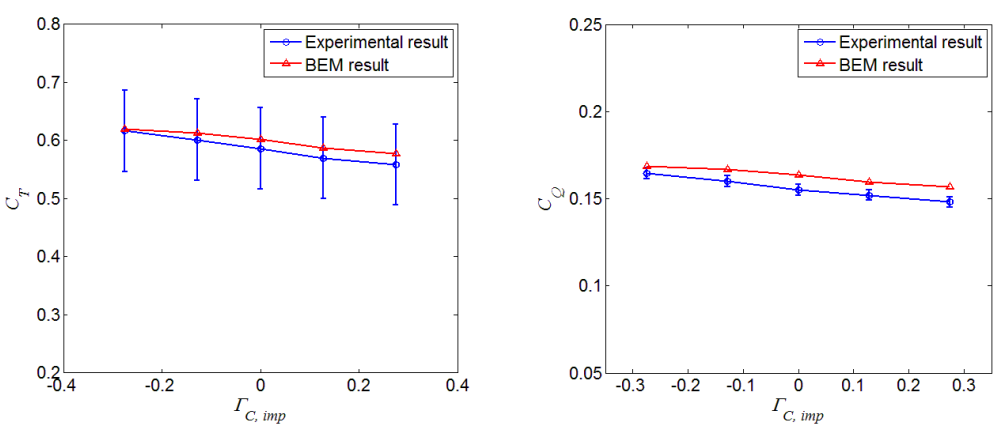

(a) C_T (b) C_Q

Figure 4.20: Dependence of thrust and torque coefficient on the strength of the impinging vortex. (J=0.58, r_{imp}=0.74)

Dependence of propeller performance on the impinging vortex strength is shown in Figure 4.20. Zero point on the x-coordinate represents the case of isolated propeller without vortex impingement. It is evident that the variation of propeller performance caused by vortex impingement becomes more significant as the strength of vortex increases. And similar as the results shown in Figure 4.17, the performance obtained by the numerical method is larger than that acquired from experiments.

4.4 Vortex development through the propeller

Development of vortex filament from the flow field upstream to downstream the propeller is of interest for the concern of propeller impact on the impinging vortex. With the help of PIV measurements, two flow fields which involve the vortex are resolved to analyze the properties of vortex. Effects of the swirling direction of the vortex, propeller load (advance ratio) and radial position of impingement, on the response of vortex, will be discussed.

4.4.1 Variation of vortex behavior through propeller disk

To investigate the variation of vortex characteristics between the flow fields upstream and downstream the propeller disk, results obtained from one single experimental condition (propeller advance ratio J=0.58, radial position of vortex impingement r_{imp}=0.74, and vortex core circulation $\Gamma_{C,\,imp}$=-0.275) are presented in this section.

4.4.1.1 Variation of vortex profile

Figure 4.21(a) shows the time averaged vorticity field involves impinging vortex superimposed by the streamlines in the measurement plane upstream the propeller. Center of the impinging vortex is observed at position (-0.001R, 0.728R). Two semi-circles in dashed lines show the projection of the propeller, which are centered at propeller axis, and have radius of the propeller blade and hub, respectively. Radial profile of the tangential velocity is shown in Figure 4.21(b), where the maximum tangential velocity is 0.64, achieved at vortex radius r_c=0.069. With the vortex radius known, we have the vortex core circulation is -0.277.

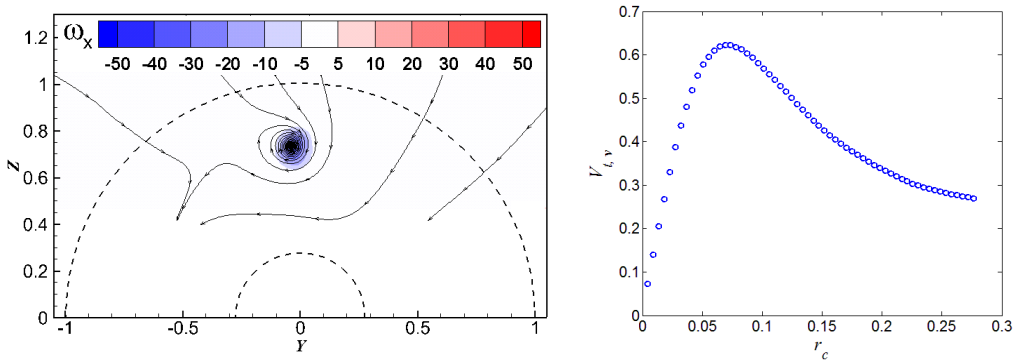

(a) Vorticity field (b) Radial profile of tangential velocity

Figure 4.21: Vorticity field and radial profile of tangential velocity. (upstream, J=0.58, r_{imp}=0.74, $\Gamma_{C,\,imp}$=-0.275)

As comparison, Figure 4.22 presents the vorticity field measured in the plane downstream the propeller disk. At each phase angle, the instantaneous position of blades are given together with the contour figures of vorticity. Since the induced tangential velocity in the flow field downstream the propeller disk is much lower than the rotational speed of the propeller blade, there is a large difference of phase angle between the blade and its wake vortices. Notice that since the rotational speed of propeller is constant, that difference of phase angle is also constant at each phase angle situation.

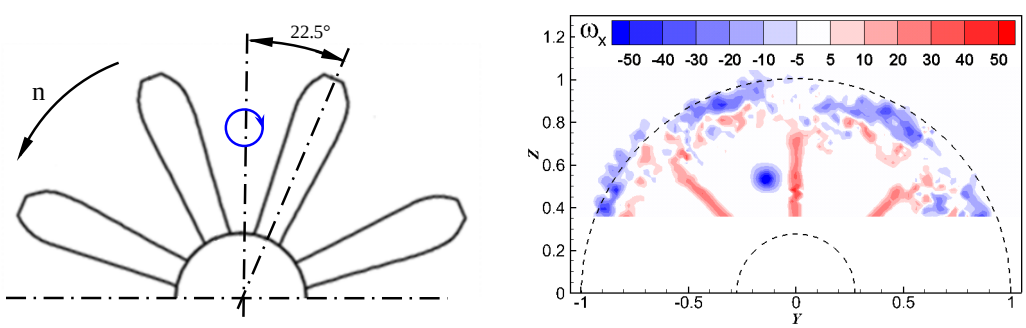

(a) Ψ=0

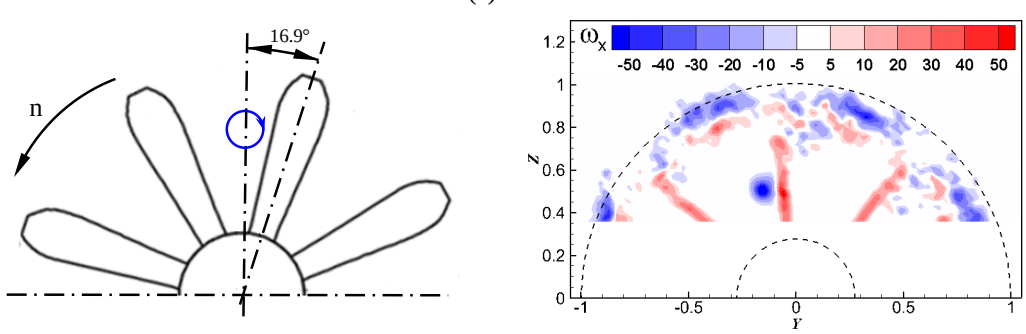

(b) $\Psi=0.13T_{\Psi}$

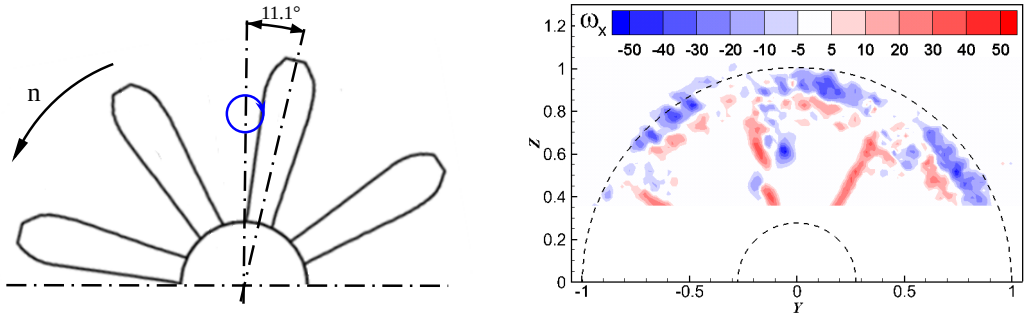

(c) $\Psi=0.25T_{\Psi}$

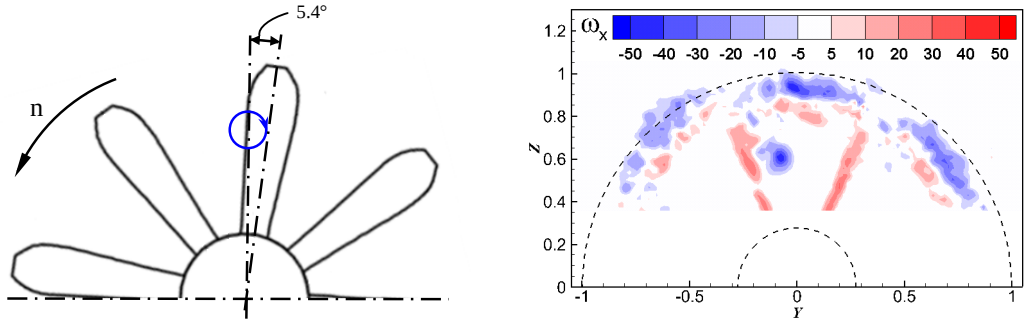

(d) $\Psi=0.38T_{\Psi}$

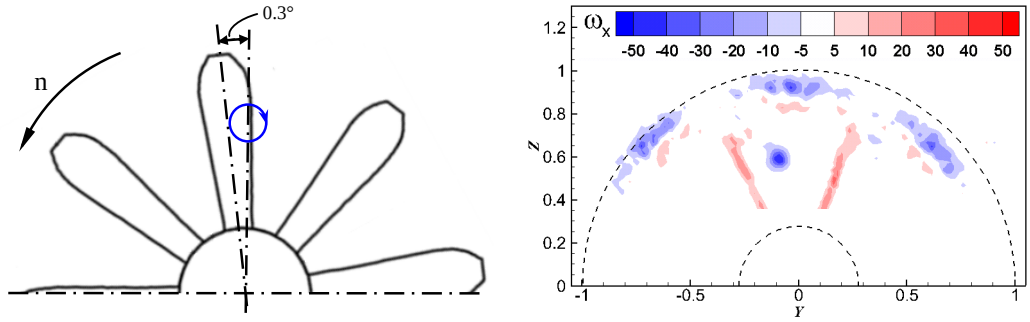

(e) $\Psi=0.50T_{\Psi}$

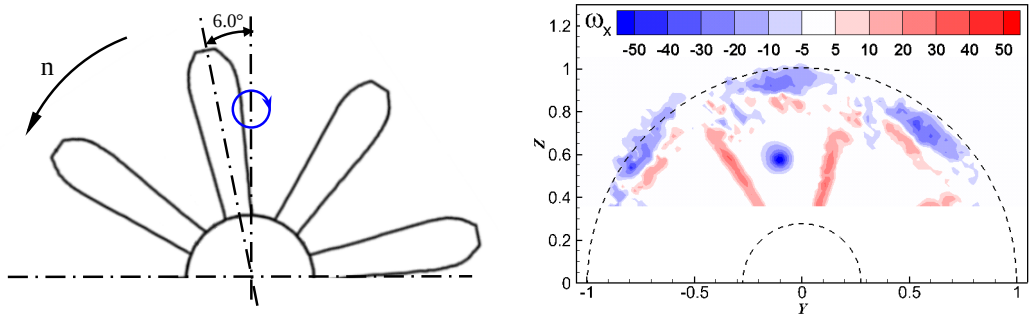

(f) $\Psi=0.63T_{\Psi}$

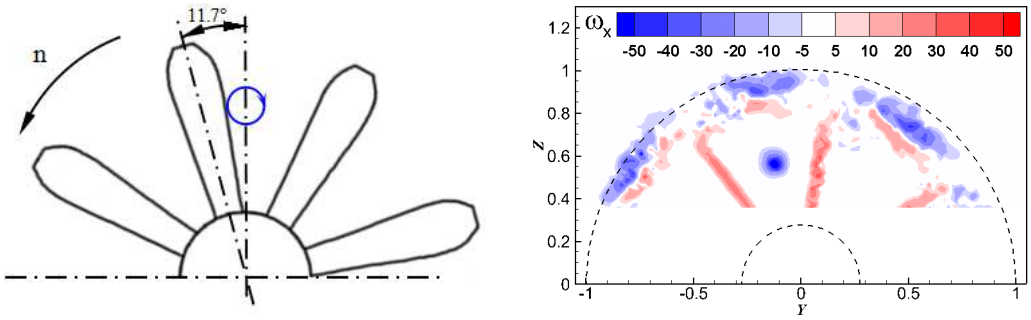

(g) Ψ=0.75T$_\Psi$

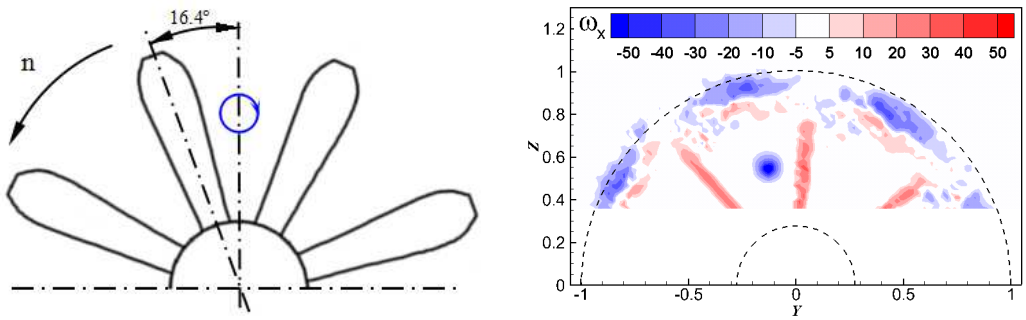

(h) Ψ=0.83T$_\Psi$

Figure 4.22: Dependence of the vorticity field on the blade phase angle. (downstream, J=0.58, r_{imp}=0.74, $\Gamma_{C,\,imp}$=-0.275)

As shown in Figure 4.22, in the measurement plane downstream the propeller, the impinging vortex is observed at the negative side of the Y-coordinate. As the blade rotates, position of the vortex center wanders within a certain range. As well, the vorticity magnitude of the vortex core region is evidently larger than that observed in the plane upstream the propeller. Variation of the position of vortex center and increase of vorticity observed in the flow field downstream the propeller will be discussed in details in Sections 4.4.1.2 and 4.4.1.3 .

At the phase angle Ψ=0.25T$_\Psi$, as shown in Figure 4.22(c), the propeller blade wake vortices rotates to the position that coincides with the impinging vortex. At this moment, the impinging vortex is “broken” into two fractions by the blade wake vortices. The smaller fraction is still maintained close to the position of the vortex core observed at Ψ=0.13T$_\Psi$ (Figure 4.22(b)); the other fraction locates in vicinity to the position of the vortex core shown in Figure 4.22(d). Furthermore, when Ψ=0.25T$_\Psi$, the vortices in the blade wake is also split into two pieces by the impinging vortex, as shown in Figure 4.22(c).

Essentially, the “broken” of the blade wake vortices and the impinging vortex is a result of the interaction between two counter-rotating vortices. For a pair of opposite-sign vortices, within the stability margin, as one approaches, the other one

has a trend to deform and move to the opposite direction. Within the critical distance, one or both of them would be broken into two ore more smaller fractions by the other one[32][33]. For the impinging vortex shown in Figure 4.22(c), since being broken into two parts, the vorticity of each of them is lower than that observed in other phase angle conditions.

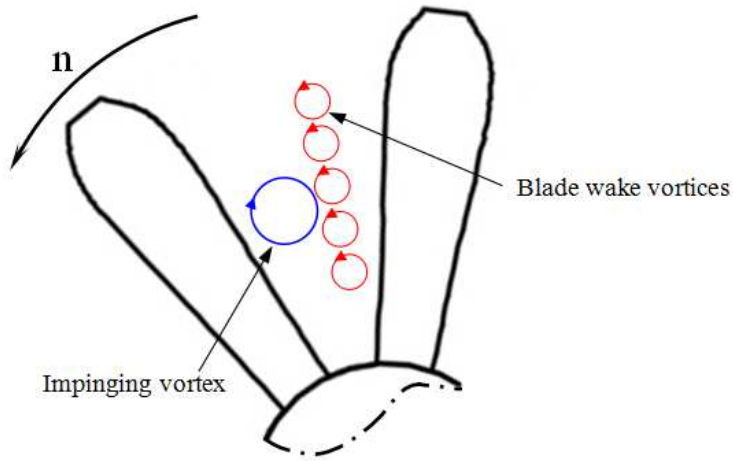

Figure 4.23: Scheme of blade wake vortices and the impinging vortex

4.4.1.2 Variation of vortex center positions

Due to the contraction of stream tube and induced tangential velocity caused by propeller, the impinging vortex filament locus is bent as it progresses through the propeller disk, as shown in Figure 4.24. The locus bending causes the displacement of the mean vortex center position observed between the measurement planes upstream and downstream the propeller.

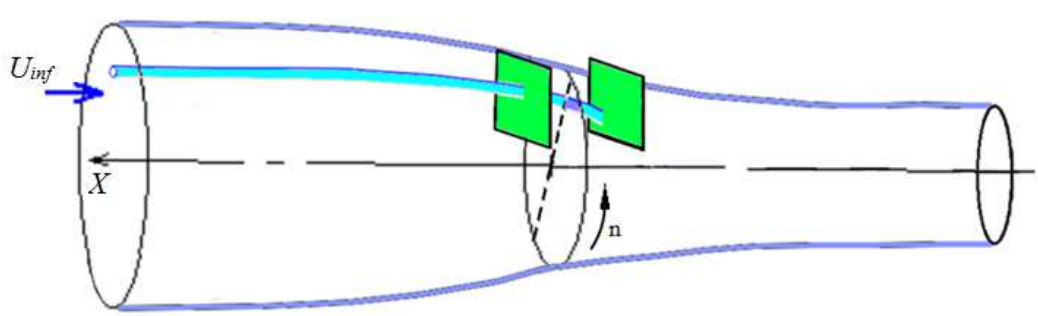

Figure 4.24: Locus of the vortex filament

Comparison of the instantaneous and mean positions of vortex center in two PIV measurement planes is shown in Figure 4.25, which is illustrated in the polar

coordinate system centered by the propeller axis. In the plane upstream the propeller, vortex is not significantly influenced by the propeller, the instantaneous positions fo vortex center meander in a very small vibrational amplitude (Figure 4.25(a)), which is ascribed to the wandering of wingtip vortex[34][35]. However, in the flow field downstream the propeller, after being affected by propeller blades, the instantaneous positions of vortex center do not meander equally in radial (*r*)- and circumferential (*θ*)-coordinate any more. As shown in Figure 4.25(b), it forms a stretched distribution region, which lays from top-left to bottom-right. The mean position of vortex center, comparing to that shown in Figure 4.25(a), moves inwards and rotates in the counter-clockwise direction.

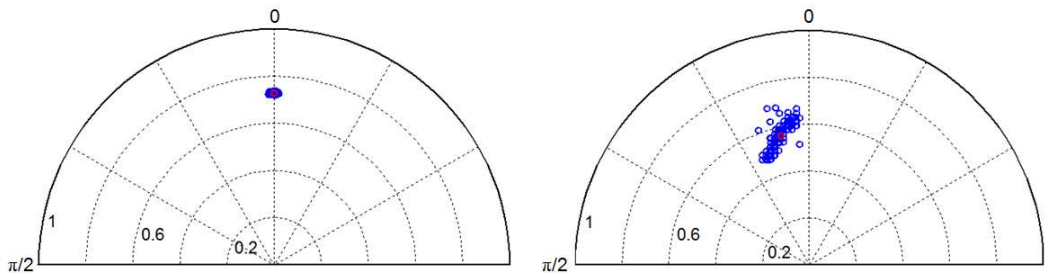

(a) Upstream plane (b) Downstream plane

Figure 4.25: Comparison of mean and instantaneous positions of vortex center in the measurement planes upstream and downstream the propeller. (J=0.58, r_{imp}=0.74, Γ_C=-0.275)

The statistical results of the instantaneous positions of vortex center are given in Table 4.3. In both *r*- and *θ*-coordinate, the standard deviation in the measurement plane downstream the propeller is about one order higher than that measured in the other plane. Being consistent with the result observed in Figure 4.25, it indicates that in the flow field downstream the propeller, the instantaneous position of vortex center has a larger meandering amplitude. To better understand that phenomenon, mean positions of the vortex center under each blade phase angle are computed and presented in Figure 4.26.

Table 4.3: Statistical comparison of instantaneous vortex center positions. (J=0.58, r_{imp}=0.74, $\Gamma_{C,\,imp}$=-0.275)

	Mean position of vortex center		**standard deviation of the *r*-coordinate**	**standard deviation of the *θ*-coordinate**
	r	***θ***		
Upstream plane	0.728	0.001	0.0038	0.0062
Downstream plane	0.565	0.216	0.0429	0.0797

As shown in Figure 4.26, at the moment before the blade wake vortices coincide with the impinging vortex core (Ψ=0.13T_Ψ), the vortex center position has the largest displacement with respect to the vortex impingement position measured in the plane upstream the propeller. After that, at Ψ=0.25T_Ψ, the vortex center "jumps" back to the position that is nearest to the impingement position. Afterwards, with the blade phase angle increasing, vortex center moves in the inward-counter-clockwise direction gradually, and finally reaches the farthest position again at Ψ=0.13T_Ψ. Thus, in the flow field downstream the propeller, the impinging vortex center position varies periodically.

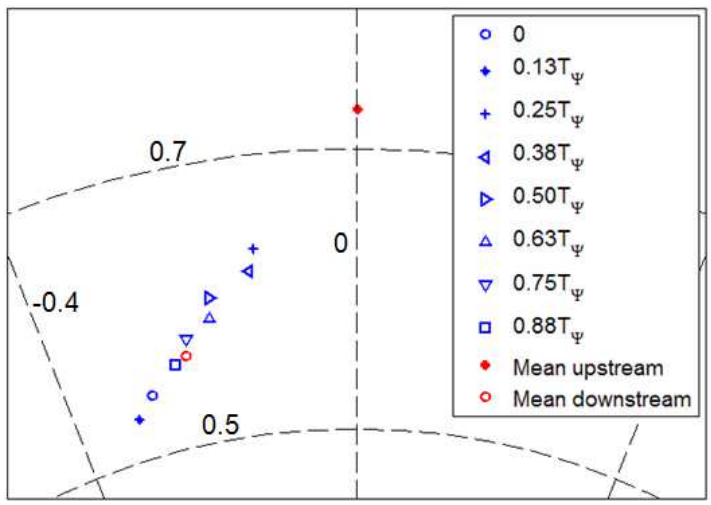

Figure 4.26: Dependence of the position of vortex center on the blade phase angle. (downstream, J=0.58, r_{imp}=0.74, $\Gamma_{C,\,imp}$=-0.275)

With the thrust measured by RSB, the radial displacement of the mean position of vortex center caused by the contraction of stream tube can be roughly estimated. According to Eq. (3.12), we have the mean axial induced velocity is about 12.0m/s. Based on the momentum theory, the ratio between the cross-sectional radius of the stream tube at the propeller disk and that at the axial position infinite upstream is about 0.8. Assume the radial distribution of axial velocity does not change in different cross sections of the stream tube, we have the radial position of the vortex center in the plane downstream the propeller is about 0.58R.

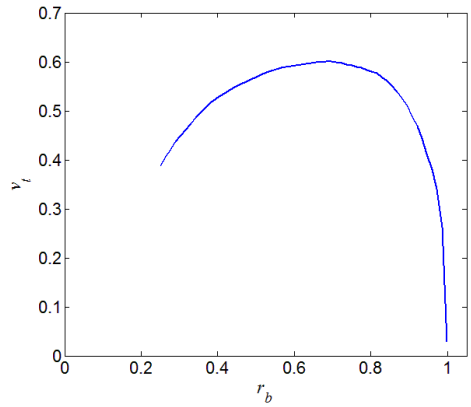

Figure 4.27: Distribution of induced tangential velocity in the radial direction for the isolated propeller case. (acquired by BEM theory)

In the circumferential direction, displacement of the mean position of vortex center can be estimated by the the induced tangential velocity. According to the design parameters of the propeller and the experimental setup given in Section 3.2 , the axial distance between these two PIV measurement planes is about 0.048m. Considering magnitude of the axial induced velocity, we have the time for the vortex to progress from the blade leading-edge to the measurement plane is about 0.0015s. Use the induced tangential velocity at the propeller disk (given by BEM theory as shown in Figure 4.27) as the mean tangential velocity between the two measurement planes, we have the circumferential displacement of the vortex center is about 0.016m, which is about 0.25 in the θ-coordinate.

The estimation given above is virtually consistent with the results obtained by PIV measurement. Then it can be concluded that the tangential induced velocity and the contraction of stream tube are two prime factors that account for the displacement of the mean position of vortex center between these two measurement planes. However, the dependence of vortex center position on blade phase angles shown in Figure 4.26 cannot be explained by that. Instead, it is a result of the interaction of vortices.

Assume a case that there is no blade wake vortices existing in the flow field downstream the propeller. Because of the induced tangential velocity and the contraction of stream tube, the instantaneous position of vortex center would always locates near to the mean position. However, with the wake vortices being generated, interaction between the impinging vortex and the wake vortices occurs as they age downstream from the blade trailing-edge. At phase angles Ψ=0.38-0.75T_Ψ, the approaching blade wake vortices have the prime influence on the impinging vortex. The vortex core is forced to move away from the mean position in the blade rotating direction. At the moment the blade wake vortices coincide with the vortex core

(Ψ=0.25T_Ψ), it breaks the impinging vortex into two smaller patterns, which moves the impinging vortex (which is recognized as the pattern with larger vorticity) to the position that is farthest from the mean position. Afterwards, at the phase angles Ψ=0.88-0.13T_Ψ, it is the leaving blade wake vortices that have the most significant effect on the impinging vortex. Since it rotates away, the impinging vortex gradually moves back to the mean position.

Additionally, the dispersion of the vortex center position in *r*-coordinate can be explained by Biot-Savart law, which describes the velocities induced by 3-D vortices lines. Assume the blade wake vortices consist of many small-radii vortices which are infinite long in the axial direction. According to Biot-Savart law given by Eq. (2.26), in the Y-Z plane, velocities induced by these vortices have directions as shown in Figure 4.28. At different sides of the blade wake, the induced velocities in the *r*-coordinate have opposite directions.

As one wake vortices sheet approaches, in the view given in Figure 4.22, the impinging vortex filament locates at the left side of the blade wake vortices. In the Y-Z plane, velocities induced by the wake vortices at the position of the impinging vortex point to the propeller axis. Magnitude of the induced velocity increases with the distance decreasing, leading to a further inward radial position of the vortex core. Once the blade wake rotates through the impinging vortex core, the radial component of the induced velocities points outwards. As the wake vortices sheet rotates away, magnitude of the induced velocities decreases, hence the radial displacement of the vortex center from the mean position becomes smaller.

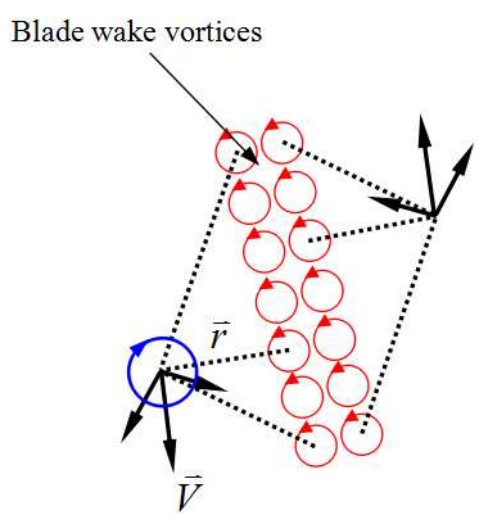

Figure 4.28: Scheme of the velocities induced by the blade wake vortices.

4.4.1.3 Variations of vortex core radius and circulation

As shown in Figure 4.22, in the flow field downstream the propeller, profile of the impinging vortex is not always axisymmetric. Considering that, the vortex core radius is defined by the radial position where the maximum mean tangential velocity in the circumferential direction achieved. Dependence of vortex core radius on the blade phase angle is presented in Figure 4.29. Generally, in the plane downstream the propeller, the vortex radius is smaller than that measured in the upstream plane, which is ascribed to the contraction of stream tube caused by propeller.

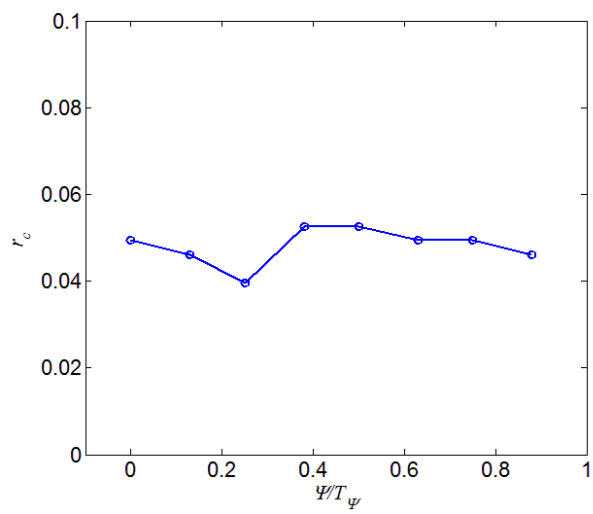

Figure 4.29: Dependence of the vortex core radius on blade phase angle. (downstream, J=0.58, r_{imp}=0.74, $\Gamma_{C,\,imp}$=-0.275)

When the blade wake vortices coincides with the impinging vortex position (Ψ=0.25T_Ψ), the vortex radius achieves the lowest value. Because at this moment, the impinging vortex is broken into two smaller fractions, and the result shown in Figure 4.29 only considers the radius of one of them. In the following phase angles, as the next blade gets closer to the vortex filament, the impinging vortex core radius decreases slightly.

As observed in Figure 4.22, regardless of the phase angles, vorticity of the vortex core is always larger than that measured in the flow field upstream the propeller. It is a result of the contraction of stream tube. As described by Eq. (2.19), for two cross sections of the vortex tube at these two measurement planes, we have

$$\int_V \nabla \omega_x dV = \int_{S_1} \omega_{x1} n_{x1} dS - \int_{S_2} \omega_{x2} n_{x2} dS = 0 \tag{4.10}$$

where ω_{x1}, n_{x1}, S_1 and ω_{x2}, n_{x1}, S_2 represent the vorticity, face normal vector and cross-sectional area of vortex tube for the cross sections upstream and downstream the propeller disk, respectively. As shown in Figure 4.29, the core radius of the impinging

vortex measured in the plane downstream the propeller is smaller. Thus, S_2 is smaller than S_1. Then we have the vorticity in the downstream plane is larger than that in the upstream plane.

Figure 4.30 shows the dependence of the maximum mean tangential velocity in the circumferential direction ($V_{t,v,m}$) on the propeller blade phase angle. Similarly, at Ψ=0.25T$_\Psi$, $V_{t,v,m}$ achieves the lowest value. After that, with the phase angle increasing, it gradually increases back to the value observed before Ψ=0.25T$_\Psi$.

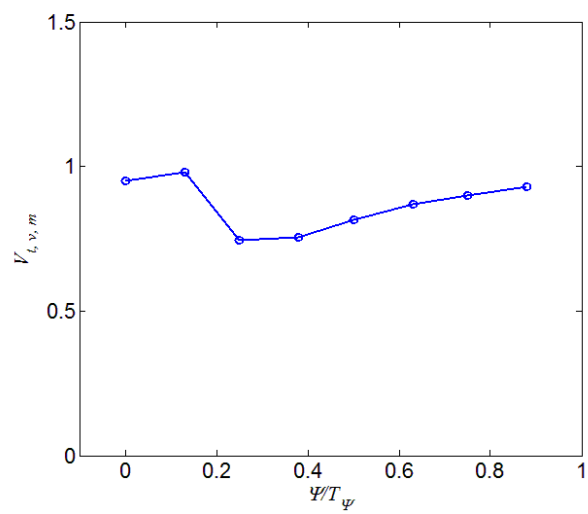

Figure 4.30: Dependence of the maximum tangential velocity on the blade phase angle. (downstream, J=0.58, r_{imp}=0.74, $\Gamma_{C,\,imp}$=-0.275)

Given the variation of vortex core radius, magnitude of the vortex core circulation at each phase angle can be obtained by Eq. (4.1), which is presented in Figure 4.31. A sharp decrease occurs after Ψ=0.13T$_\Psi$, leading to the lowest magnitude of circulation at Ψ=0.25T$_\Psi$. After that, the core circulation increases back to a nearly constant value which is slightly lower than that measured in the plane upstream the propeller. It indicates that when the impinging vortex filament develops through the gap between two blades, its core circulation is not significantly influenced by the propeller. However, when the blade wake coincides with the vortex, a significant decrease of core circulation can be observed, which is a result of the decrease of vortex core radius and maximum tangential velocity, as shown in Figure 4.29 and Figure 4.30.

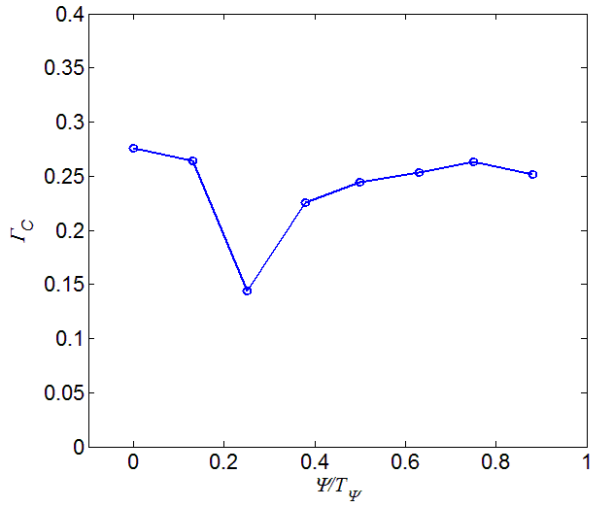

Figure 4.31: Dependence of the vortex core circulation on the blade phase angle. (downstream, J=0.58, r_{imp}=0.74, $\Gamma_{C,\,imp}$=-0.275)

Notice that the opposite trends of the variation of core radius and swirl velocity after $\Psi=0.25T_\Psi$ is ascribed to the conservation of core circulation. According to Stokes' theorem given in Eq. (2.9), expressing the core circulation by the maximum tangential velocity $V_{t,v,m}$, we have

$$\Gamma_C = \oint_C v_{t,v} dl = 2\pi r_c \cdot V_{t,v,m} \tag{4.11}$$

where $v_{t,v}$ is the local velocity at each elemental line along the integral path. As shown in Figure 4.31, the core circulation magnitude keeps nearly constant after $\Psi=0.25T_\Psi$. So with the blade phase angle increasing, the vortex core radius and maximum tangential velocity have opposite trends of variation.

4.4.2 Effects of the rotational direction of the impinging vortex

In this section, effect of the impinging vortex rotational direction is studied (Cases C1 and E2 in Table 3.2). Same as the definition stated in Section 4.1 , the symbols of vortex core circulation and vorticity is marked negative when it counter-rotates with the propeller, and marked positive for the co-rotating case.

4.4.2.1 Variation of vortex profile

Comparison of the vorticity field and radial profile of the tangential velocity in the flow field upstream the propeller are presented in Figure 4.32 andFigure 4.33. When co-rotating with the propeller, the vortex has larger tangential velocity and a slightly

smaller core radius. Except for that, the rotational direction does not have any other effect on the vortex profile observed in the plane upstream the propeller disk.

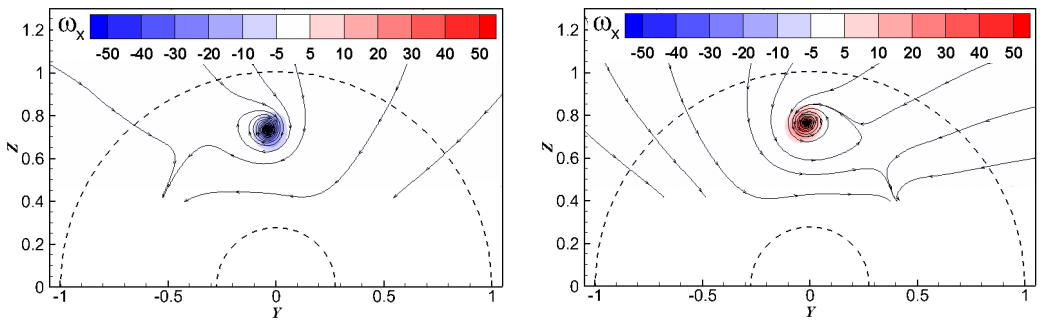

a) $\Gamma_{C,\,imp}$=-0.275 b) $\Gamma_{C,\,imp}$=0.275

Figure 4.32: Comparison of vorticity field for impinging vortex with different rotational directions. (upstream, J=0.58, r_{imp}=0.74)

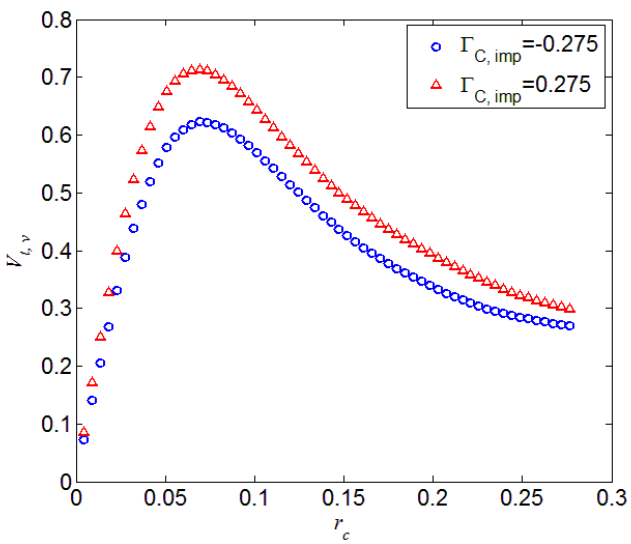

Figure 4.33: Comparison of radial profile of the tangential velocity for impinging vortexes with different rotational directions. (upstream, J=0.58, r_{imp}=0.74)

Dependence of the vorticity field on vortex rotational direction in the measurement plane downstream the propeller is shown in Figure 4.34. Only the phase angles at which the blade wake vortices are close to the impinging vortex core position (Ψ=0.13T_Ψ, 0.25T_Ψ and 0.38T_Ψ) are presented. As illustrated in Section 4.4.1 , for the counter-rotating case, unstable interaction occurs between the impinging vortex and the blade wake vortices. Deformation of both the impinging vortex and the blade wake vortices is observed in the figures in the right side of Figure 4.34(a). And even if

they get very close to each other, there is always a low vorticity region forming a "gap" between these opposite-signed vortices.

For the case that the impinging vortex has a positive symbol, as the blade wake vortices approaches, it start to merge with the impinging vortex. When the blade wake vortices get close enough to the impinging vortex core, these two vortices merge into a single pattern with higher vorticity (as shown in Figure 4.34(b)), which is a result of the interaction between a pair of co-rotating vortices[33][36]. At phase angles $\Psi=0.13T_{\Psi}$ and $0.38T_{\Psi}$, since the strength of the blade wake vortices is much lower than that of the impinging vortex, a smaller part of the wake vortices is torn and consequently wrapped around the impinging vortex[37]. While, the profile of the impinging vortex is virtually unaffected.

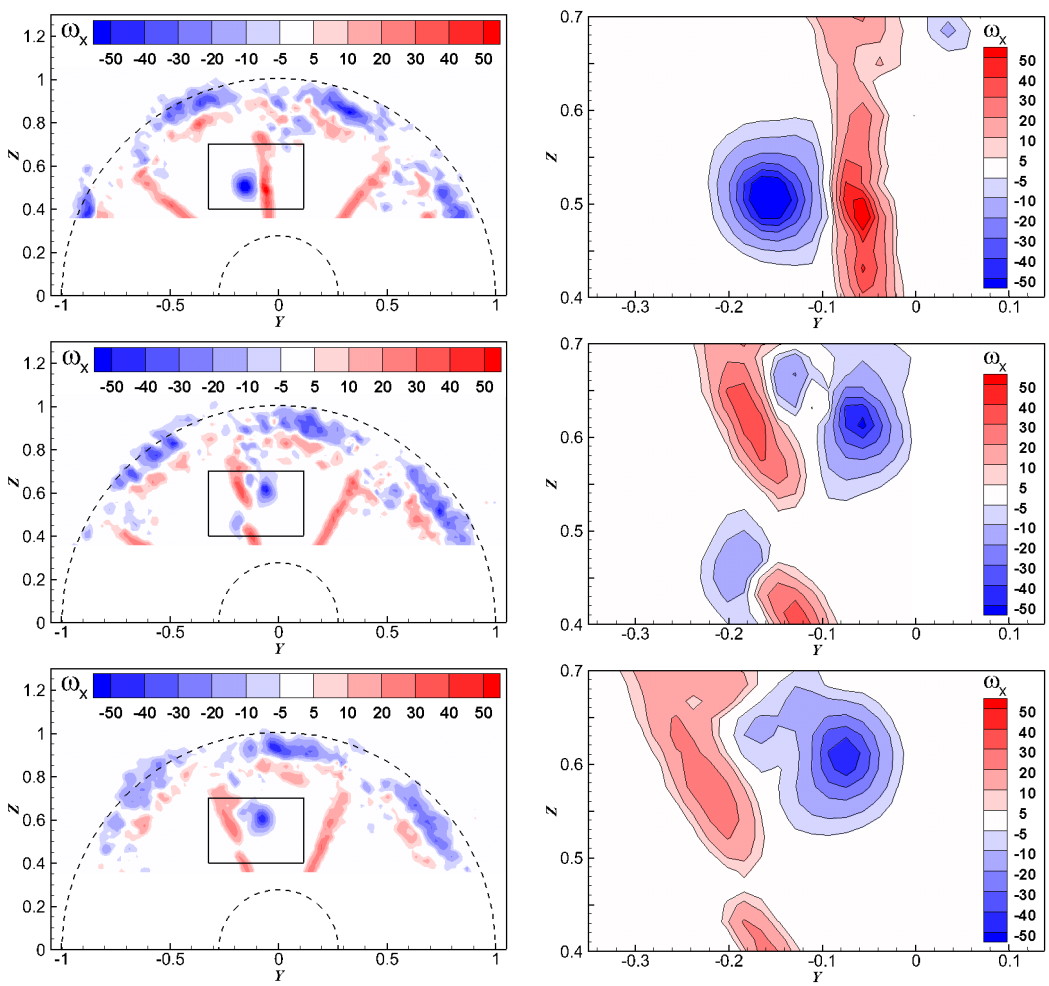

(a) $\Gamma_{C,\,imp}$=-0.275 (top: $\Psi=0.13T_{\Psi}$, middle: $\Psi=0.25T_{\Psi}$, bottom: $\Psi=0.38T_{\Psi}$)

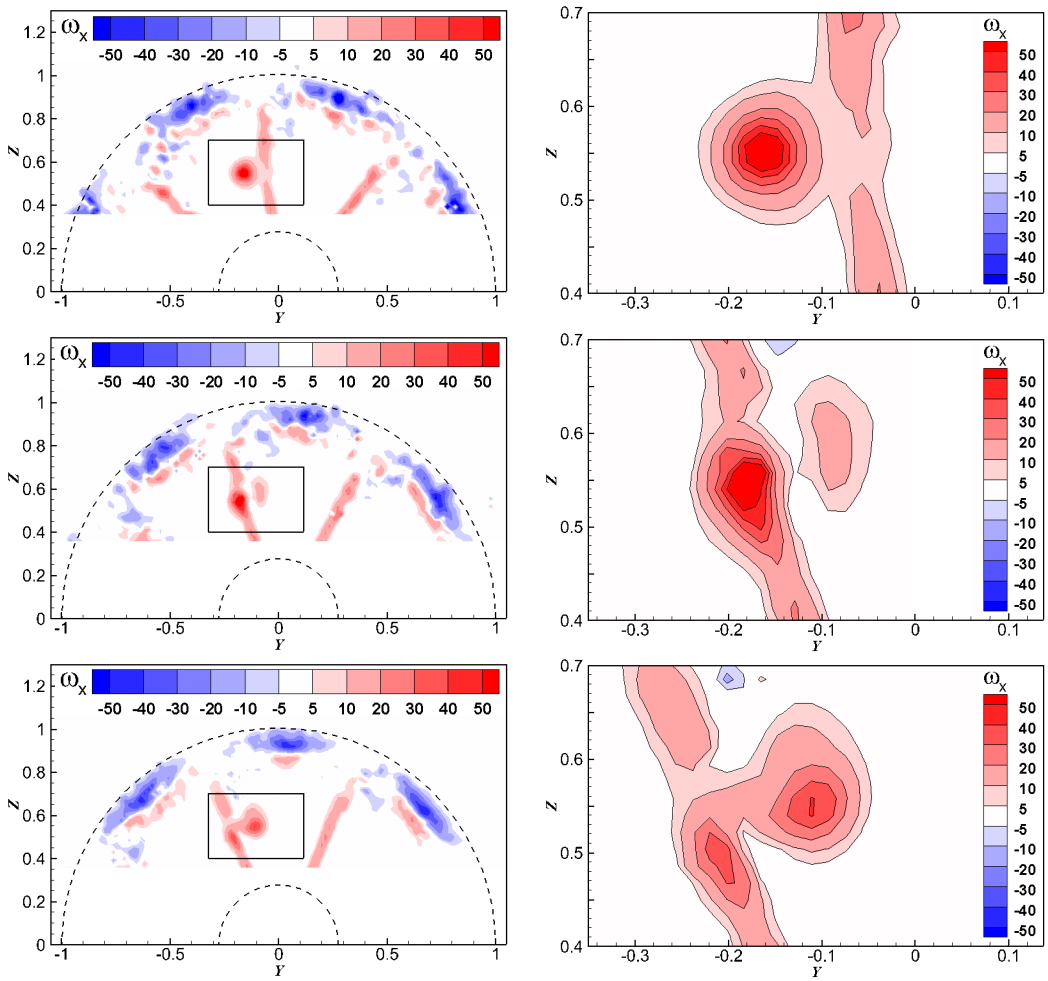

(b) $\Gamma_{C,\,imp}$=0.275 (top: Ψ=0.13T$_\Psi$, middle: Ψ=0.25T$_\Psi$, bottom: Ψ=0.38T$_\Psi$)

Figure 4.34: Dependence of vorticity field on vortex rotational direction. For each case, three phase angles at which blade positions are closest to the impinging vortex column are selected and shown. For each phase angle, the figure on the right hand side gives the details of the area marked by the rectangular frame in the figure on the left hand side, highlighting flow field near the impinging vortex. (upstream, J=0.58, r_{imp}=0.74)

4.4.2.2 Variation of vortex center position

The statistical comparison of instantaneous vortex center positions is shown in Table 4.4. The opposite vortex rotational directions do not have any significant impact on the displacement of the mean vortex between two measurement planes. However, for the distribution of instantaneous vortex center positions, the counter-rotating case has larger standard deviations, in both the r- and θ-coordinate. It indicates that in the flow field downstream the propeller, wandering of the vortex center counter-rotating case is more significant for the co-rotating case.

Table 4.4: Effect of vortex rotational direction on vortex core center positions (J=0.58, r_{imp}=0.74)

$\Gamma_{C,\,imp}$		-0.275	0.275
Displacement of mean vortex center		0.216	0.219
Standard deviation of instantaneous vortex center positions	**r-coordinate**	0.0429	0.0091
	θ-coordinate	0.0797	0.0429

Dependence of the vortex position on blade phase angle is given in Figure 4.35. The circles indicate the uncertainty of the instantaneous positions of the vortex, radius of that equals to the mean distance between all the instantaneous positions and the mean position at the corresponding phase angle. When the impinging vortex counter-rotates with the propeller, between each two neighbored phase angles, the vortex center moves a relatively large distance. However, for the co-rotating case, the distribution of the vortex center is more concentrated. It just moves very slightly as the phase angle varies, and mainly in the circumferential direction. And the commonly observed overlap between the uncertainty circles suggests that for the co-rotating case, position of vortex center is not highly dependent on the blade phase angle.

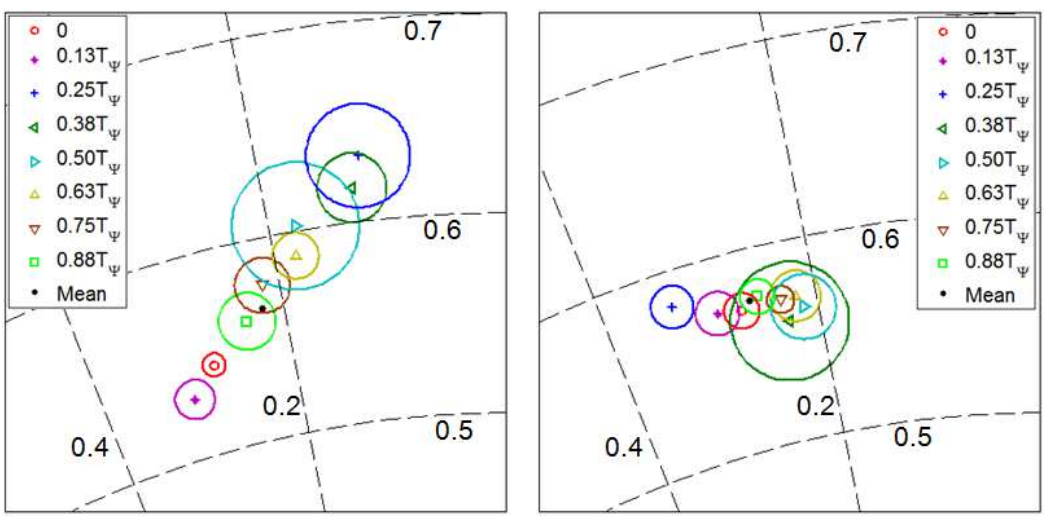

(a) $\Gamma_{C,\,imp}$=-0.275 *(b)* $\Gamma_{C,\,imp}$=0.275

Figure 4.35: Dependence of the positions of vortex on the blade phase angles. The center of the circle represents the mean position of the vortex at each phase angle; the radius of the circles represents the mean distance between the instantaneous positions and the mean position of the vortex center. (downstream, J=0.58, r_{imp}=0.74)

It is the different effects of interaction between the co- and counter-rotating vortices pair that account for the different distribution of vortex center observed in Figure 4.35.

For the counter-rotating case, as illustrated in Section 4.4.1.2 , significant wandering of vortex center is caused by the interaction between the opposite-sign vortices pair. While, as shown in Figure 4.34(b), when the impinging vortex co-rotates with the propeller, it has a trend to merge with the blade wake vortices. Evenly, once they get close enough to each other, merger can be observed in the measurement plane. It keeps the vortex center varying in a relatively small region. Due to the fact that neither of the induced tangential velocity and contraction of the stream tube is dependent on the vortex rotational direction, the results shown in Figure 4.35 support the conclusion that the vortices interaction is the prime factor that influence the dispersion of the vortex center distribution in the flow field downstream the propeller.

Note that the interaction between a pair of co-rotating vortices will develop as the vortices age downstream[38][39]. In the flow field further downstream, it can be inferred that merger between the impinging vortex and the wake vortices can be observed in more blade angle moments other than $\Psi=0.25T_{\Psi}$.

4.4.2.3 Variations of vortex core radius and circulation

A comparison of the impinging vortex characteristics in the flow field upstream the propeller is presented in Table 4.5. The vortex core radius does not vary significantly with the change of the sense of rotation. However, when the vortex counter-rotates with the propeller, the magnitude of the maximum tangential velocity and core circulation are larger than that for the other case.

Table 4.5: Comparison of impinging vortex core radius, maximum tangential velocity and core circulation for different vortex rotational directions. (upstream, J=0.58, r_{imp}=0.74)

$\Gamma_{C,\,imp}$	**-0.275**	**0.275**
r_c	0.069	0.065
$V_{t,\,v,\,m}$	-0.64	0.73
Γ_C	-0.277	0.297

In the flow field downstream the propeller, dependence of core radius on the blade phase angles is shown in Figure 4.36. For both of these two cases, the vortex core radius achieves the lowest value at phase angle $\Psi=0.25T_{\Psi}$. However, for each of these cases, it is caused by different mechanisms. As shown in Figure 4.34, when $\Psi=0.25T_{\Psi}$, for the co-rotating case, the impinging vortex merges with the blade wake vortices. It generates a new vortex with smaller core radius but larger core vorticity. For the counter-rotating case, the impinging vortex is broken by the blade wake vortices into two patterns, each of them has smaller radius and lower intensity.

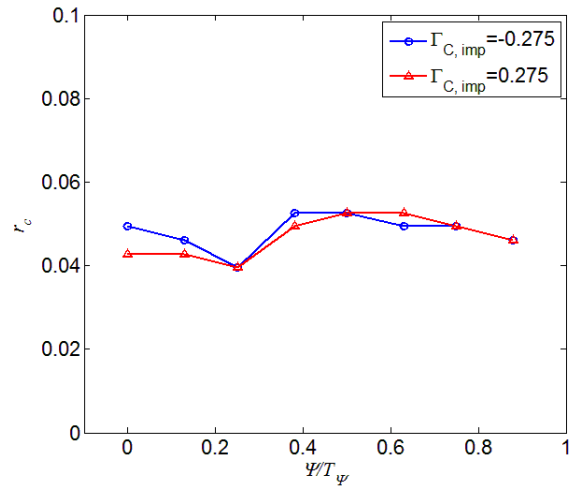

Figure 4.36: Effect of the vortex rotational direction on the vortex core radius. (downstream, J=0.58, r_{imp}=0.74)

Comparison of the magnitude of the maximum tangential velocity is shown in Figure 4.37. At most of the blade phase angles, the curves for these two cases have good agreement. However, at the moment $\Psi=0.25T_\Psi$, thus, when the impinging vortex and blade wake vortices has the strongest interaction effect, $V_{t,v,m}$ for the co-rotating case is much larger than that for the other case. Evenly, it is larger than the values for any other phase angle. Such a large value of maximum tangential velocity observed at $\Psi=0.25T_\Psi$ is in consistence with the vortices merger observed in Figure 4.34(b). It forms a new vortex pattern with larger magnitude of vorticity.

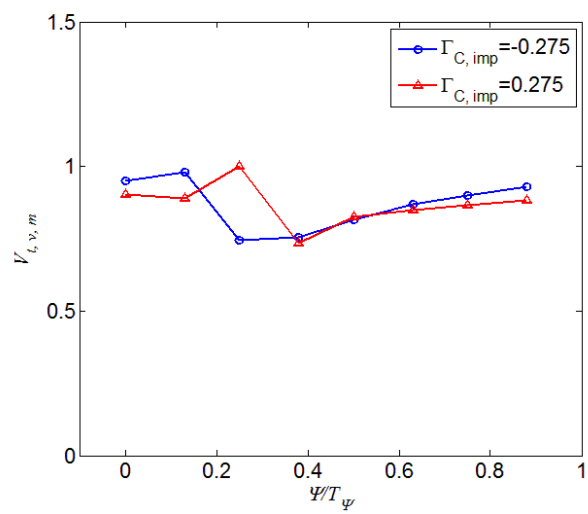

Figure 4.37: Effect of vortex rotational direction on the maximum tangential velocity. (downstream, J=0.58, r_{imp}=0.74)

The dependence of core circulation on the blade phase angle is shown in Figure 4.38. It is consistent with the vortex profiles as presented in Figure 4.34. When $\Psi=0.25T_{\Psi}$, the vortex core radius for both two cases achieve a low value. For the case $\Gamma_{C,\,imp}=0.275$, the maximum tangential velocity is much higher than that for the other case. As a result, at the phase angle $\Psi=0.25T_{\Psi}$, a larger magnitude of core circulation is observed for the case $\Gamma_{C,\,imp}=0.275$.

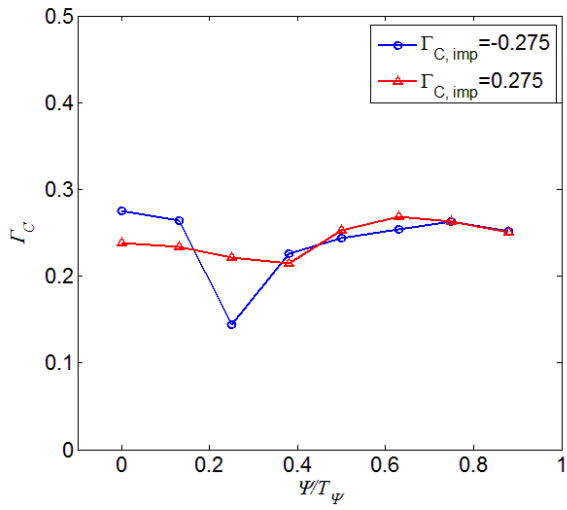

Figure 4.38: Effect of vortex rotational direction on the vortex core circulation. (downstream, J=0.58, r_{imp}=0.74)

4.4.3 Effects of propeller advance ratio

In this section, three advance ratio conditions, 0.58, 0.78 and 1.10 (Cases C1, C2 and C3 in Table 3.2) are selected to investigate the effect of advance ratio on the development of vortex filament through the propeller disk.

4.4.3.1 Variations of vortex profile

For each advance ratio, vorticity field and radial profile of the tangential velocity in the measurement plane upstream the propeller are shown in Figure 4.39Figure 4.40. The position of vortex center in the plane upstream the propeller is virtually independent from the advance ratio. However, with advance ratio increasing, the vortex core radius slightly increases, and magnitude of the maximum tangential velocity decreases (Figure 4.40).

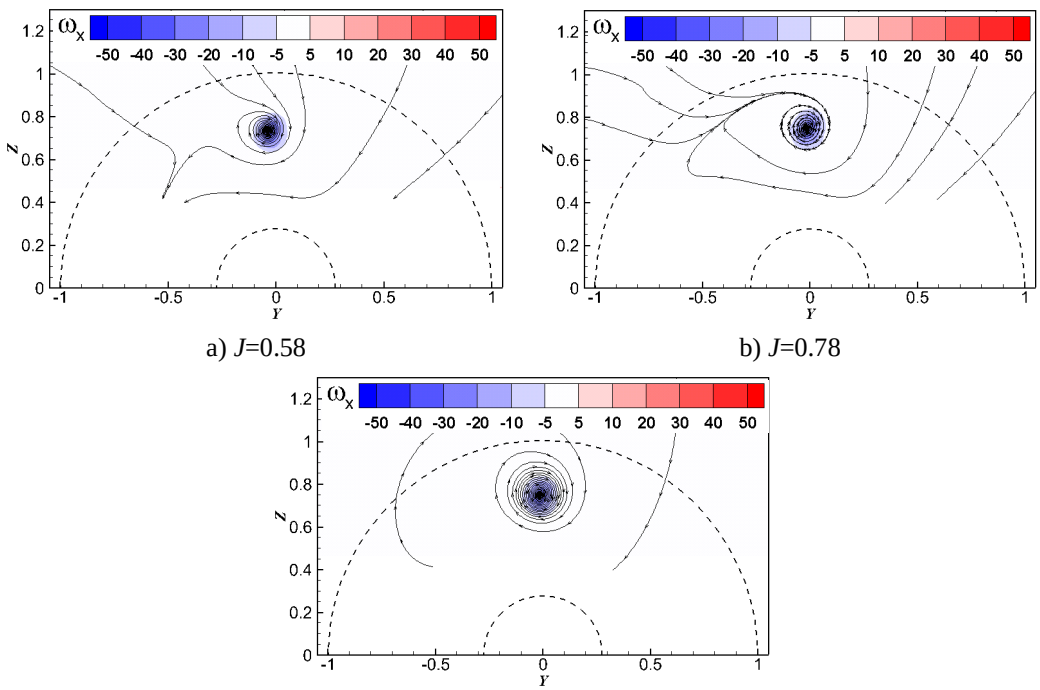

a) J=0.58 b) J=0.78

c) J=1.10

Figure 4.39: Comparison of vorticity fields of different advance ratios. (upstream, $\Gamma_{C,\,imp}$=-0.275, r_{imp}=0.74)

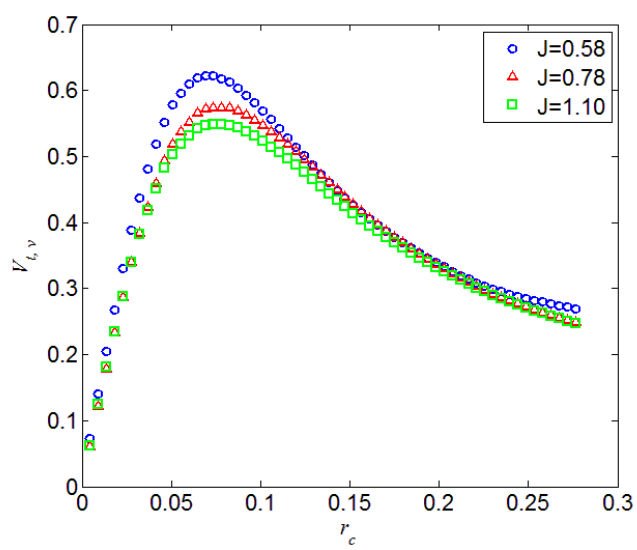

Figure 4.40: Comparison of radial profile of the tangential velocity for different advance ratio conditions. (upstream, $\Gamma_{C,\,imp}$=-0.275, r_{imp}=0.74)

As illustrated in Figure 4.22, in the flow field downstream the propeller, the vortex profile is dependent on the blade phase angle. When the blade wake vortices rotate to

the position that coincides with the impinging vortex core, the most severe interaction effect can be observed. In Figure 4.41, the vorticity field in the measurement plane downstream the propeller for different advance ratios are shown. For each advance ratio condition, contour figures for two phase angles are selected to present, including the one when the blade wake vortices coincides with the vortex column and the one follows.

In lower advance ratio condition, the propeller has higher rotational speed and heavier load, which cause stronger blade wake vortices. When J=0.58, as shown in Figure 4.41(a), once the position of the blade wake vortices coincides with the impinging vortex, they break each other into smaller vortices fractions. As the advance ratio increases, propeller rotational speed decreases, resulting in weaker blade wake vortices. As observed in Figure 4.41(c), when J=1.10, the blade wake vortices are not strong enough to break the impinging vortex apart. The impinging vortex is just stretched into a longer shape, but still maintains as a whole vortex body.

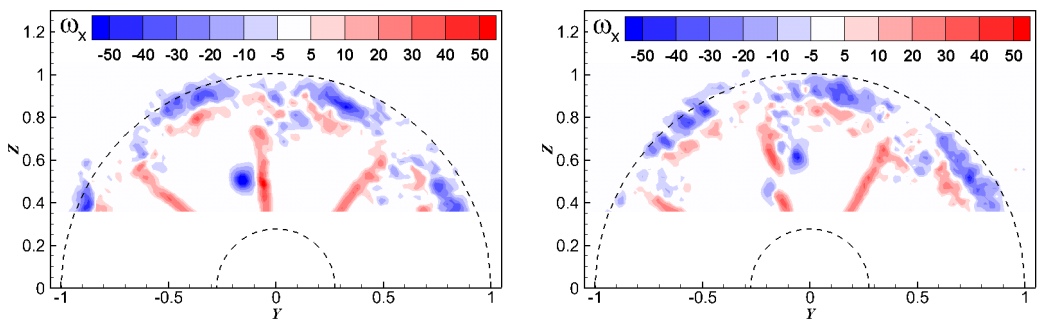

(b) J=0.58 (left: Ψ=0.25T_Ψ, right: Ψ=0.38T_Ψ)

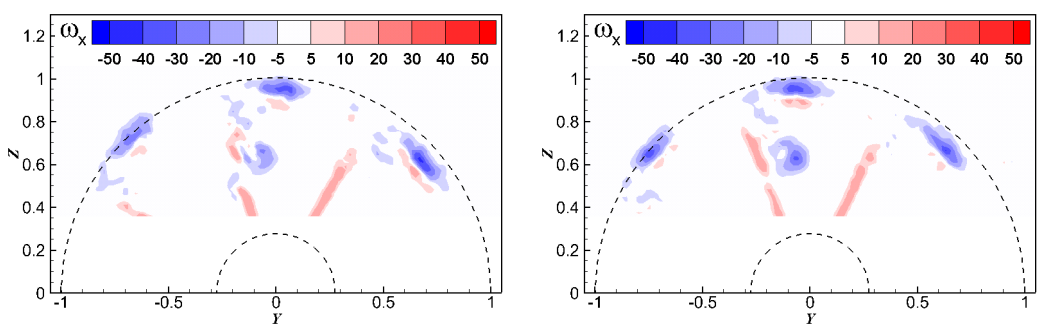

(b) J=0.78 (left: Ψ=0.25T_Ψ, right: Ψ=0.38T_Ψ)

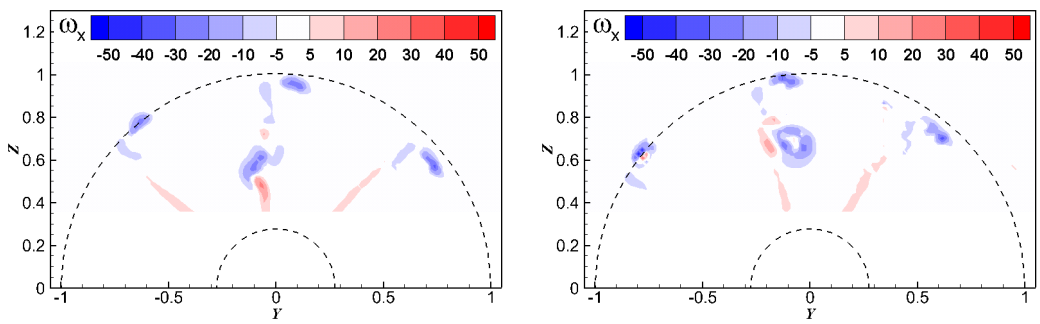

(c) J=1.10 (left: Ψ=0.25T_Ψ, right: Ψ=0.38T_Ψ)

Figure 4.41: Dependence of the vorticity field on propeller advance ratio. (downstream, $\Gamma_{C,\,imp}$=-0.275, r_{imp}=0.74)

When J=1.10, the propeller blade vortices coincide with the impinging vortex column at phase angle Ψ=0.13T_Ψ, which is one phase angle step advanced comparing to that for J=0.58 and 0.78. It is a result of the smaller displacement of the mean vortex center position between these two measurement planes. Details about that will be discussed in the next section.

4.4.3.2 Variations of vortex center positions

All the four factors that have impacts on the vortex center position in the flow field downstream the propeller, induced tangential velocity, contraction of stream tube, interaction between vortices and velocities induced by the blade wake vortices, are dependent on advance ratio. As a result, variation of advance ratio has significant effects on the position of the impinging vortex center.

Figure 4.42 andFigure 4.43(a) present the displacement of the mean vortex center positions between two measurement planes for different advance ratios. In the plane upstream the propeller, the mean vortex center position is virtually independent from the advance ratio. While, in the plane downstream the propeller, as advance ratio increasing, the mean vortex center position gets closer to that in the upstream plane. Thus, the displacement of the mean vortex center position becomes smaller as the advance ratio increases.

As discussed in Section 4.4.1.2 , displacement of the mean vortex center position between two measurement planes are dependent on the induced tangential velocity and contraction of stream tube. As advance ratio increases, the rotational speed of each blade and load of the propeller decrease, leading to lower induced tangential velocity and less contraction of stream tube. Hence, as advance ratio increases, the displacement of mean vortex center position decreases in both r- and θ-coordinate.

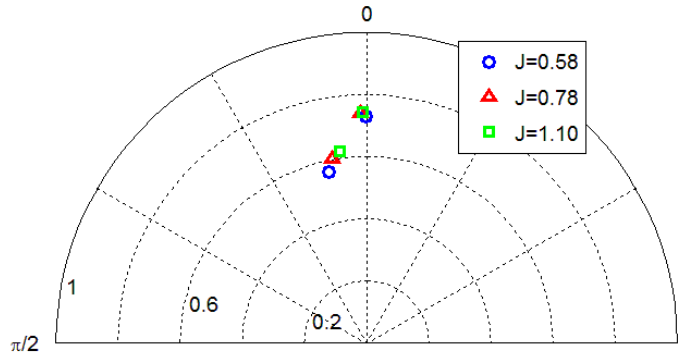

Figure 4.42: Displacement of mean vortex center position between the upstream and downstream measurement planes for different advance ratios. (J=0.58, $\Gamma_{C,\ imp}$=-0.275)

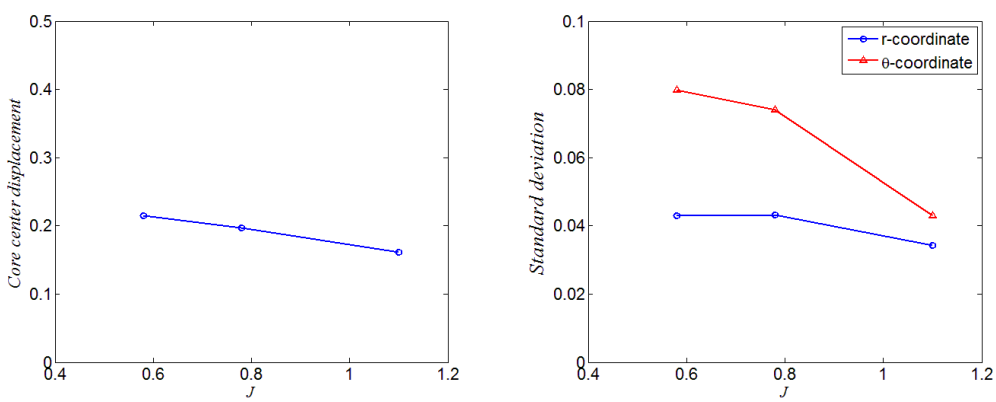

(a) Displacement of mean vortex center position between two PIV measurement planes

(b) Standard deviation of instantaneous vortex center positions

Figure 4.43: Statistical analysis of vortex center positions for different advance ratios. (downstream, J =0.58, $\Gamma_{C,\ imp}$=-0.275)

Statistical analysis of the vortex center positions is presented in Figure 4.43. As advance ratio increases, standard deviation of the instantaneous center positions in the plane downstream the propeller (Figure 4.43(b)) decreases, in both r- and θ-coordinate. Evidently, it indicates that when propeller advance ratio increases, distribution of the instantaneous vortex center positions in the flow field downstream the propeller becomes more concentrated.

As shown in Figure 4.41, strength of the blade wake vortices decreases as the advance ratio increases. The effect of the interaction between the blade wake vortices and the

impinging vortex becomes less significant. And also, according to Biot-Savart law, the magnitude of the velocities induced by the blade wake vortices becomes lower. As a result, with advance ratio increasing, the distribution of instantaneous vortex center becomes less dispersed.

4.4.3.3 Variations of vortex characteristics

Variations of the impinging vortex core radius, maximum tangential velocity and core circulation with advance ratio in the flow field upstream the propeller are given in Figure 4.44. As advance ratio increases, contraction of stream tube becomes weaker. The vortex core radius increases, the maximum tangential velocity decreases, and the core circulation is basically independent from the advance radio.

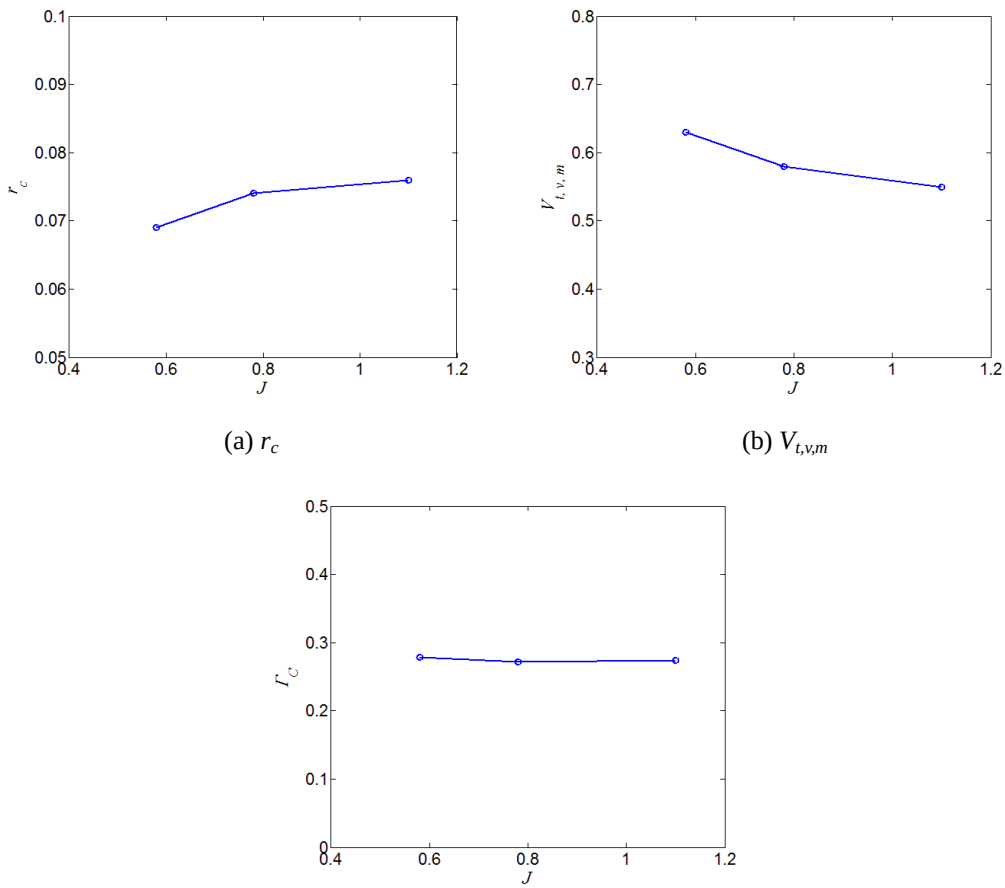

(a) r_c (b) $V_{t,v,m}$

(c) Γ_C

Figure 4.44: Dependence of impinging vortex characteristics on propeller advance ratio. (upstream, $\Gamma_{C,\,imp}$=-0.275, r_{imp}=0.74)

In the measurement plane downstream the propeller, as shown in Figure 4.45 andFigure 4.46, when the impinging vortex aging through the gap between two blades

(Ψ=0.38T$_\Psi$-0.88T$_\Psi$), lower advance ratio results in smaller vortex core radius and larger magnitude of the maximum tangential velocity. For each advance ratio, both r_c and $V_{t,v,m}$ achieves the lowest value at the phase angle when the impinging vortex and blade wake vortices coincide with each other. After that, r_c increases to a high point immediately, and then decreases gradually. While $V_{t,v,m}$ just monotonically increases from the lowest value. Furthermore, as shown in Figure 4.47, the variation of r_c and $V_{t,v,m}$ between the planes upstream and downstream the propeller disk, Δr_c and $\Delta V_{t,v,m}$, decrease with the advance ratio increasing.

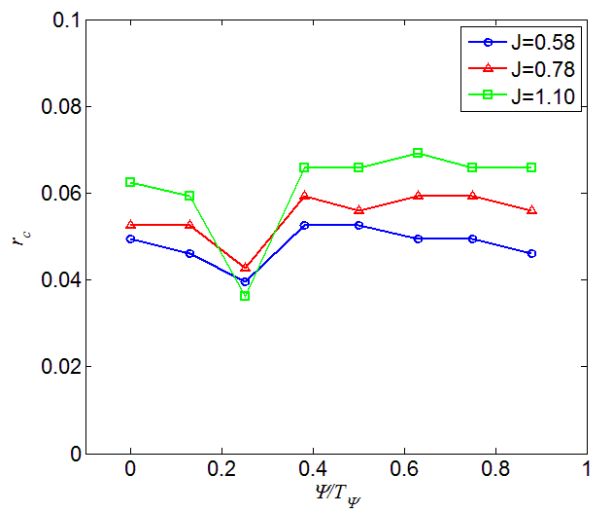

Figure 4.45: Effect of advance ratio on the vortex core radius. (downstream, $\Gamma_{C,\,imp}$=-0.275, r_{imp}=0.74)

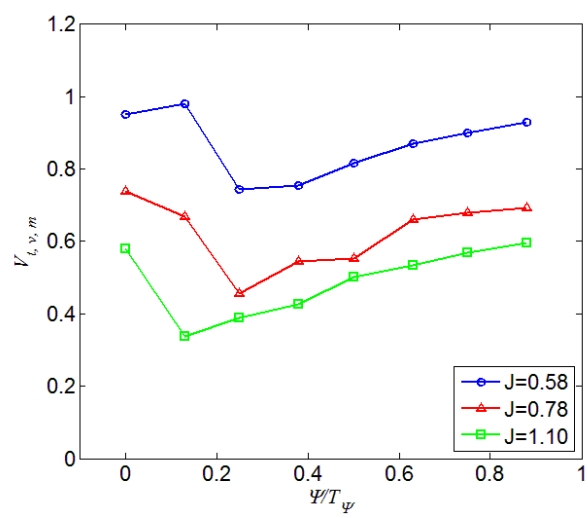

Figure 4.46: Effect of advance ratio on the maximum tangential velocity. (downstream, $\Gamma_{C,\,imp}$=-0.275, r_{imp}=0.74)

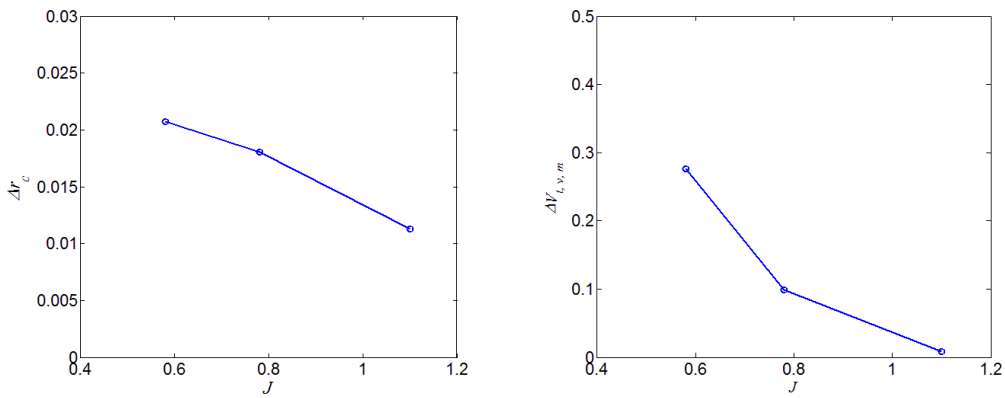

(a) r_c (b) $V_{t,\,v,\,m}$

Figure 4.47: Variation of vortex core radius and maximum tangential velocity between the measurement planes upstream and downstream the propeller.

Dependence of the vortex core circulation on advance ratio in the plane downstream the propeller is presented in Figure 4.48. For each of these advance ratio conditions, due to the interaction between the impinging vortex and blade wake vortices, dramatic vortex core circulation variation can be observed between Ψ=0.13T_Ψ-0.38T_Ψ. For other phase angles, although not totally constant, the vortex core circulation magnitude just has slight fluctuation. And also, the variation of advance ratio does not have any significant impact on the magnitude of core circulation.

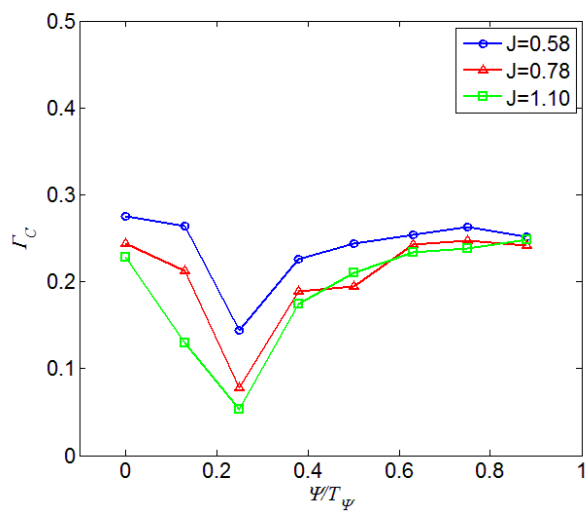

Figure 4.48: Effect of advance ratio on the vortex core circulation. (downstream, $\Gamma_{C,\,imp}$=-0.275, r_{imp}=0.74)

Note that in Figure 4.41Figure 4.46, both the core vorticity and maximum tangential velocity of the impinging vortex increase with propeller advance ratio decreasing. It is a result of the increase of propeller contraction strength. With lower advance ratio, propeller generates stronger contraction of the stream tube, causing smaller vortex core radius, as shown in Figure 4.45. Since the vortex core circulation basically keeps constant, as the integral area in Eq. (4.1) and integral length in Eq. (4.11) decrease, both the magnitudes of vorticity and maximum tangential velocity increase.

4.4.4 Effects of radial impingement position

In this section, variations of vortex characteristics under three impinging radial positions, r_{imp}=0.74, 0.83 and 0.92 (Cases C3, D1 and D2 in Table 3.2) are investigated.

4.4.4.1 Variation of vortex profile

For each radial impingement position, the vorticity field and radial profile of tangential in the upstream measurement planes are presented in Figure 4.49 andFigure 4.50. As the impinging position moves outwards, except for the displacement of center position, there is not any other evident difference observed.

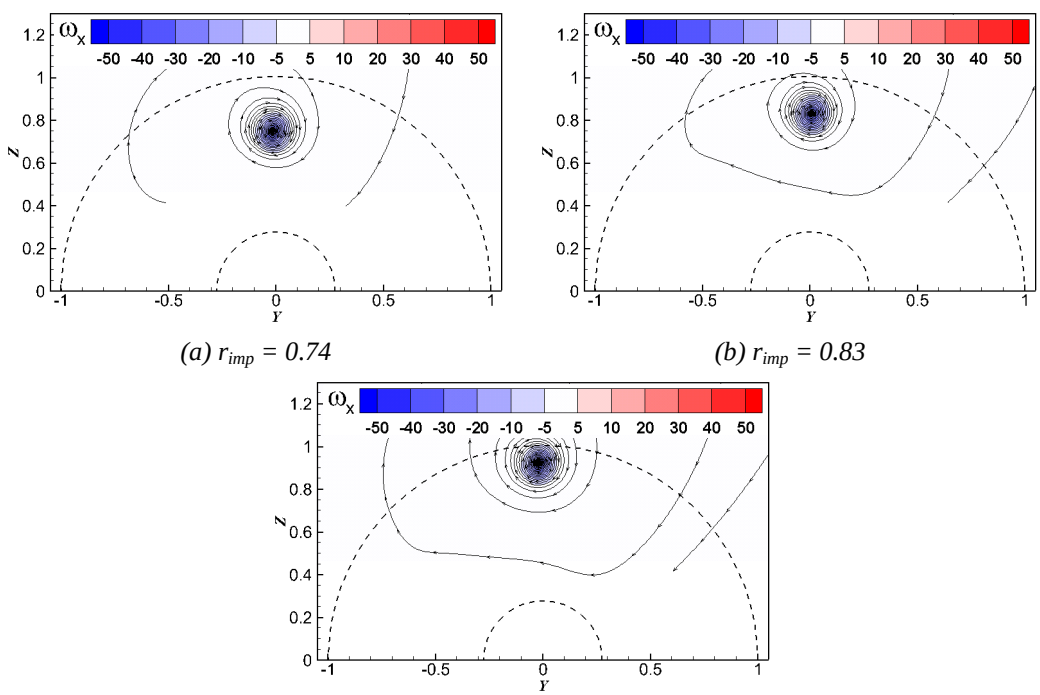

(a) r_{imp} = 0.74

(b) r_{imp} = 0.83

(c)r_{imp} = 0.92

Figure 4.49: Vorticity distribution for different impinging radial positions. (upstream, J=1.10, $\Gamma_{C,\,imp}$=-0.275)

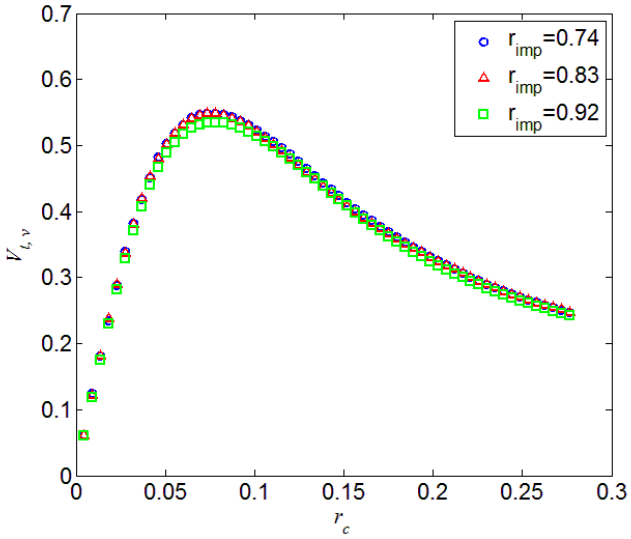

Figure 4.50: The radial profile of the tangential velocity for different radial impinging positions. (upstream, J=1.10, $\Gamma_{C,\,imp}$=-0.275)

Figure 4.51 shows the vorticity fields in the measurement plane downstream the propeller. Phase angle at which the impinging vortex coincides with the blade wake vortices (Ψ=0.13T_Ψ) and the following one (Ψ=0.25T_Ψ) are chosen to present. When Ψ=0.13T_Ψ, since the blade wake vortices are very weak, the impinging vortex is just stretched into irregular shapes, instead of being broken into smaller fractions. Note that for the cases r_{imp} = 0.83 and 0.92, since the impinging vortex are very close to the blade tip, although its core position can still be well recognized, merger between the impinging vortex and blade tip vortices can be observed.

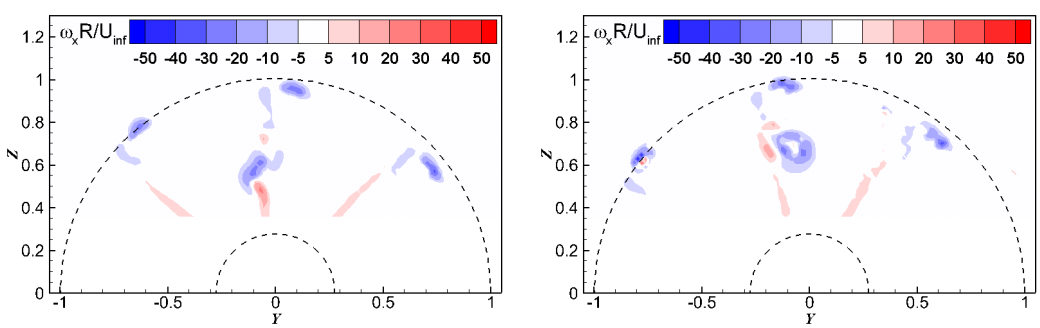

(a) r_{imp} = 0.74 (left: Ψ=0.13T_Ψ, right: Ψ=0.25T_Ψ)

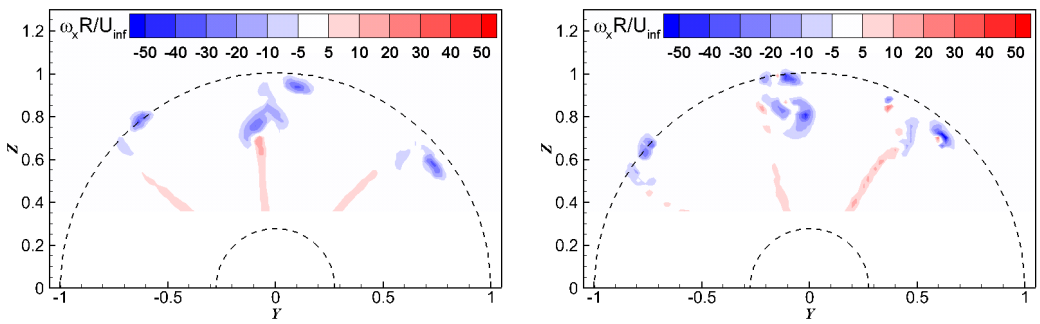

(b) r_{imp} = 0.83 (left: Ψ=0.13T$_{\Psi}$, right: Ψ=0.25T$_{\Psi}$)

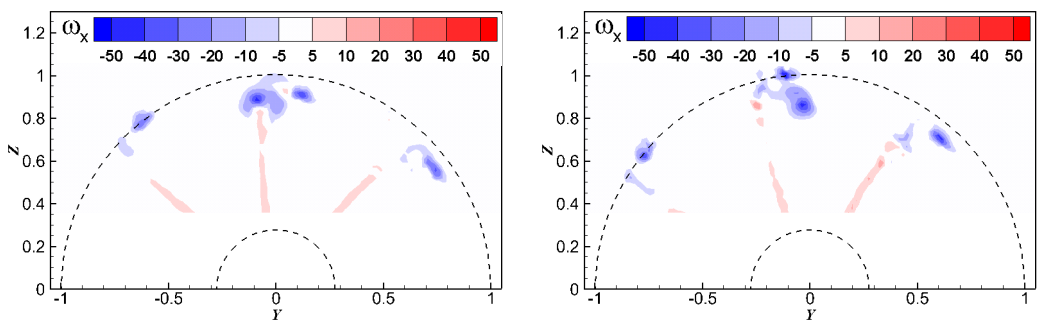

(c) r_{imp} = 0.92 (left: Ψ=0.13T$_{\Psi}$, right: Ψ=0.25T$_{\Psi}$)

Figure 4.51: Vorticity fields for different vortex impinging radial positions. For each case, phase angles when blade wake coincides with the impinging vortex column and the following one were selected. (downstream, J=1.10, $\Gamma_{C,imp}$=-0.275).

4.4.4.2 Variation of vortex center position

Displacement of mean vortex center position between the two measurement planes and standard deviation of instantaneous center positions in the plane downstream the propeller are given in Figure 4.52. As shown in Figure 4.52(a), the displacement of mean vortex center position decreases as the impinging radial position moves outwards. Similarly, as shown in Figure 4.52(b), the standard deviation of instantaneous center positions in both two coordinates decrease with the radial impingement position moving outwards.

According to Figure 4.9, the maximum circumferential load occurs at radial position r_b=0.87. Comparing the radial position r_{imp}=0.74, the other two impingement positions are closer to the maximum load position in the radial direction. And the annular ring with radius of 0.74R would be contracted more significant than that for the annular ring with radius of 0.83 and 0.92. Hence, the displacement of mean vortex center in the r-coordinate for the case r_{imp}=0.74 is much larger than that for the other two cases. As for the θ-coordinate, according to Figure 4.27, from the radial position r_b=0.70 the induced tangential velocity decreases as the radial position increases. That explains why the displacement of mean vortex center in the θ-coordinate decreases as

the impingement position moves outwards.

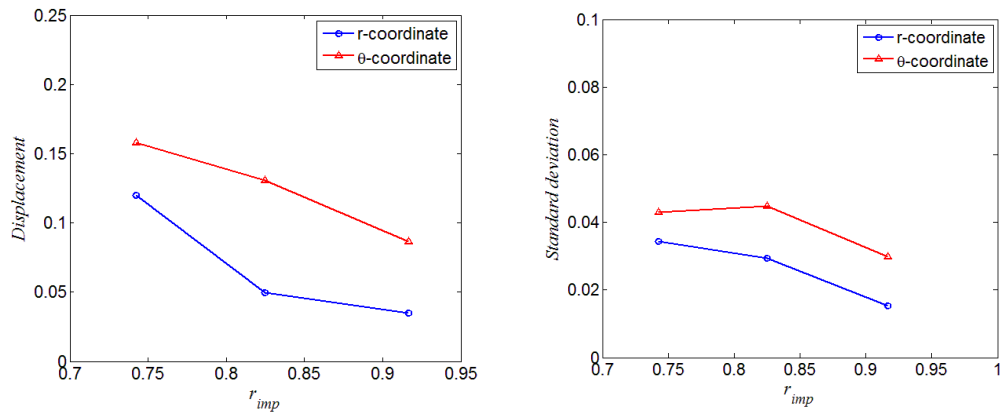

(a) Displacement of mean vortex center position

(b) Standard deviation of instantaneous vortex center positions in the plane downstream the propeller

Figure 4.52: Statistical analysis of vortex center positions for different radial impingement positions (J=1.10, $\Gamma_{C,\,imp}$=-0.275).

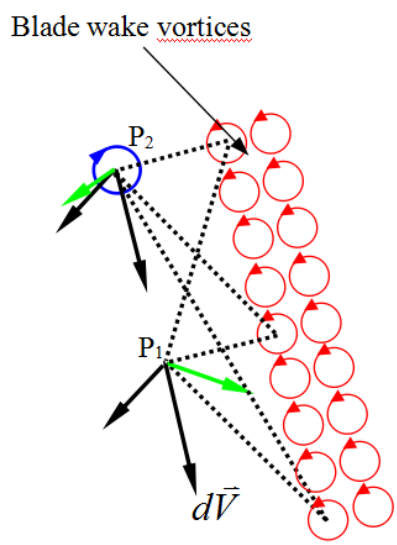

Figure 4.53: Scheme of the velocities induced by vortices at different radial positions

In the region where radial position r_b>0.5, as the impinging vortex moves outwards, according to the Biot-Savart law, sum of the radial components of velocities induced at its core decreases. As shown in Figure 4.53, at the point P_2, because of the direction and magnitude of the induced velocity marked in green, its component in the radial direction is smaller than that generated at the point P_1. It results in a smaller sum of

the radial components of the induced velocities at P_2. Hence, smaller standard deviation in the r-coordinate is observed for the cases with the impingement position locating further outwards.

4.4.4.3 Variation of vortex core characteristics

Variations of vortex core radius, maximum tangential velocity and core circulation in the measurement plane upstream the propeller are presented in Figure 4.54. In consistence with the vorticity fields and radial profiles of tangential velocity shown in Figure 4.49Figure 4.50, in the flow field upstream the propeller, none of these three parameters varies significantly.

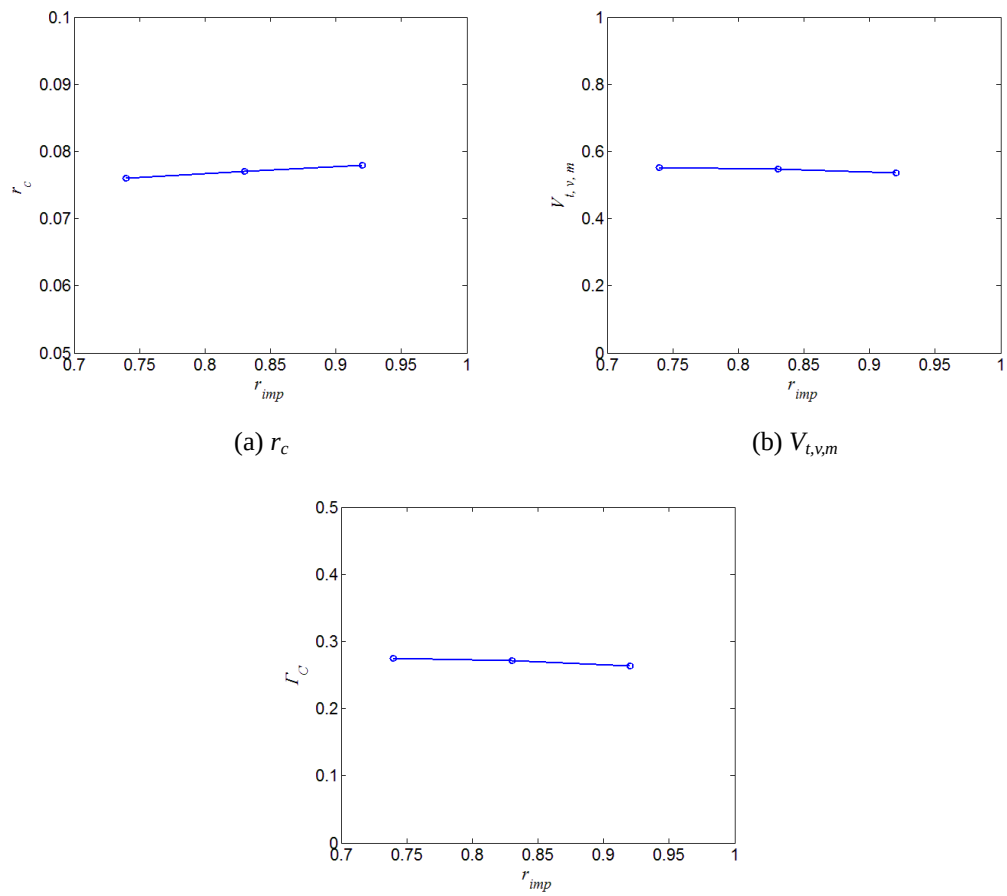

(a) r_c (b) $V_{t,v,m}$

(c) Γ_C

Figure 4.54: Dependence of r_c, $V_{t,v,m}$ and Γ_C on radial impingement position. (upstream, J=0.58, $\Gamma_{C,\,imp}$=-0.275)

In the plane downstream the propeller, variations of r_c, $V_{t,v,m}$ and Γ_C with the vortex radial impingement position are presented in Figure 4.55Figure 4.56Figure 4.57, respectively. When the vortex develops through the gap between two blades

(Ψ=0.38T_Ψ - 0.88T_Ψ), as shown in Figure 4.55, for the case r_{imp}=0.74, vortex core radius is evidently larger than that for the cases r_{imp}=0.83 and 0.92.

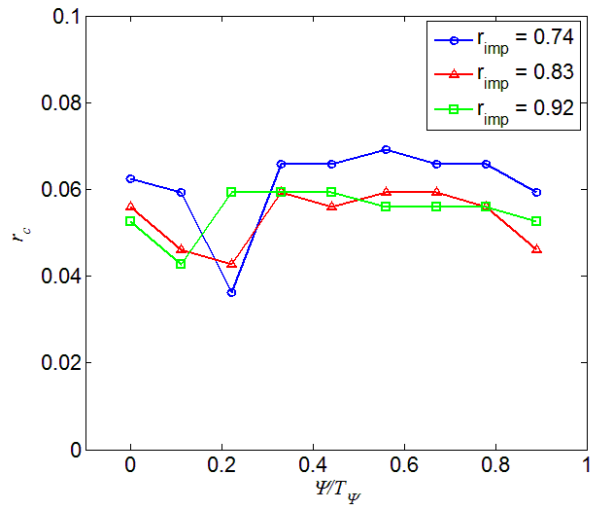

Figure 4.55: Effect of the radial impinging position on the vortex core radius. (downstream, J=0.58, $\Gamma_{C,\,imp}$=-0.275)

As discussed above, propeller largest circumferential load appears at radial position r_b=0.87. According to the momentum theory, larger propeller load means stronger contraction of the stream tube. Since r_b=0.74 is farther to the heaviest load position than the other two, for the case r_{imp}=0.74, the impinging vortex is contracted less than that for the other two cases. Thus, the vortex core radius observed in the plane downstream the propeller for the case r_{imp}=0.74 is larger. And since the radial positions r_{imp}=0.83 and 0.92 have almost the same distance to the largest load position, the vortex radius for that two cases approximately equal to each other.

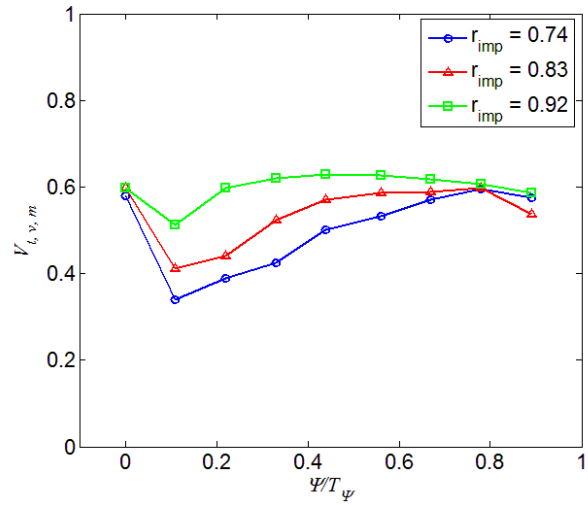

Figure 4.56: Effect of the radial impinging position on the vortex maximum tangential velocity. (downstream, J=0.58, $\Gamma_{C,\,imp}$=-0.275

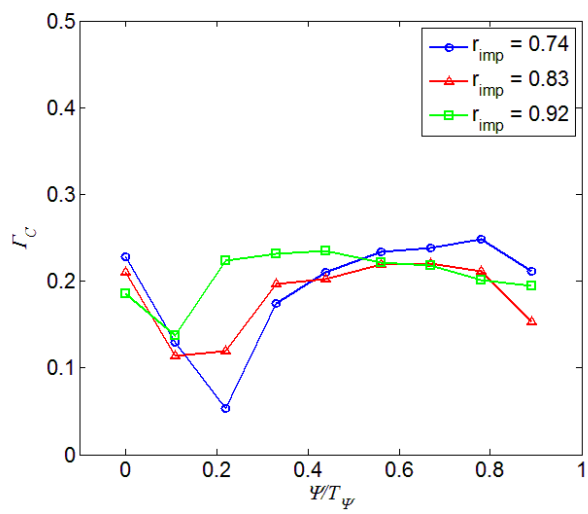

Figure 4.57: Effect of the radial impinging position on the vortex core circulation. (downstream, J=1.10, $\Gamma_{C,\,imp}$=-0.275)

5 Conclusions, Discussion and Recommendation

This chapter gives the conclusions obtained from the experimental and numerical analysis reported in Chapter 4, which provides answers for the questions stated in this project: what effects would be caused by the orthogonal interaction between the inflow vortex and propeller. Discussions on experimental results and the numerical results are presented. And it is closed with some the unsolved problems and recommendations for further research.

5.1 Variations of propeller performance

According to the numerical analysis, the variation of propeller performance caused by vortex impingement is a result of the variation of flow field. The vortex tangential velocity can increase or decrease the local tangential velocity of blade cross sections, which lead to lower or higher angle of attack, resulting in increase or decrease of the normal force and out-of-plane component of moment generated by the corresponding blade cross sections.

The impact of the impinging vortex on propeller performance is mainly decided by the rotational direction of the vortex with respect to the rotation of propeller. When co-rotating with the propeller, the impinging vortex decreases both thrust and torque coefficients. For the counter-rotating case, both of them are increased. The variation becomes more significant as the strength of the impinging vortex increases and propeller advance ratio increases, and it decreases as the radial impingement position moves outwards. However, the vortex impingement does not have any significant impact on efficiency of the propeller.

5.2 Variations of vortex behavior

Interaction between the impinging vortex and blade wake vortices is an important factor that decides the behaviors of the vortex observed in the plane downstream the propeller. The effect of that interaction is mainly decided by the relatively rotational direction between these two vortices. Unstable interaction occurs when they counter-rotates with each other. In that case, when the blade wake vortices are strong enough, the impinging vortex would be broken into fractions with smaller scales. On the other hand, for the co-rotating case, merger between two vortices occurs, forming a new pattern with higher intensity.

Characteristics of the vortex in the flow field downstream the propeller is dependent on the blade phase angle. When the vortex filament ages through the gap between two blades, magnitude of the vortex core circulation measured in the planes upstream and downstream the propeller does not vary significantly. At the moment blade wake vortices coincides with the impinging vortex, the core circulation decrease sharply for the counter-rotating case.

Due to the contraction of stream tube caused by the propeller, the impinging vortex in the stream tube is shrunk. The vortex core radius in the flow field downstream of the propeller is smaller than that observed in the flow field upstream. The decrease of vortex radius is mainly determined by the load distribution of the propeller. Heavier load causes stronger contraction of the stream tube, leading to more significant shrinking of the vortex core. At the moments when the impinging vortex is relatively far from the blade wake vortices, since the core circulation basically keeps constant, the maximum tangential velocity and vorticity of the vortex increase as the load of propeller increases, due to the decrease of the vortex core radius.

Between the measurement planes upstream and downstream the propeller, a displacement of the mean vortex center position can be observed. In r-coordinate, the mean position of the vortex center moves inwards, which is a result of the contraction of stream tube. In θ-coordinate, the vortex center moves in the same direction as the blades rotate, which is caused by the induced tangential velocity. And in the flow field downstream the propeller, the instantaneous position of the vortex center wanders with the blade phase angle. The wandering in r-coordinate is decided by the interaction between the impinging vortex and blade wake vortices, and that in θ-coordinate is relevant to the radial component of the velocities induced by the blade wake vortices in the Y-Z plane.

5.3 Discussion of modified BEM theory

Based on the comparison between the numerical and experimental results, it can be concluded that the modified BEM theory is able to simulate the propeller performance variation caused by vortex impingement. However, the thrust and torque coefficients calculated by BEM theory is higher than that measured by RSB, and the variation amplitude obtained by BEM theory is slightly smaller. There are several possible causes for these deviations observed between the numerical and experimental results:

1) It is hard to obtain accurate c_d values in computation. For each station on blade, although an accurate c_d-α_b curve can be obtained, it is not easy to express the c_d values with a mathematical function. During the iteration process to solve the equations group (3.23) and (3.24), errors on the c_d-α_b would be accumulated and lead to a relative large error for the C_Q value.

2) The application of BEM theory in this project does not consider the vortex variation in the flow fields from upstream to downstream the propeller. For example, according to the PIV measurement results given in Section 4.4 , as the impinging vortex develops downstream, its core radius decreases, and the core center position wanders. But in the computational process, all the vortex characteristics are considered constant.

3) Impinging vortex radius is in the same order of chord length of the blade in each station. In the numerical simulation, the flow field variation caused by the impinging vortex is only applied to the leading edge of each airfoil station, and the calculation is performed with the assumption that the whole airfoil is in uniform flow. However, in reality, the vortex may cause more complicated flow on both the pressure and suction sides of the blade surface.

5.4 Recommendation for future research

In this project, only two PIV measurement planes were selected along the flow direction. To have a further research on this topic, setting more measurement planes, especially in the flow field downstream of the propeller disk would be helpful to investigate the development of the vortex column. Since the interaction between vortices would develop as the vortices age downstream, characteristics of the impinging vortex at the same phase angle might be observed differently in different measurement planes.

It would be interesting to have an time dependent analysis on propeller thrust and torque when it is impinged by an vortex filament. Such an investigation could be done by applying RSB with high measurement frequency together with the synchronized PIV measurement. Further relationship between the vortex behavior and propeller

performance variation might be revealed by doing that research.

In the present project, since the PIV measurement planes cannot be placed infinitely close to the propeller disk, it is difficult to find out the development of the vortex filament in the field between these two planes. However, this is quite an essential issue for this problem. Considering this, a CFD study on the same research model might be able to provide answers for that.

Results and conclusions obtained from this project research could be applied to help understand the effect of the ground vortex problems, as stated in Chapter 1. Then, a more general situation, non-orthogonal vortex-propeller interaction, is worth for a further study. As a special situation, sometimes, vortices sucked from the position that is right down the propeller disk may impinge to the blade tip. Considering the existence of propeller tip vortices, it would be a more complicated problem. To study that, CFD might be an available tool, since experimental measurement would be very difficult to design and perform.

Reference

[1] Campell, James F., and Joseph R., Chambers. "Patterns in the sky: Natural visualization of aircraft flow fields." NASA SP-514, 1994.

[2] Schlinker, Robert H., and Roy K. Amiet. Rotor-vortex interaction noise. Vol. 3744. National Aeronautics and Space Administration, Scientific and Technical Information Branch, 1983.

[3] Nagahara, T., Sato, T. & Okamura, T. 2001 Effect of the submerged vortex cavitation occurred in pump suction intake on hydraulic forces of mixed flow pump impeller. *CAV 2001: 4th Intl Symp. on Cavitation, Pasadena, California.* (ed. C. Brennen, S. Ceccio & R. Arndt).

[4] Siervi, F. De, et al. "Mechanisms of inlet-vortex formation." *Journal of Fluid Mechanics* 124 (1982): 173-207.

[5] Ahmadi, All R. "An experimental investigation of blade-vortex interaction at normal incidence." *Journal of aircraft* 23.1 (1986): 47-55.

[6] Marshall, J. S. "Vortex cutting by a blade. I-General theory and a simple solution." *AIAA journal* 32.6 (1994): 1145-1150.

[7] Marshall, Jeffrey S. The Fluid Mechanics of Vortex Cutting By a Blade. Iowa State University, Iowa City, 1995.

[8] Liu, X., and J. S. Marshall. "Blade penetration into a vortex core with and without axial core flow." *Journal of Fluid Mechanics* 519 (2004): 81-103.

[9] Doolan, Cornelius J., Frank N. Coton, and Roderick A. McD Galbraith. "The effect of a preceding blade on the orthogonal vortex interaction." *Journal of the American Helicopter Society* 46.3 (2001): 221-227.

[10] Doolan, Cornelius Joseph, F. N. Coton, and R. A. M. Galbraith. "Surface pressure measurements of the orthogonal vortex interaction." *AIAA journal* 39.1 (2001): 88-95.

[11] Wang, Tongguang, et al. "Experimental study of the three dimensionality of orthogonal blade-vortex interaction." *AIAA journal* 40.10 (2002): 2037-2046.

[12] Kaynes, I.W., Preatoni, G., Visingardi, A., Tino, N., Arzoumanian, C., Kampa, K., Hermans, C., Renier, B. S. M., Tchen-Fo, F., and Bettschart, N., "HELIFLOW Pitch-Up and Quartering Flight Experiments," *Proceedings of the 26th European Rotorcraft Forum*, National Aerospace Lab. of the Netherlands, Amsterdam, 26–29 Sept. 2000, pp. 41.1–41.12.

[13] Wiesner, W., and Kohler, G., "Tail Rotor Performance in Presence of Main Rotor, Ground, and Winds," Journal of the American Helicopter Society, Vol. 19, No. 3, 1974, pp. 2–9.

[14] Fletcher, Timothy M., and Richard E. Brown. "Helicopter Tail Rotor Thrust and Main Rotor Wake Coupling in Crosswind Flight." *Journal of Aircraft* 47.6 (2010): 2136-2148.

[15] Houghton, Edward Lewis, and Peter William Carpenter. *Aerodynamics for engineering students*. Butterworth-Heinemann, 2003.

[16] Heene, Mario. "Aerodynamic Propeller Model for Load Analysis." Master of Science Thesis, Stockholm, Sweden, 2012.

[17] Ting, Lu, and Rupert Klein. "Viscous vortical flows." Springer-Verlag. ISBN 3-540- 53713-9. Vol. 374. 1991.

[18] Tung, C., et al. "The structure of trailing vortices generated by model rotor blades." (1981). NASA Technical Memorandum 81316.

[19] Takahashi, R. K., and Kenneth W. McAlister. "Preliminary study of a wing-tip vortex using laser velocimetry." (1987). NASA Technical Memorandum *88343*

[20] Bagai, Ashish, and J. Gordon Leishman. "Flow visualization of compressible vortex structures using density gradient techniques." *Experiments in Fluids* 15.6 (1993): 431-442.

[21] Squire, H. B. "The growth of a vortex in turbulent flow (vortex growth in turbulent incompressible flow)." *Aeronautical Quarterly* 16 (1965): 302-306.

[22] Bhagwat, Mahendra J., and J. Gordon Leishman. "Generalized viscous vortex model for application to free-vortex wake and aeroacoustic calculations."*Annual Forum Proceedings-American Helicopter Society*. Vol. 58. No. 2. American Helicopter Society, INC, 2002.

[23] Saffman, Philip G., J. Hinch, E *Vortex dynamics*. Cambridge university press, 1992. ISBN 0-521-47739-5. p. 253.

[24] H. Glauert. Airplane propellers. In W.F. Durand, editor, *Aerodynamic Theory*, volume IV. Julius Springer, 1935.

[25] Rwigema, M. K. "Propeller blade element momentum theory with vortex wake deflection." *Proceedings of the 27th Congress of the International Council of the Aeronautical Sciences, Nice, France, September*. 2010.

[26] Yannian Yang, Teng Zhou, Andrea Sciacchitano, Leo Veldhuis, and Georg Eitelberg, “Propeller and inflow vortex interaction: vortex response and impact on the propeller performance”, *5th CEAS Air & Space Conference, Delft, the Netherlands*, 2015

[27] Yang, Yannian, Andrea Sciacchitano, Leo Veldhuis, and Georg Eitelberg, "Experimental investigation of propeller induced ground vortex under headwind condition.", *32nd AIAA Applied Aerodynamics Conference, Atlanta, GA, 16-20 June 2014*.

[28] Lindeboom, R. C. J., J. J. H. M. Sterenborg, and C. J. Simao Ferreira. "Determination of unsteady loads on a DU96W180 airfoil with actuated flap using particle image velocimetry." *3rd EWEA Conference-Torque 2010: The Science of making Torque from Wind, Heraklion, Crete, Greece, 28-30 June 2010*. European Wind Energy Association, 2010.

[29] http://www.dept.aoe.vt.edu/~aborgolt/aoe3054/manual/expt7/DU96_Normalized_Profile.txt

[30] Daniel, Cuthbert. "One-at-a-time plans." *Journal of the American statistical association* 68.342 (1973): 353-360.

[31] Brix, S., G. Neuwerth, and D. Jacob. "The inlet-vortex system of jet engines operating near the ground." *AIAA paper* 3998 (2000): 2000.

[32] Reinaud, Jean N., and David G. Dritschel. "Destructive interactions between two counter-rotating quasi-geostrophic vortices." *Journal of Fluid Mechanics* 639 (2009): 195-211.

[33] Dritschel, David G. "A general theory for two-dimensional vortex interactions." *Journal of Fluid Mechanics* 293 (1995): 269-303.

[34] Roy, Clément, and Thomas Leweke. "Experiments on vortex meandering." *FAR-Wake Technical Report AST4-CT-2005-012238, CNRS-IRPHE, also presented in international workshop on fundamental issues related to aircraft trailing wakes*. 2008.

[35] Devenport, William J., et al. "The structure and development of a wing-tip vortex." *Journal of Fluid Mechanics* 312 (1996): 67-106

[36] Dritschel, D. G., and D. W. Waugh. "Quantification of the inelastic interaction of

unequal vortices in two - dimensional vortex dynamics." *Physics of Fluids A: Fluid Dynamics* (1989-1993) 4.8 (1992): 1737-1744.

[37] Trieling, R. R., OU Velasco Fuentes, and G. J. F. van Heijst. "Interaction of two unequal corotating vortices." *Physics of Fluids (1994-present)* 17.8 (2005): 087103.

[38] Meunier, Patrice, Stéphane Le Dizes, and Thomas Leweke. "Physics of vortex merging." *Comptes Rendus Physique* 6.4 (2005): 431-450.

[39] Bristol, R. L., et al. "On cooperative instabilities of parallel vortex pairs." *Journal of Fluid Mechanics* 517 (2004): 331-358.